

**DESIGN AND ANALYSIS OF A MECHANISM CREATING BIAXIAL WING
ROTATION FOR APPLICATIONS IN FLAPPING-WING
AIR VEHICLES**

by

Sean Harold McIntosh

A thesis submitted to the Faculty of the University of Delaware in
partial fulfillment of the requirements for the degree of Master of Science in
Mechanical Engineering

Fall 2005

Copyright 2005 Sean McIntosh
All Rights Reserved

UMI Number: 1430778

UMI[®]

UMI Microform 1430778

Copyright 2006 by ProQuest Information and Learning Company.
All rights reserved. This microform edition is protected against
unauthorized copying under Title 17, United States Code.

ProQuest Information and Learning Company
300 North Zeeb Road
P.O. Box 1346
Ann Arbor, MI 48106-1346

**DESIGN AND ANALYSIS OF A MECHANISM CREATING BIAxIAL WING
ROTATION FOR APPLICATIONS IN FLAPPING-WING
AIR VEHICLES**

by

Sean Harold McIntosh

Approved: _____
Dr. Sunil Kumar Agrawal, Ph.D., Mechanical Engineering
Professor in charge of thesis on behalf of the Advisory Committee

Approved: _____
Thomas S. Buchanan, Ph.D.
Chair of the Department of Mechanical Engineering

Approved: _____
Eric W. Kaler, Ph.D.
Dean of the College of Engineering

Approved: _____
Conrado M. Gempesaw II, Ph.D.
Vice Provost for Academic and International Programs

ACKNOWLEDGMENTS

I would like to thank my advisor, Dr. Sunil Agrawal, for the opportunity to work on such an interesting and rewarding topic. I would also like to thank Dr. Michael Keefe, and Dr. James Glancey for serving on my thesis committee. I would to thank the members of the “Bird Group,” Zaeem Khan and Matt McDonald, and also everyone in the Mechanical Systems Laboratory especially Andrew Schmalz and Jon Fader. I would also like to thank all my friends and family for their love and support.

TABLE OF CONTENTS

LIST OF FIGURES	vi
ABSTRACT	xiii
Chapter	
1 INTRODUCTION	1
1.1 Introduction	1
1.2 Micro Air Vehicles (MAVs)	2
1.2.1 Fixed Wing MAVs	3
1.2.2 Rotary Wing MAVs	5
1.2.3 Flapping Wing MAVs	6
1.3 Summary.....	9
2 AERODYNAMICS OF FLAPPING WING FLIGH	11
2.1 Introduction of Flapping Wing Aerodynamics.....	11
2.2 Geometric and Kinematic Parameters	11
2.3 Steady State Aerodynamics.....	14
2.4 Quasi-Steady State Aerodynamics	19
2.4 Quasi-unsteady State Aerodynamics.....	20
2.4.1 Leading Edge Vortex/ Delayed Stall.....	21
2.4.2 Rotational Force/Kramer Effect	22
2.4.3 Virtual Mass Effect/ Added Mass Effect	24
2.4.4 Wake Capture/Wing Wake Interaction	25
2.4.5 Clap and Fling Effect	27
2.4.6 Quasi-Unsteady model	28
2.5 Summary.....	30
3 MECHANICALHUMMINGBIRD PROJECT (MHP).....	31
3.1 Introduction to the Mechanical Hummingbird Project.....	31

3.2	Hummingbird Inspiration	31
3.3	Goals of the MHP	33
3.4	Mechanism Operation	36
3.5	Wing Kinematics	45
3.6	Specifications of MHP III	48
3.7	Summary.....	49
4	THEORETICAL ANALYSIS OF THE MHP	50
4.1	Introduction	50
4.2	Model Simplifications and Assumptions.....	50
4.3	Reference Frames	51
4.4	Forces and Moments acting on the Mechanism	53
4.5	Aerodynamics of the Flapping Wing	54
4.6	Solution Procedure	56
4.7	Model Results.....	60
4.8	Summary.....	64
5	EXPERIMENTAL ANALYSIS OF MHP	65
5.1	Introduction	65
5.2	Iterations of the MHP	65
5.3	Setup of the MHP II Experiments	68
5.4	Experimental Results of MHP II	71
5.5	Experimental Setup of MHP III	73
5.6	Experimental Results of MHP III.....	75
5.7	Conclusions	79
5.8	Summary.....	81
6	CONCLUSIONS AND FUTURE RECOMMENDATIONS	82
6.1	Conclusion.....	82
6.2	Future work	83
	APPENDIX A: EXPERIMENTAL RESULTS ON MHP II	85
	APPENDIX B: EXPERIMENTAL RESULTS OF MHP III.....	90
	APPENDIX C: FRABRICATION DETAIL OF MHP III.....	98
	REFERENCES.....	103

LIST OF FIGURES

Figure 1.1: Vortex generators on the Gloster Javelin, used to create turbulent air around the wings to delay flow separation and increase lift at high angles of attack. Fig. courtesy of http://www.aerospaceweb.org/question/aerodynamics/q0215.shtm	4
Figure 1.2: Fixed wing MAVs from left to right Trochoid developed by MLB, the Wasp developed at Aerovironment, and the flexible wing design developed at the University of Florida.	5
Figure 1.3: Examples of MAV helicopters; from left to right the meszipopter developed at Stanford, the pixelito, and the proxflyer.	6
Figure 1.4: A a replica model of a human powered ornithopter designed by Leonardo Da Vinci (circa 1490), B a more contemporary ornithopter modeled on the wing movement of a crow, developed by Edward Purkis Frost (circa 1904).	7
Figure 1.5: Examples of Ornithopters A <i>Slow Hawk II</i> manufactured by The Ornithopter Zone, B <i>Sparrow II</i> developed at the University of Delaware, C and <i>Microbat</i> developed at Caltech.	8
Figure 1.6: Examples of Ornithopters from right to left: The Mentor developed by SRI at the University of Toronto, the Elastodynamic Ornithoptic Robotic Insect developed at Vanderbilt University, and the Mechanical Flying Insect (MFI) developed at UC Berkeley	9
Figure 2.1: A shows a generic insect showing the geometric parameters relevant in flapping wing air vehicles. B shows the cross section of the wing and the geometric, α , and the effective angle of attack, α' , where U is the free stream velocity and $U'+U$ is the locally deflected stream [23].	12
Figure 2.2: There are two major wing motions shown in the Fig., a rotation about the flapping axis and a rotation about the feathering axis.	14
Figure 2.3: This is an illustration of the Kutta- Zhukhovsky condition. The actual flow field, C, is the sum of the invicid flow field, A, and a circulation field, B, whose magnitude just sufficient to move the rear stagnation point of A to the trailing edge [23].	16

Figure 2.4: This figure shows the starting vortex, Γ , developed by a wing starting from rest. An equal and opposite circulation develops around the wing such that the total circulation, in the region ABCD bounding both vortices, is zero [24]..... 17

Figure 2.5: A shows the motion of the leading edge vortices of a 2-d fixed wing. The vortex gains in strength until the air flowing over the wing can no longer reattach and the vortex separates. B shows the same LEV on a flapping wing. The spanwise flow stretches the LEV decreasing its inertia and increasing its angular velocity, thus the vortex remains stable and attached to the wing increasing its lift. This figure was modified from [2]. 22

Fig. 2.6: The figure shows how the rotation of the wing can develop lift. In (a) the wing is experiencing lift because of the Kutta condition, as the wing rotates the air on the top side of the wing is accelerated re-establishing the Kutta condition. It is important that the wing be rotating, because at the new steeper angle the flow would separate from the wing. 24

Fig. 2.7: This shows the virtual mass effect. A cylinder of air is assumed to be attached to the wing as seen in (a), (b), and (c). When the wing accelerates the mass of air resists the motion (a) but once the mass of air is moving at the same velocity as the wing there is no force (b). When the wing decelerates the mass of air acts as a force to keep the wing in motion (c)..... 25

Figure 2.3: In the wake capture mechanism LEV and TEV shed from the wing as seen in (a)-(c) interact with the wing as it reverses directions (d)-(e), this interaction can lead to an increase of lift, (Fig. borrowed from [2]). 26

Figure 6: This shows how the clap and fling mechanism might operate. At the end of the stroke the two wings collide canceling or partially canceling out TEV. TEVs delay the growth of LEVs at the beginning of the stroke, LEVs increase circulation over the wing increasing lift. Also as the two wings collide they produce a jet of air that helps increase lift. Fig. borrowed from [2] 28

Figure 3.1: An early prototype developed at the University of Delaware that creates a multi-oscillatory wing motion using a single motor. 34

Figure 3.2: Illustration of MHP III, featuring a novel mechanism to drive the flapping and feathering motion of the vehicle’s wings. The wings are driven by a single motor that operates two symmetric 4-bars which in turn operate two symmetric cam/follower mechanisms. 35

Figure 3.3: This shows some important features of the wing, namely the flapping and feathering axes. 36

Figure 3.3 A shows the feathering motion of MHP III—the wing moves from the supinated position (semi-transparent) to the pronated position. B shows the flapping motion of MHP III. The wing is in a fully pronated position as it moves through the downstroke. 37

Figure 3.4: A shows a schematic of the parts in the flapping mechanism of MHP III. B shows a closer look at some of the parts in the flapping mechanism. A detailed list of these parts and assembly procedures appear in Appendix B. 39

Figure 3.5: A shows the reciprocating motion created by the 4-bar mechanism, with the geometric link lengths shown in red. B shows the flapping motion of the wings generated by the 4-bar mechanism. 40

Figure 3.6: A shows the lobe end of the follower moving down the backside of the guide, putting the wing in a supinated position. Fig. B shows the non-lobed end of the follower moving up the front side of the guide, putting the wing in a pronated position. 41

Figure 3.7: This shows the motion of the follower along the guide. During the down stroke the follower moves up along the front of the guide. During the upstroke the follower moves down along the backside of the guide. Note that the motion of the follower is always opposite to the motion of the wing, as it moves down the wing moves up and vice versa. 43

Figure 3.8: This shows the matting externally and internally splined shafts that allow for different initial orientations of the wing with the follower. 44

Figure 3.9: This is the desired wing motion of MHP III. A positive lift force shown in blue is generated during the down stroke when the wing is pronated. During the upstroke the wing produces a smaller negative force while in a supinated position. Consequently there is a net positive lift force. 46

Figure 3.10: This shows the wing motion for different initial feather angles. A moves in an asymmetric motion and has an initial feather angle of 0 degrees and is the focus the experiments. B and C show initial feather angles of 30 and 80 degrees respectively. C is similar to the symmetric wing motion of flies..... 47

Figure 3.10: This shows the motion of a fly’s wing. The stroke plane is oriented horizontally and the net force of the wings in both the up and down stroke is vertical..... 48

Figure 3.5: Dimensioned illustration of MHP III. It weighs 50 grams and has a maximum flapping rate of 6 Hz. 49

Figure 4.1: A shows an illustration of the physical joint contrasted with B an illustration of the theoretical joint. 51

Figure 4.2: This shows the inertially fixed reference frame \mathcal{E} and the wing fixed reference frame \mathcal{F} . The flapping angle, ψ , the feathering angle, ϕ , and the out of plane angle, θ , are also shown..... 53

Figure 4.3: This is a free body diagram of the forces and moments that act on the flapping mechanism. 54

Figure 4.4: A differential aerodynamic force acting on a wing strip a distance r from the wing pivot. The differential force is created from the air velocity V contacting the wing at an angle α_l 56

Figure 4.7: The two graphs show the feathering and, flapping angle, and aerodynamic force in the Z direction vs. time. The force data is generated by the aerodynamic model presented. The magnitude of the lift generated in the down stroke is much greater then the magnitude of the negative lift generated in the upstroke. 62

Figure. 4.8: A shows the flapping, and feathering angle vs. time and B shows the aerodynamic force in the z direction vs. time. The wing is flapping at 5 Hz. 64

Figure 5.1: The photographs show the first iteration of the design, named MHP I. No quantitative experimentation was carried out on MHP I, but it did validate the basic premise of the mechanism..... 66

Figure 5.2: The photographs show the second iteration of the design, named MHP II. Initial lift experiments were performed on MHP II. 67

Figure 5.3: The photographs are of the most recent iteration of the design, named MHP III. Extensive measurements of lift production, wing position, and motor torques were performed on MHP III. 68

Figure 5.4: A schematic of the force torque sensor used in the experiments. The F_x and F_y axes are shown bisecting the circular cross-section of the sensor with the F_z axes directed out of the page. 69

Figure 5.5: The photograph shows the experimental setup used for MHP II. MHP II rests on top of a slender aluminum rod. Between MHP II and the rod is a small force/torque sensor. Also seen in the picture is the constant voltage power source used to power the MHP II's motor. 70

Figure 5.6: The graph shows the approximate power usage at various flap rates. Initially the power usage reduces as inertial forces overcome large frictional forces. The power usage then increases as inertial and aerodynamic forces increase. 72

Figure 5.7: Lift vs. time Graph of MHP II at a flapping rate of 1.9 Hz. For each stroke there are two distinct lift peaks that are surmised to correspond to translational forces and rotational forces. 73

Figure 5.8: The photographs show the experimental setup of MHP III. The grey cable, hanging off to the right is the encoder cable, and the black cable hanging off to the left is the force/torque cable. 75

Figure 5.9: The above graph is the typical set of data captured in the MHP III experiments. The first three graphs show the F_x , F_y , and F_z forces respectively. The fourth graph is the flapping angle position and the fifth graph is the motor power. 76

Figure 5.10: The graph shows where the motor power peaks occur relative to the flap angle. There is a large peak just after the wing begins its upstroke and a smaller peak just after the wing begins its down stroke. The large spikes are attributed to the inertial loads on the motor and the contact force of the follower with the guide. 77

Figure 5.11: The graph shows the F_z forces vs. time. The force values were much smaller than in the MHP II experiments but the average force in the down stroke was positive and the average force in the upstroke was negative consistent with predictions. 78

Figure 5.12: The graph shows the force data in the x direction and the flap angle vs. time. It shows two consistent spikes in lift during the translational motion of the wing.....	79
Figure 5.13: The observed motion of MHP III which differs from MHP II. At the top of the upstroke the wing over pronates reducing the effective wing surface area during the downstroke.....	80
Figure 5.14: This shows the force generation for the symmetric flapping observed by MHP III.....	81
Figure A.1: Aerodynamic forces in the x, y, and z directions with a motor current of 1.2 amps. The average force in the x and y is 0.01 N and -0.03 N respectively. The average force in the z direction is 0.32 N with a maximum force of 1.78 N.....	85
Figure A.2: Aerodynamic forces in the x, y, and z directions with a motor current of 1.5 amps. The average force in the x and y is 0.00 N and -0.03 N respectively. The average force in the z direction is 0.33 N with a maximum force of 2.12 N.....	86
Figure A.3: Aerodynamic forces in the x, y, and z directions with a motor current of 1.7 amps. The average force in the x and y is -0.02 N and -0.02 N respectively. The average force in the z direction is 0.46 N with a maximum force of 1.67 N.....	87
Figure A.4: Aerodynamic forces in the x, y, and z directions with a motor current of 2.0 amps. The average force in the x and y is 0.01 N and -0.04 N respectively. The average force in the z direction is 0.48 N with a maximum force of 2.61 N.....	88
Figure A.5: Aerodynamic forces in the x, y, and z directions with a motor current of 2.1 amps. The average force in the x and y is 0.01 N and -0.05 N respectively. The average force in the z direction is 0.54 N with a maximum force of 3.47 N.....	89
Figure B.1: 3v Trial 1—Flap Rate = 2.9 Hz, $F_{x\text{mean}} = 0.0607$ $F_{y\text{mean}} = -0.0046$, $F_{z\text{mean}} = -0.0642$, $\text{Power}_{\text{mean}} = 0.5399$ W	90
Figure B.2: Trial 1—Flap Rate = 4.0 Hz, $F_{x\text{mean}} = 0.0140$ N, $F_{y\text{mean}} = 0.0474$ N, $F_{z\text{mean}} = 0.1290$ N, $\text{Power}_{\text{mean}} = 0.8143$ W	91
Figure B.3: Trial 1—Flap Rate = 5.5 Hz, $F_{x\text{mean}} = 0.2412$ N, $F_{y\text{mean}} = 0.0138$ N, $F_{z\text{mean}} = -0.0290$ N, $\text{Power}_{\text{mean}} = 1.2219$ W	92

Figure B.4: Trial 1—Flap Rate = 6.7 Hz, $F_{x\text{mean}} = -0.0017$ N, $F_{y\text{mean}} = -0.0040$ N, $F_{z\text{mean}} = 0.0110$ N, $\text{Power}_{\text{mean}} = -4.3910$ W	93
Figure B.5: Trial 2—Flap Rate = 3.2 Hz, $F_{x\text{mean}} = 0.2121$ N, $F_{y\text{mean}} = 0.1033$ N, $F_{z\text{mean}} = 0.0209$ N, $\text{Power}_{\text{mean}} = 0.9098$ W	94
Figure B.6: Trial 2—Flap Rate = 5.2 Hz, $F_{x\text{mean}} = 0.2014$ N, $F_{y\text{mean}} = 0.1116$ N, $F_{z\text{mean}} = -0.0244$ N, $\text{Power}_{\text{mean}} = 1.1530$	95
Figure B.7: Trial 3 Flap Rate = 3 Hz, $f_{x\text{mean}} = -0.4089$ N $f_{y\text{mean}} = -0.3176$ N $f_{z\text{mean}} = 0.1628$, $\text{Power}_{\text{mean}} = 0.7210$ W	96
Figure B.8: Trial 3—Flap Rate = 3.3 Hz, $F_{x\text{mean}} = 0.0637$ N, $F_{y\text{mean}} = 0.0451$ N, $F_{z\text{mean}} = 0.0659$ N, $\text{Power}_{\text{mean}} = 0.8653$ W	97
Figure C.1: labeled wing	99
Figure C.2: Body Assembly	101
Figure C.3: Wing Carriage Assembly	102

ABSTRACT

Flapping wing air vehicles, also known as ornithopters, are a promising new technology, especially for the new class of aircraft known as micro air vehicles (MAV). These vehicles are classified by the defense army research project agency (DARPA) to have overall dimensions less than 15 cm. With their small size, MAVs can operate in locations inaccessible to other larger vehicles. Possible applications of MAVs are numerous for both military and civilian purposes. The majority of MAVs in existence have either fixed or rotary wings. Unfortunately, the aerodynamic performance of these vehicles deteriorates as their size decreases. Insects and hummingbirds, however, are much smaller than present MAVs and operate magnificently. These biological designs inspire the creation of flapping wing MAVs, especially for slow-flight and hover-flight MAVs.

Research studies have discovered a variety of aerodynamic mechanisms created by the flapping wing flight of insects. Complex wing rotations about multiple axes have been identified to provide the flight behavior characterized by these newly discovered aerodynamic mechanisms. A major issue in the development of MAVs, is the design of mechanisms that can generate the complex wing motion necessary for the vehicle to fly and hover. This thesis briefly outlines the current theory of flapping wing aerodynamics and applies it in the design of a flapping wing mechanism that can potentially hover. A detailed description of the mechanism is given along with a mathematical model that integrates empirically observed aerodynamic theory along

with classical rigid body dynamics of the mechanism. The model helps predict the lift forces and the power requirements of the mechanism. Furthermore, experimental measurements from the prototype help in validation of the theoretical predictions.

Chapter 1

INTRODUCTION

1.1 Introduction

The purpose of this thesis and the research is to use the basic understanding of flapping wing vehicles to design working prototypes of flapping wing micro air vehicles (MAVs). Flapping wing vehicles, also known as ornithopters, have been in existence for years, but only recently has the potential of small unmanned aircrafts become apparent. Inspired by the remarkable ability of insects and birds, it is believed by scientists and engineers that these vehicles will surpass the ability of fixed and rotary wing MAVs, especially during slow and hover-flight. The aerodynamics of hover-flight and the design of a flapping wing mechanism for hover flight is the focus of this thesis. Hover flight is an important topic to study for a number of reasons: (i) the vehicle can be tethered to a fixed position preventing costly crashes involved in forward flight testing, (ii) expensive wind tunnels are not necessary, (iii) lift forces can be calculated simply by measuring the change in weight. Furthermore, hover-flight is perhaps the most challenging mode of flight, and vehicles capable of hovering can also fly forward [1]. The contribution of this thesis is three fold, first and foremost it presents an original design for a flapping wing vehicle, very few researches have created designs attempting, secondly it applies classical dynamics and a newly developed analytic aerodynamic model to predict the vehicles

performance, and thirdly it presents an experimental method to validate the predictions of the theoretical model.

1.2 Micro Air Vehicles (MAVs)

The Defense Advanced Research Projects Agency (DARPA) characterizes Micro Air Vehicles (MAVs) as aircrafts with a maximum dimension of 15 cm, along any direction, and capable of flight speeds of 25 mph or less, with a flight duration of 20 to 30 minutes [2]. MAVs enjoy many advantages over larger flying vehicles—they can safely fly low to the ground and in restrictive environments including dense forests, battlefields, and office buildings. MAVs offer a number of reconnaissance opportunities, including photographing targets and areas of interest obstructed to higher-flying vehicles and satellites. MAVs can be much harder to detect and combat compared to larger aircraft. If destroyed, MAVs may be substantially less expensive to replace. Beyond their military function, MAVs can also be useful in civilian applications providing visual access for search and rescue operations, exploratory missions, and cinematography. For example, MAVs fitted with infrared cameras could detect people trapped in collapsed buildings while minimizing risk to rescuers. Similarly, a video crew at a sporting event or a movie set could capture spectacular, never before seen angles using MAVs. Perhaps, someday, the toys that hobbyists once used to enjoy a day at the park may become crucial in exploring distant planets.

In the past, a number of factors have limited the development and successful implementation of MAVs for military and civilian use. These factors include the weight and power of essential components. Batteries and motors have made enormous improvements in the past few years, with a significant reduction in size and

weight with an increase in power. Also, structural components, such as high-strength plastics, e.g. delrin, and composites, e.g. carbon fiber, allow for lighter and more resilient vehicle bodies. Furthermore, on-board electronics such as transmitters, cameras, and on-board computers, have shrunk to mere grams. Most importantly, scientists are finally beginning to understand the aerodynamics of small-scale flight, unlocking the mysteries of how insects defy previously conceived notions of flight. Science and technology have reached a point where the dreams of creating MAVs are now possible.

1.2.1 Fixed Wing MAVs

The majority of MAVs in use today are scaled down versions of the more traditional manned aircraft. These MAVs, like their larger counter parts, use either fixed wings or rotary wings to fly. There has been a great deal of research and development into these vehicles. Some of these designs already meet DARPA's requirements for MAVs and there is no doubt they will continue to improve and become more apt to meet their design needs. However, many of these vehicles are beginning to show their limitation as their size decreases. The reason for this is because the dimensionless parameter, Reynolds number, decreases as an aircrafts flight speeds and wing span decreases. The nature of air flow is dependent on the Reynolds number, at high Reynolds the flow around a fixed wing is turbulent, at low Reynolds numbers the flow is laminar. In the laminar flow there is less kinetic energy and the flow will separate from the wing at a lower angle of attack than in turbulent flow. Therefore a wing moving in turbulent air can generate more lift than the same wing in laminar air. Even large airplanes have the problem of low lift due to laminar flow when flying low speeds, some airplanes have small devices called vortex

generators as seen in Fig. 1.1. These devices help break up the flow to create turbulence. In the much lower Reynolds number régimes of MAVs such devices are less effective [24].



Figure 1.1: Vortex generators on the Gloster Javelin, used to create turbulent air around the wings to delay flow separation and increase lift at high angles of attack. Fig. courtesy of <http://www.aerospaceweb.org/question/aerodynamics/q0215.shtml>

Fig. 1.2 shows three examples of fixed wing MAVs, the Trochoid, the Wasp and a flexible wing design. The *Wasp*, developed by Aerovironment, has a wing span 33 cm [4]. The *Trochoid*, developed by the MLB company, has a wingspan of 20 cm [5]. The flexible-wing design, developed by the University of Florida, has a wing span of 15 cm [6]. Lightweight Li-polymer batteries power the Trochoid and the flexible wing design, and the Wasp is powered by a hydrogen fuel cell allowing for mission durations as long as 1 hour 45 minutes.



Figure 1.2: Fixed wing MAVs from left to right Trochoid developed by MLB, the Wasp developed at Aerovironment, and the flexible wing design developed at the University of Florida.

1.2.2 Rotary Wing MAVs

One of the most obvious drawbacks of fixed wing vehicles is their inability to hover. Rotary wing vehicles, though, are designed specifically for this purpose. These vehicles can also fly forward but expend much more energy than fixed wing vehicles [7]. Furthermore, at low Reynolds number, the efficiency of helicopters decreases for much the same reason that fixed wing planes decrease in efficiency. Despite these problems, there are still a number of successful rotary wing MAVs as shown in Fig. 1.3. Examples include the proxflyer which has a rotor length of 35cm [8], the pixelito [9], and the mesicopter, developed at Stanford University, which has four rotors each having a length of 3 cm [10].

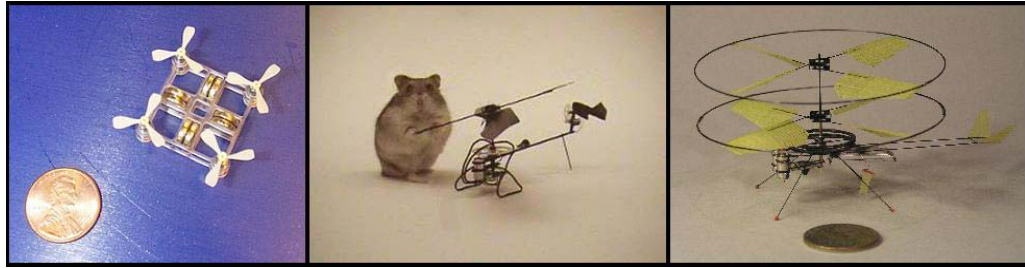


Figure 1.3: Examples of MAV helicopters; from left to right the mescipopter developed at Stanford, the pixelito, and the proxflyer.

1.2.3 Flapping Wing MAVs

Flapping wing vehicles attempt to solve the problem of poor aerodynamic efficiency of MAVs. Far from being a new idea, many of the first attempts at human flight used flapping wings. Leonardo De Vinci drew detailed sketches of human-powered ornithopters as early as 1490 AD [11]. In more recent history, the inventor Edward Purkis Frost designed and built a manned ornithopter powered by an internal combustion engine (circa 1904) [12]. There have been many attempts to create manned flapping wing aircraft. Unfortunately, except for a few rare examples, these attempts have all failed. Some of the more promising attempts were the human-powered ornithopter by Alexander Lippisch that could perform power glides [13], and the Project Ornithopter of the University of Toronto that self accelerated to lift off speeds on level pavement [14]. Wings large enough to lift a human have proportionally larger inertias than even the largest avian inspirations. Early designs of mechanisms powerful enough to flap large wings were far too heavy for flight and in many cases would shake the aircraft apart. Pioneers of the first successful manned aircraft soon abandoned designs of ornithopters and created fixed and rotary wing

vehicles. Fig. 1.4 shows a replica model of Da Vinci's ornithopter and a photograph of Frost's ornithopter.

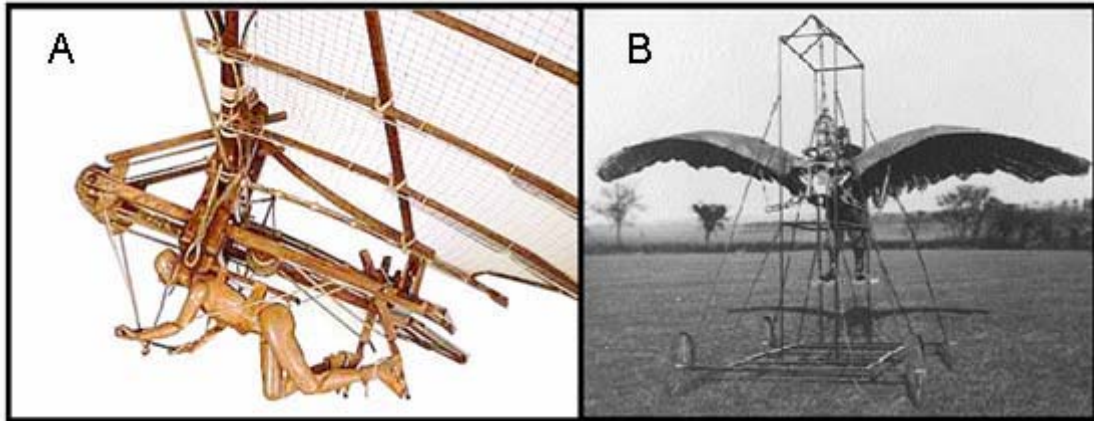


Figure 1.4: A a replica model of a human powered ornithopter designed by Leonardo Da Vinci (circa 1490), B a more contemporary ornithopter modeled on the wing movement of a Midnight Turkey, developed by Edward Purkis Frost (circa 1904)

Even though flapping wings may not be ideal for human-scale flight, they show a great deal of promise for MAVs. Lift is proportional to wing surface area, while wing inertia is proportional to the wing mass. The wing surface area, consequently the lift, is proportional to the square of the wing length, $F_{lift} \propto L_{wing}^2$. The wing mass, and consequently wing inertia, is proportional to the cube of the wing length, $I_{wing} \propto L_{wing}^3$. Thus, the wing inertia becomes proportionally smaller than the lift generation as the wing length decreases [15]. Thus, smaller vehicles can flap their wings proportionally faster generating more lift. Furthermore, with this ability of small ornithopters to flap their wings at higher rates comes the ability to move the

wings through complex motions, taking advantage of numerous aerodynamic mechanisms discussed further in Chapter 2.

Though large manned ornithopters are exceedingly rare, there are numerous examples of ornithopters at smaller scales. An example of a commercially available ornithopter, is *Slow Hawk*, manufactured by the Ornithopter Zone. *Slow Hawk* is a remote control operated ornithopter and has a wingspan of 47 inches [16]. A smaller design, built at the University of Delaware, is *Sparrow II* [17]. *Sparrow II* is powered by a Lithium polymer battery and has a wingspan of 36 cm. Even smaller is the radio controlled ornithopter, developed at Caltech, named the *microbat*. *Microbat* has a wingspan of 20 cm [18]. Figure 1.5 shows photographs of these three ornithopters.

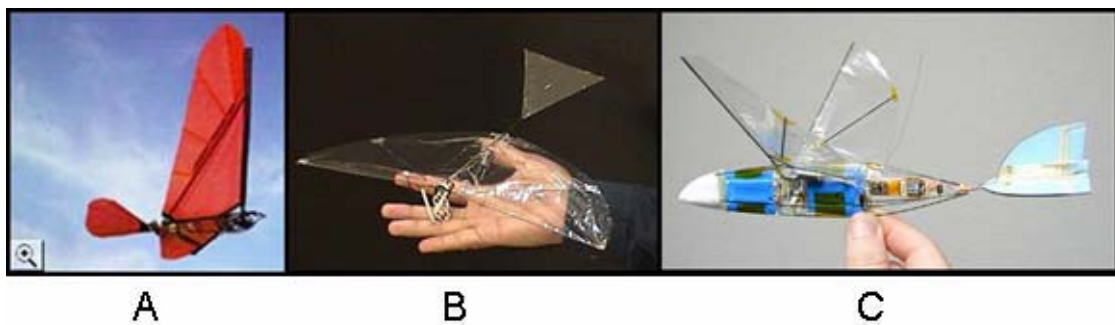


Figure 1.5: Examples of Ornithopters A *Slow Hawk II* manufactured by The Ornithopter Zone, B *Sparrow II* developed at the University of Delaware, C and *Microbat* developed at Caltech.

New designs of ornithopters, and the particular design which is the focus of this thesis, rely on more complex wing motions to generate lift. For example, the Mentor [19], developed by SRI and the University of Toronto uses four opposable

wings that actually contact each other while flapping, to produce a recently discovered aerodynamic mechanism known as clap-fling (see in Sec. 2.4.5). The Micromechanical Flying Insect (MFI) of Berkley uses peizo-electric actuators to create wing flapping and twisting [20]. Another example is Vanderbilt's Elastodynamic Ornithoptic Robotic Insect which involved the mechanical amplification of small piezoceramic wafer actuators exciting natural frequencies in the wing [21] *This needs to be finished*. Fig. 1.6 shows photographs of these three ornithopters.

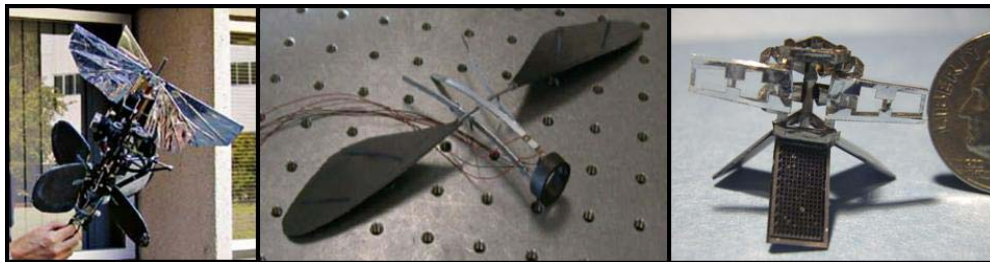


Figure 1.6: Examples of Ornithopters from right to left: The Mentor developed by SRI at the University of Toronto, the Elastodynamic Ornithoptic Robotic Insect developed at Vanderbilt University, and the Mechanical Flying Insect (MFI) developed at UC Berkeley

1.3 Summary

This chapter has presented the state-of-the-art in MAV design for fixed, rotary, and flapping wing vehicles, and offered a number of potential applications. As discussed briefly, there are aerodynamic limitations to fixed and rotary wing MAVs. Because of these limitations, there needs to be new innovative designs for MAVs.

Flapping wing air vehicles offer numerous aerodynamic advantages and will perhaps be the dominant vehicle for MAV use.

The remainder of this thesis is laid out as follows. Chapter 2 discusses the aerodynamics of flapping flight. It outlines currently believed theories of flapping wing flight and the aerodynamic mechanisms applied to our current design. Chapter 3 details the development and operation of the prototype mechanism. Chapter 4 develops a simulation model to predict dynamics of the prototype mechanism. Chapter 5 validates the theoretical model with experiments from the prototype designs. Finally, Chapter 6 provides conclusions and recommendations for future work.

Chapter 2

AERODYNAMICS OF FLAPPING WING FLIGHT

2.1 Introduction of Flapping Wing Aerodynamics

Traditionally, the majority of aerodynamics theory has focused on fixed and rotary wing vehicles. Serious investigation of flapping wing aerodynamics has only begun in the past decades. The earliest flapping wing studies used quasi steady-state models, ignoring time variant properties, to predict wing lift [22]. Not surprisingly, these early models greatly underestimated the lift generation in flapping wings. Recent experiments using particle image velocometry (PIV) and two-dimensional computer analysis of vorticity generation [23] has greatly enhanced the understanding of flapping wing flight. These studies have led to the discovery of a number of unsteady aerodynamic mechanisms involved in flapping wing flight. From the understanding of steady and unsteady effects, some researchers have developed *quasi unsteady* models that do a much better job in predicting lift than previous *quasi steady* models. This chapter focuses on one particular *quasi steady* model, developed at the University of Delaware [41]. This model is later incorporated into a dynamic model of a flapping wing prototype introduced in Chapter 3.

2.2 Geometric and Kinematic Parameters

Before presenting a detailed discussion of flapping wing aerodynamics, it is important to understand the nomenclature characterizing the geometric and

kinematic parameters specific to flapping wing vehicles (much of this terminology is borrowed from the nomenclature of insect biology). The geometric terminologies are as follows: *Leading Edge*—the edge of the wing that meets the airflow first. *Trailing Edge*—the edge opposite to the leading edge. *Wing span*—the length between the tips of the wings when they are out stretched laterally. *Wing length*—the base-to-tip length of one wing. *Wing chord*—the section between the leading and trailing edge of the wing at any position along the span. *Geometric Angle of Attack*— α , the angle the wing chord makes with the free stream velocity vector. *Effective Angle of Attack*— α' , the angle the wing chord makes with the locally deflected free stream velocity vector [23]. All the parameters are shown in Fig. 1.

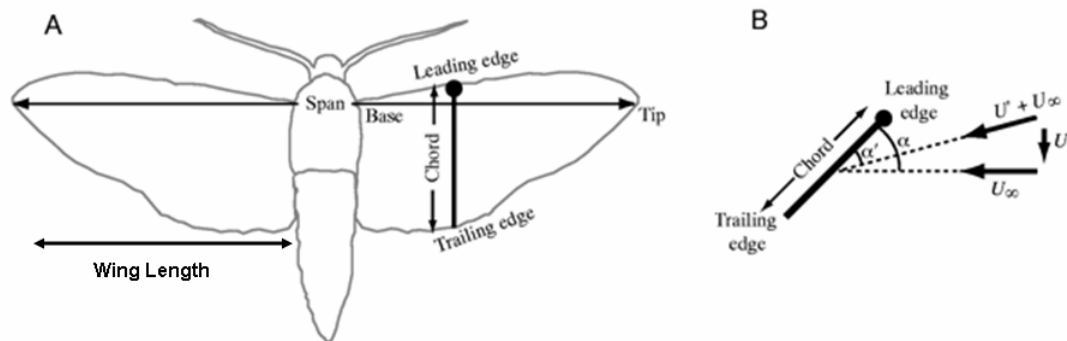


Figure 2.1: A shows a generic insect showing the geometric parameters relevant in flapping wing air vehicles. B shows the cross section of the wing and the geometric, α , and the effective angle of attack, α' , where U is the free stream velocity and $U'+U$ is the locally deflected stream [23].

The kinematic parameters are as follows: *Feathering*—also referred to as *rotational* motion, is the rotation of the wing about a spanwise axis, often

corresponding to the leading edge, this axis is the *feathering axis*. *Flapping*—also referred to as *translational* motion, is the rotation of the wing about an axis perpendicular to the feathering axis that passes through the wing base, this axis of rotation is the *flapping axis*. The flapping motion defines the *stroke plane*, the plane perpendicular to the flapping axis. In general the insect's leading edge stays in the stroke plane. This stroke plane may be roughly horizontal for some hovering species whereas others have a more inclined stroke plane (Ellington, 1984c; Dudley, 2000.). In both circumstances, it is conventional to use the terms *upstroke* and *down stroke* to describe the ventral-to-dorsal and dorsal-to-ventral rotations of the wings (dorsal refers to the backside of the insect and ventral the front side of the insect) [23]. The directions of the feathering rotation also have specific terms. The feathering motion, during which the ventral wing surface (the bottom surface) is rotated upwards, is termed *supination*, and occurs just prior to the beginning of the upstroke. The feathering motion, during which the dorsal surface (the top surface) is rotated upwards is termed *pronation*, this usually occurs just prior to the beginning of the downstroke. Supination is similar to turning one's palms up and pronation is similar to turning one's palms downwards. These parameters are shown in Fig. 2.2.

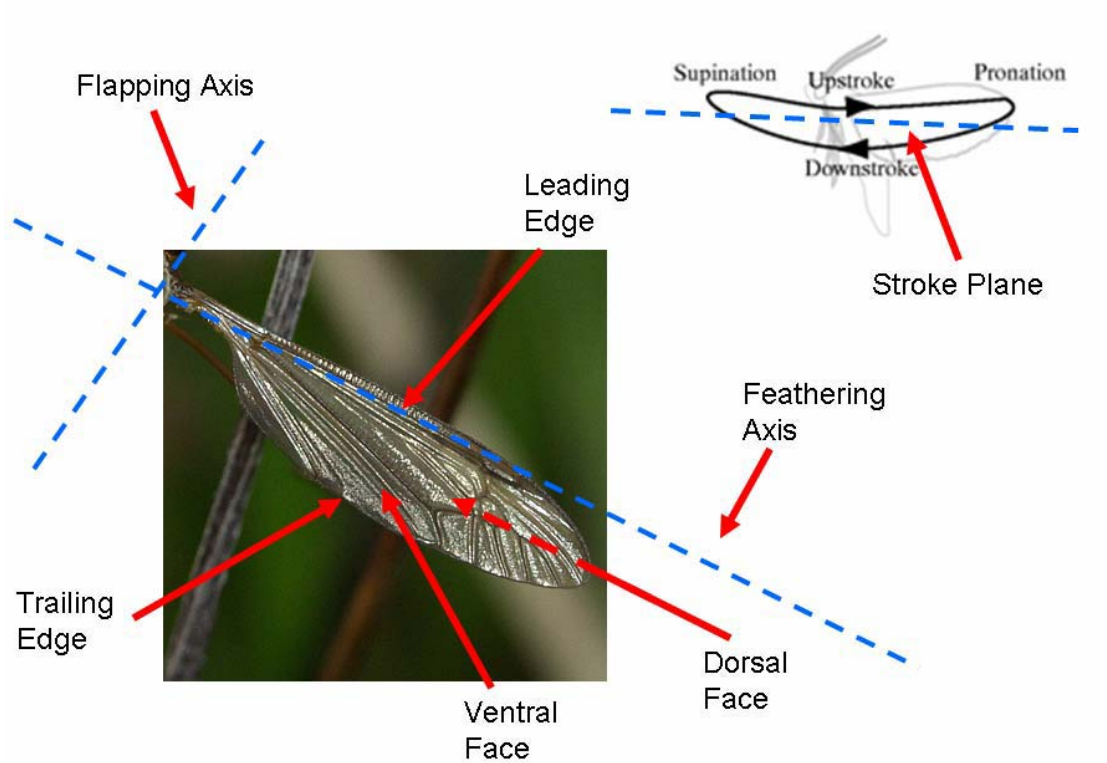


Figure 2.2: There are two major wing motions shown in the Fig., a rotation about the flapping axis and a rotation about the feathering axis.

2.3 Steady State Aerodynamics

Although steady state aerodynamics does not describe the air flow around flapping wings, it does serve as the basis for developing much of the aerodynamics of flapping wings. Steady state flow defines a condition where the fluid properties (e.g. pressure, temperature and velocity) at any point in the flow do not change over time. For steady state flow over an airfoil, the velocity at a particular point on the airfoil does not change with time; however, it can be different at different spatial positions. For steady state flow, as well as the unsteady flow of flapping wings, a vehicle's

wings must accelerate the fluid volume surrounding the wing in a downward direction [24].

Two important concepts in understanding how an aircraft's wings direct the surrounding fluid in a downward direction are vorticity and circulation. Both quantities describe rotational motion in fluids. Vorticity is the rotation of a fluid element at a point, where circulation is the total amount of vorticity passing through any plane region within a flow field (Von Mises 1959). Without local changes in fluid velocity, a translating wing would not produce vorticity. Consequently, there would be no circulation and no lift production. This is because circulation depends on flow velocity; larger circulation coincides with smaller pressure forces above the wing pulling the wing in an upward direction. The relationship between upward lift per unit wingspan and circulation in a potential flow is given by the Kutta-Zhukhovsky theorem

$$L = \rho u \Gamma, \quad (2.1)$$

where ρ is the fluid density and u is the airfoil speed and Γ is the circulation [22] [23] [24].

Because of the very low viscosity of air, it is often assumed to be a non-viscous ideal fluid. If there is no circulation in a non-viscous fluid moving around an airfoil, the initial streamlines must coincide with the exiting streamlines. In order for this to occur a stagnation point must develop on the ventral wing surface just behind the leading edge and on the dorsal surface just before the trailing edge, also there must be a sharp kink in the flow field just behind the trailing edge, as shown in Fig. 2.3 A [24]. Because there is no net change in the fluid momentum before and after it passes over the airfoil there is no lift generation. Fig. 2.2 C, however, is the experimentally

observed flow field, that does create lift. The Kutta condition accounts for this discrepancy by adding an arbitrary value of circulation to the flow field. The Kutta condition states that in flow over a two-dimensional body with a sharp trailing edge, there develops a circulation of magnitude just sufficient to move the rear stagnation point to the trailing edge [22] [23] [24].

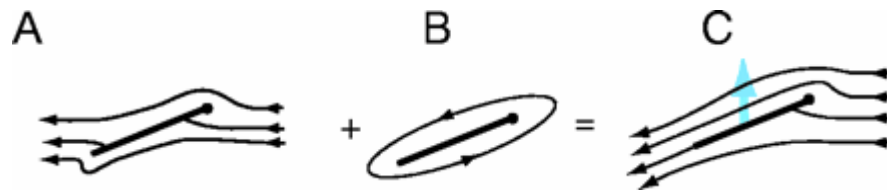


Figure 2.3: This is an illustration of the Kutta- Zhukhovsky condition. The actual flow field, C, is the sum of the inviscid flow field, A, and a circulation field, B, whose magnitude just sufficient to move the rear stagnation point of A to the trailing edge [23].

The reason that this circulation develops is due to the invalid assumption that air is completely inviscid. Inviscid flow is a valid assumption for the majority of the flow field except in the small region around the wing known as the boundary layer. The boundary layer is the thin layer of fluid attached to the wing's surface serving as the interface between the solid body and the fluid surroundings. In this transition region, fluid velocities increase from zero near the wing surface (no slip condition) to the free stream velocity, further away from the wing [22] [23] [24].

To understand how the boundary layer viscosity generates circulation consider an airfoil starting from rest. The initial flow is irrotational everywhere, because vorticity adjacent to the surface has not yet diffused outward. The velocity has a near discontinuity adjacent to the wing surface, and the flow resembles Fig. 2.3

A. The fluid must move at a very high velocity around the flow singularity, at this very high velocity there is a severe pressure differential in adjacent fluid flows, making even small values viscosity dominant forces. At this point, boundary layers develop around the airfoil, slowing the fluid velocity. Kinetic energy is dissipated by the viscosity in the boundary layer, preventing the flow from moving around the steep pressure rise near the trailing edge of the airfoil. This generates a back-flow and causes the boundary layer to separate at the trailing edge. This separation creates a starting vortex, which moves downstream in the flow and is left at the location where the airfoil started its motion [24]. Fig. 2.4 shows the formation of the starting vortex.

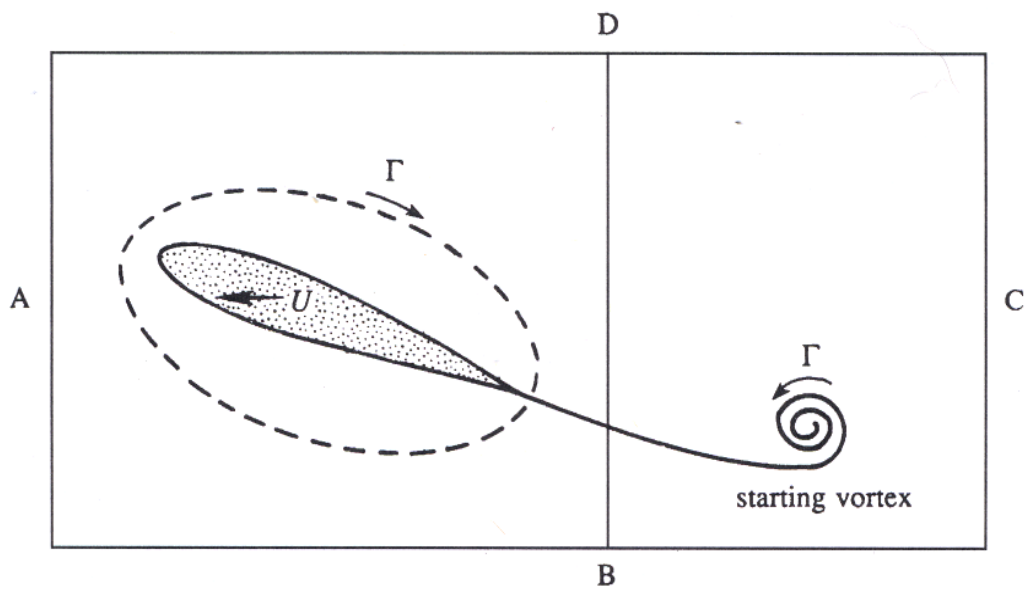


Figure 2.4: This figure shows the starting vortex, Γ , developed by a wing starting from rest. An equal and opposite circulation develops around the wing such that the total circulation, in the region ABCD bounding both vortices, is zero [24].

According to the Kelvin circulation theorem, the circulation around any material circuit remains constant, if the circuit remains in a region of inviscid flow—although viscous processes may go on inside the region enclosed by the circuit. Therefore, if the starting vortex rotates counter clockwise, the airfoil must generate a clockwise circulation to balance out the effects of the starting vortex. Only a circulation that moves the rear stagnation point exactly to the trailing edge will satisfy this theorem. With every change in speed the airflow or angle of attack, a new starting vortex is cast off and left behind [24].

Theoretical computation of circulation can be a difficult proposition. Consequently, the simple empirical formula, Eq. (2.2), was developed to calculate the lift of a differential thick airfoil strip.

$$dF = \frac{1}{2} \rho C_L \alpha U^2 c dr, \quad (2.2)$$

where dF is the aerodynamic force perpendicular to the wing chord for the wing strip, ρ is the fluid density, U is the free stream velocity, c is the chord length, dr is the thickness of a differential wing strip, and C_L is an experimentally determined lift coefficient based on the shape of the airfoil. Using an approach called *blade element method* (BEM) the lift of an entire wing can be determined from Eq. (2.2). BEM involves dividing a wing into n strips. The force acting on each strip is calculated then the strips are summed to give the total airfoil lift. BEM is an important concept that will be expanded for use in quasi-steady and quasi-unsteady state analysis of airfoils [22].

2.4 Quasi-Steady State Aerodynamics

A flapping winged vehicle, even when its body is moving at a constant air speed, is not in a steady state flow. The wings rotate about both the feathering and flapping axes, resulting in unsteady airflow over the wings. The first attempts in calculating flapping wing aerodynamics used *quasi-steady* state models [23]. The assumption for quasi steady-state model is that the instantaneous aerodynamic force on a flapping wing is equal to the force during steady motion at an identical instantaneous velocity condition and angle of attack [25]. The actual fluid motion over the flapping wing is approximated by the fluid motion of a series of static wing positions coinciding with the actual wing motion. In order to solve for the aerodynamic lift BEM is again used similar to Sec. 2.3. The differential lift of each wing strip is found using the same steady state Eq. (2.2), except now the wing strips may have different airspeeds and angles of attack due to the flapping and feathering motions. The process is then repeated an instant later with the wing in a new position with a newly calculated flow field. The lift generated at each instant can be integrated throughout one entire wing stroke giving the total lift.

This approach ignores three-dimensional forces such as span wise flow and wing-tip vorticity. Discrepancies between calculated and measured flight forces arise due to assumptions of steady-flow. Ellington (1994a) argued that if the predicted lift from the quasi-steady model was less than the mean lift required to hover, then the model is insufficient. Theoretical lift coefficients from quasi-steady state conditions for insect wings are measured to be around 1.0, as shown in numerous studies (Newman et al. 1977; Okamoto et al. 1996; Wakeling and Ellington 1997b; Nachtigall 1977; Vogel 1967; Zanker and Gotz 1990; Dudley and Ellington 1990b). However, experimental lift coefficients of these same insects showed lift coefficients ranging

from 1.2 to 4 (Ellington 1975, 1984e; Lehmann and Dickinson 1998; Norberg 1975a; Weis-Fogh 1972,1973). Such findings, Ellington argues, show that quasi-steady state theory falls short of accurately predicting lift values [23] [26].

In order to more accurately predict flapping wing aerodynamics, it is therefore necessary to have a better approach. There has been considerable effort in the past few years to create computational solutions for flapping wing flight, Liu and coworkers built a full Navier-Stoke's simulation using a *finite volume method* for the hawkmoth (*Manduca sexta*) [27]. Another prominent researcher, Dickinson used computational approaches to model the airflow over a fruit fly (*Drosophila*) wing. Computational methods provide useful information about the flow field, but require enormous computational resources. Instead, the research of this thesis relies on approximate analytical models described as quasi-unsteady aerodynamics [28].

2.4 Quasi-unsteady State Aerodynamics

Quasi-unsteady aerodynamic models rely heavily on experimental evidence of certain *aerodynamic mechanisms*. Aerodynamic mechanisms are identifiable flow formations that cause predictable aerodynamic forces. These mechanisms have been observed and measured experimentally in fluid flows. There have been some computational studies to verify the existence of some aerodynamic mechanisms [27]. The following sections discuss the prominent aerodynamic mechanism identified thus far by researchers. These mechanisms include *leading edge vortex, rotational force, virtual mass, wake capture, clap and fling*.

2.4.1 Leading Edge Vortex/ Delayed Stall

A leading edge vortex is, as the name implies, is a vortex attached to the leading edge of a wing. As detailed earlier, circulation influences flow velocities, greater flow velocities on the dorsal wing surface reduce pressure forces above the wing creating lift. A LEV on the dorsal wing surface will increase the flow velocity over the top of the wing thus increasing the lift. Airplane pilots can dramatically experience this phenomenon while flying at high angles of attack. When an airplane's angle of attack exceeds a critical value of approximately 12-15 degrees [29] the flow on the top surface begins to detach and a LEV begins to form. As the vortex builds in strength, the airplane experiences a burst of lift, the vortex is unstable though and after the plane has moved 1-2 chord lengths, the vortex detaches and there is a dramatic loss in lift known as a stall—thus the term *delayed stall*.

Certain airplanes, such as the Concorde, use swept back wings to create a spanwise flow across the wing. A span-wise flow stretches the LEV outwards to the wing tip, the LEV then merges with the tip vortex, thus forming an L shaped vortex as shown in Fig. 2.5. Stretching the vortex decreases its moment of inertia and increases its angular velocity thus preventing dissipation [22] [23] [30]. Insects generate a spanwise flow through the flapping motion of the wings. This spanwise flow allows for even greater angles of attack than swept wing airplanes, while still maintaining stable LEVs. Experiments of hovering hawkmoths suggest that nearly two thirds of the overall lift of flapping wings is due to LEVs [31].

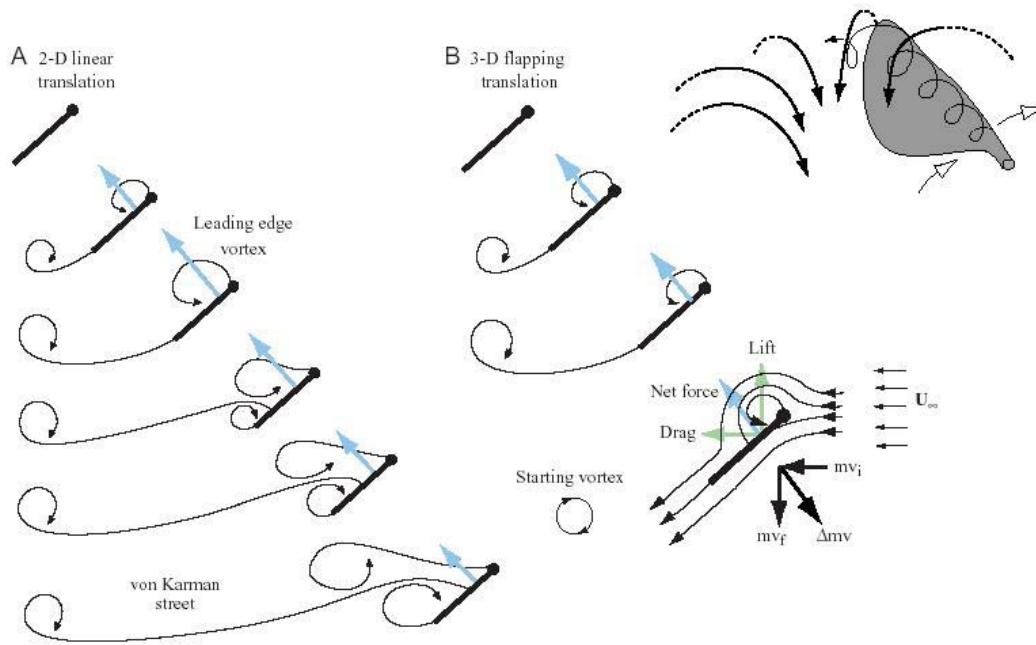


Figure 2.5: A shows the motion of the leading edge vortices of a 2-d fixed wing. The vortex gains in strength until the air flowing over the wing can no longer reattach and the vortex separates. B shows the same LEV on a flapping wing. The spanwise flow stretches the LEV decreasing its inertia and increasing its angular velocity, thus the vortex remains stable and attached to the wing increasing its lift. This figure was modified from [2].

2.4.2 Rotational Force/Kramer Effect

LEV effect occurs during the flapping or translational motion of the wings, but another important effect occurs during feathering, i.e. the rotational motion of the wings during the transitions between up and down strokes. One such mechanism is the *rotational force* or the *Kramer effect*. This phenomenon is similar to the Magnus force responsible for the curved trajectory of a spinning baseball. In the

case of a spinning sphere, the surface pulls air within the boundary layer as it spins, thus creating circulation. As the ball translates in the air, the circulation increases the total flow velocity on one side of the sphere and decreases the velocity on the other side. A low-pressure region created by the greater velocity on one side pulls the ball in that direction [22]. If the wing pronates prior to reversing direction at the end of the upstroke then the leading edge rotates backward relative to translation producing an upward component of lift (backspin). If pronation occurs after the reversal of directions the rotational force will actual create a downward force. Furthermore, the viscous force within air will makes the flow above and below a flat wing fuse smoothly at the sharp trailing edge, as previously explained in Sec. 2.3, i.e. the Kutta condition. This attempt to re-establish the Kutta condition creates additional circulation around the wing, thus increasing the lift. The Kutta reestablishment is not instantaneous, so if the wing is continually rotating it may never be fully realized, but the tendency to re-establish this Kutta condition will still lead to greater circulation. Fig. 2.6 show an illustration of the rotational force mechanism.

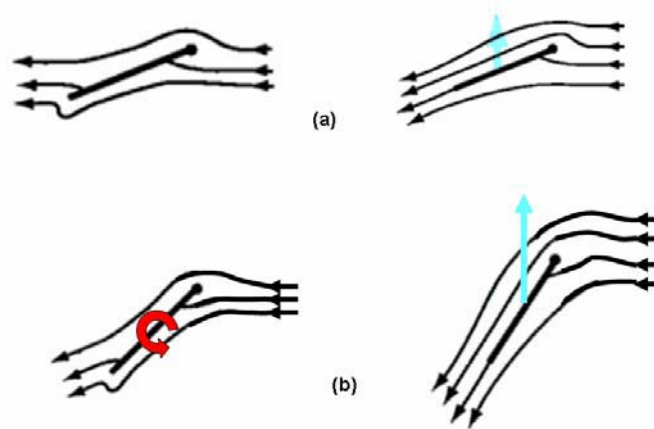


Fig. 2.6: The figure show how the rotation of the wing can develop lift. In (a) the wing is experiencing lift because of the Kutta condition, as the wing rotates the air on the top side of the wing is accelerated re-establishing the Kutta condition. It is important that wing be rotating, because at the new steeper angle the flow would separate from the wing.

2.4.3 Virtual Mass Effect/ Added Mass Effect

The virtual mass effect or added mass effect is caused by the translational or rotational acceleration of fluid flow surrounding the wing. The force needed to accelerate the mass of air is primarily a function of wing orientation; this force is a minimum when the wing chord is oriented parallel to flow and maximum when the wing chord is perpendicular to the flow. The wing translational acceleration is much greater than the rotational acceleration. Furthermore, the translational accelerations are greatest at the end of the wing half strokes consequently the virtual mass effect is greatest there. Virtual mass is a non-circulatory force and can be modeled as the mass of a cylindrical volume of air surrounding the wing chord with an equal diameter to the chord at every location as one moves along the wingspan from root to the tip [29].

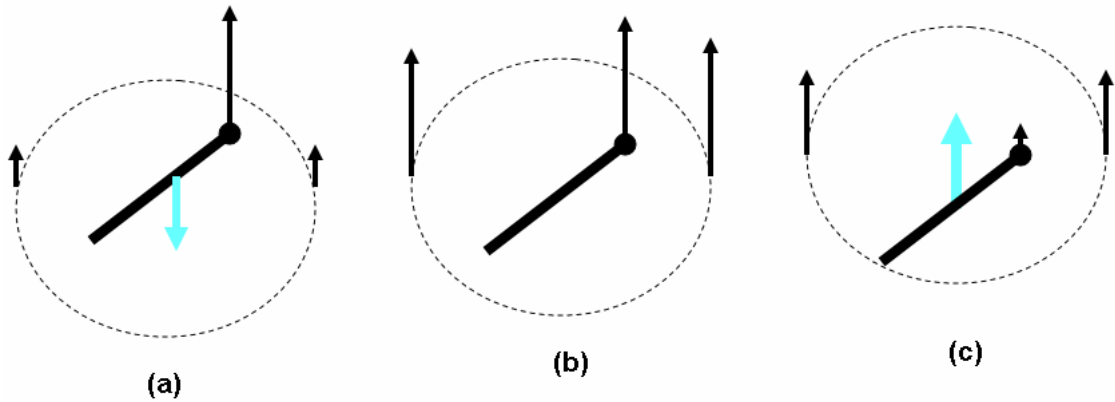


Fig. 2.7: This shows the virtual mass effect. A cylinder of air is assumed to be attached to the wing as seen in (a), (b), and (c). When the wing accelerates the mass of air resists the motion (a) but once the mass of air is moving at the same velocity as the wing there is no force (b). When the wing decelerates the mass of air acts as a force to keep the wing in motion (c).

2.4.4 Wake Capture/Wing Wake Interaction

The wake capture mechanism, or wing wake interaction, as the name implies, takes advantage of the wake generated by the wings in their previous stroke. PIV images suggest that wing supination just prior to the end of the up stroke shed leading and trailing edge vortices (TEV and LEV) creating an inter-vortex stream directed towards the ventral wing surface, giving added lift. The greater the circulation produced by the wing at the end of the half stroke, the greater the inter-vortex stream. Fig. 2.8 illustrates how this mechanism might work. The wing wake interaction was first observed by Dickinson (1994) during flow visualization experiments on a 2-D inclined plate [32]. Flow visualization and force measurements of a 3-D mechanical model of a fruit fly revealed a similar phenomenon [33] as well as smoke trail visualization of freely flying butterflies [34]. Sun and Tang (2002) also

performed CFD simulations on wing kinematics [35] similar to those of Dickinson (1999) and found results that contradicted the Dickinson hypothesis [1]. Sun believes the force peak, observed by Dickinson, are due to acceleration of the wing rather than wing-wake interactions. As of now the discrepancy between the CFD model of Sun and Tang and the flow visualization of Dickinson has not been resolved and the effect of wing-wake interaction is still largely unknown.

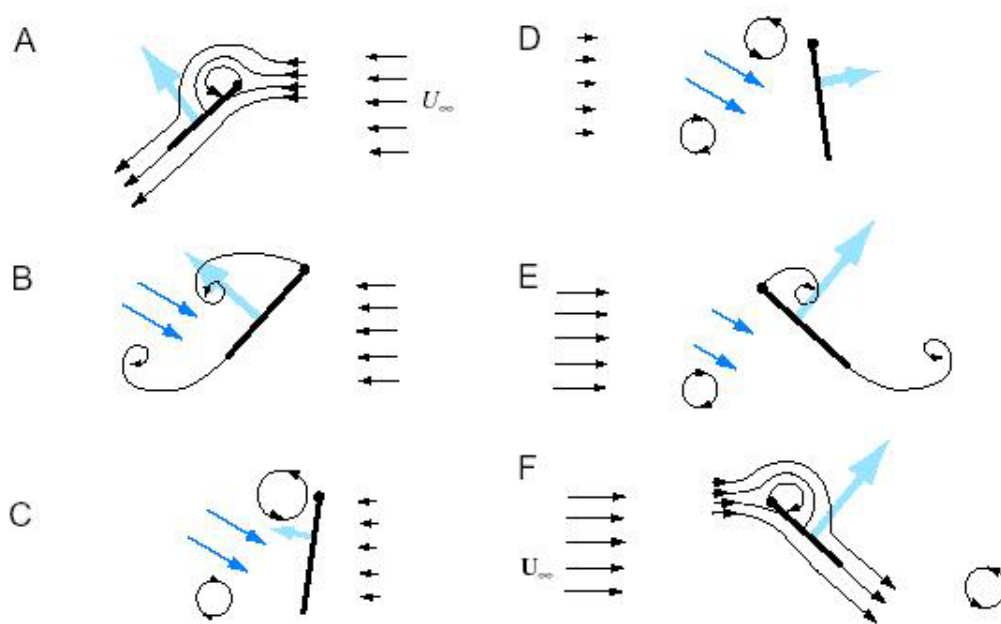


Figure 2.3: In the wake capture mechanism LEV and TEV shed from the wing as seen in (a)-(c) interact with the wing as it reverses directions (d)-(e), this interaction can lead to increase of lift, (Fig. borrowed from [2]).

2.4.5 Clap and Fling Effect

The clap and fling effect, first observed by Weis-Fogh in the Chalcid wasp, describes an interaction of the near touching or touching of wings during the end of the wing stroke [36]. In some insects, the wings actually touch or clap together during flight. The leading edge of each wing collides first, followed shortly by the trailing edge progressively closing the gap. The clap and fling mechanism has two effects: (i) A jet of air is created caused by the squeezing together of the two wings. (ii) As the wings press together, the trailing edge vortex of each wing collide, canceling each other out, this reduces or eliminates the trailing edge vortex at the beginning of the new stroke. Trailing edge vortices, present at the beginning of a stroke, delays the growth of LEV. Without these vortices, circulation grows more rapidly and increases the beneficial lift of LEVs. Also, because the leading edge separates first, leaving the trailing edge still attached, it creates a low-pressure zone. Air flows to fill the gap as the leading edge separates, helping to create circulation of the attached vortex. The net circulation around the entire systems remains at zero though satisfying Kelvin's law [22] [23]. Figure 8 shows a visualization of the clap

fling effect.

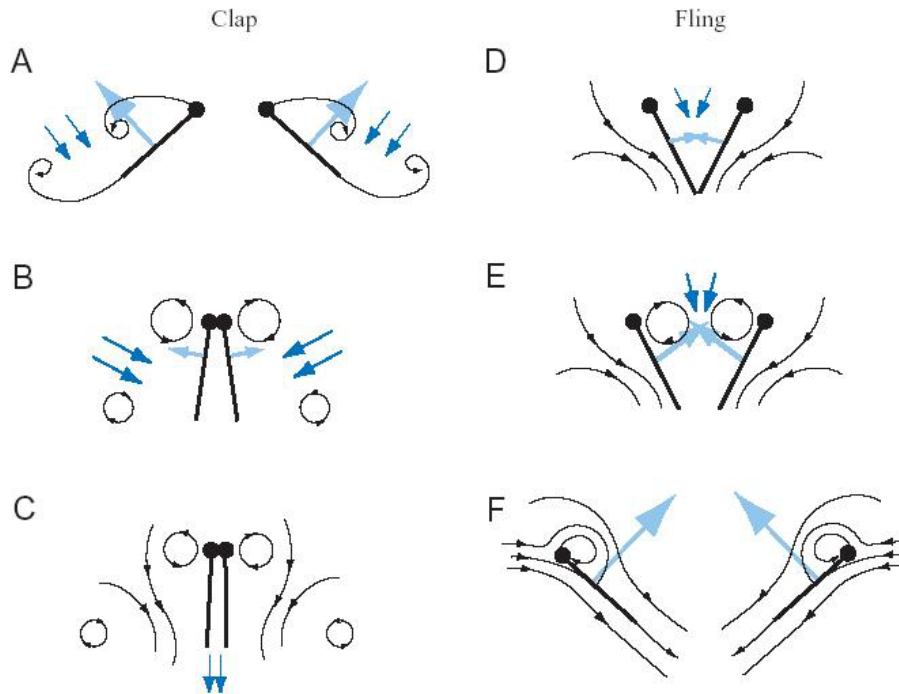


Figure 6: This shows how the clap and fling mechanism might operate. At the end of the stroke the two wings collide canceling or partially canceling out TEV. TEVs delay the growth of LEVs at the beginning of the stroke, LEVs increase circulation over the wing increasing lift. Also as the two wings collide they produce a jet of air that helps increase lift. Fig. borrowed from [2]

2.4.6 Quasi-Unsteady model

The quasi-unsteady model used in this thesis was developed at the University of Delaware. This model was built from the work of a number of prominent researches including Ellington, Dickinson, Delaurier and Walker [37] [38] [39] [40]. The quasi-unsteady model adds the steady state effects discussed in Sec. 2.4 to the unsteady state effects as shown in Eq. (2.5).

$$F_T = F_{steady\ state}(\dot{\phi}) + F_{unsteady\ state}(\dot{\phi}, \dot{\psi}, \ddot{\phi}, \ddot{\psi}), \quad (2.5)$$

where F_T is the total instantaneous force on the wing, $F_{steady\ state}$ are the steady state forces, and $F_{unsteady\ state}$ are the unsteady state forces. The instantaneous force, F_T , can also be written as a sum of the steady and unsteady aerodynamic mechanisms.

$$F_T = F_{steadystate} + F_{LEV} + F_{rotation} + F_{virtualmass} + F_{wakecapture} + F_{clapfling} \quad (2.6)$$

In the UD model, the clap fling and wake capture effects are ignored. Also, because the attached LEV is present in steady revolving wings, where each wing section undergoes translational motion with constant velocity, F_{LEV} is lumped with the $F_{steadystate}$ force [38] [39]. The remaining terms are written as a product of a function which captures the physics of the phenomena and an experimental coefficient that adjusts the scaling or magnitude of the force which varies for different shapes [41].

The total aerodynamic force including the LEV, rotational, and virtual mass effect can be written as

$$F_T \cong C_1 \frac{\rho}{2} \int_0^R |\bar{u}(r,t)|^2 c(r) dr + C_3 \frac{\rho\pi}{4} \int_0^R \dot{u}_n(r,t) c(r)^2 dr \quad (2.7)$$

Here, the rotational and translational forces are combined as the first term in the above equation. C_1 and C_3 are the coefficients of LEV and virtual mass force respectively. The coefficient of rotational force, C_2 , appears implicitly in $u(r,t)$, $c(r)$ is the chord length at distance, r , from the root, \bar{u} and \dot{u} are the total flow velocity and the rate of change of the normal velocity component at the local wing mid-chord respectively [41]. Using the BEM presented in Sec. 2.3 and 2.4, the total force F_T on the wing is obtained by integrating the forces at ever section of wing.

2.5 Summary

This chapter discussed the current theory in flapping wing aerodynamics. It explained the various flow patterns, or aerodynamic mechanisms, generated by flapping wings, and how these mechanisms can improve the performance of flapping wings. The chapter went on to discuss the analytical models used to quantify flapping wing lift generation. One such analytical model developed at the University of Delaware, was discussed in detail. This model will be incorporated into a full dynamic model of the prototype ornithopter discussed in Chapter 4.

Chapter 3

MECHANICAL HUMMINGBIRD PROJECT (MHP)

3.1 Introduction to the Mechanical Hummingbird Project

The majority of ornithopters in existence rely on a simple up and down flapping as in larger birds. These mechanisms that drive these ornithopters usually rely on some sort of four-bar mechanism. In the Mechanical Hummingbird Project these concepts are built on but extra components are added to give the mechanism's wings a second degree of motion. This chapter discusses the goals for the prototype ornithopter created for this thesis. It also gives a detailed description of the prototype mechanism and how it accomplishes these goals. Finally, it discusses how the wing kinematics developed by the prototype attempts to use the aerodynamic mechanisms discussed in Chapter 2.

3.2 Hummingbird Inspiration

In 2002, the University of Delaware Mechanical Systems Laboratory began research and development on flapping wing vehicles. After the creation of a number of successful forward-flying ornithopters, the group began the ambitious task of creating a hovering ornithopter. This new endeavor, the Mechanical Hummingbird Project (MHP), attempts to emulate the size and ability of the hummingbirds. Hummingbirds can hover steadily, feeding for minutes at a time. They can negotiate through foliage while avoiding predators. They are lightweight and energy efficient.

Furthermore, hummingbirds are one of the larger animals capable of sustained hover. The largest hummingbird, the Giant Andean (*Patagona gigas*), has a wingspan of 13.5 cm. Construction of a MAV at a hummingbird scale is much more feasible than an insect scale. Also, even though the sizes of electrical actuators, sensors, and other accessories have reduced drastically, they are not small enough to fit into an insect size vehicle.

Hummingbirds inspire the MHP, but it was never our intention to replicate the mechanics of the hummingbird. Muscles, acting as linear actuators, operate the intricate skeletal mechanisms that flap and feather the wings of hummingbirds. These muscles are very efficient at generating the hummingbird's complex wing motions. Unfortunately, technology has not advanced to a point where synthetic linear actuators are as light and strong as hummingbird muscles. There have been notable developments and applications of certain new linear and bending actuators. For example, the MFI of UC Berkeley uses reciprocating piezoelectric actuators that bend to create wing motion. However, these actuators require a significantly higher voltage than what the typical batteries on a MAV can produce. Also, certain metal alloys, referred to as memory wire, can expand and contract under changes in temperature. Passing an electrical current through a memory wire can heat it to expand or contract the metal. This technology has been successfully used in actuating control surfaces but is inadequate to create the large motions necessary for flapping wings. The most feasible actuators, in our opinion, are small electric DC motors. However, motors create rotary motion which needs to be changed to reciprocating motion to flap the MAV wings. This requires some ingenuity in design. The remainder of this chapter discusses one such novel mechanism, designed to turn the rotary motion of a small

electrical motor into a reciprocating motion of the wing around multiple axis for use in a MAV.

3.3 Goals of the MHP

The major goal of the MHP is to create a flapping wing vehicle with the size and capability of a hummingbird, with the most important capability being the ability to hover. The decision to create a flapping wing vehicle came in part from the aerodynamic inefficiencies observed in small fixed and rotary wing aircraft. However, the major inspiration comes from the enormous number of biological species that show the efficiency and agility that flapping wing MAVs can achieve. Another goal, derived from the observation of insects and hummingbirds, is to create a vehicle where the wings can rotate about multiple axes and make use of the aerodynamic mechanism described in Chapter 2. The MHP, similar to insects and hummingbird, can both flap and feather its wings. Reduction of weight is another major concern, and since the motor is a major source of weight, our design uses a single motor to drive the flapping and feathering of both wings.

In order to achieve these goals, our research group has designed several possible flapping mechanisms. A flapping mechanism designed before the MHP is shown in Fig. 2.1. Like the MHP, it uses a single motor to both feather and flap the mechanism wings. The mechanism relies on two sprockets of unequal size driven by a single motor, connected by a chain. The wings are attached to a point on the large sprocket by a ball and socket joint and are supported in a second location by an eyebolt. This mechanism creates a figure of eight motion of the wing. However, feathering and flapping are not optimized to create substantial lift. Also, the

mechanism needs to be minaturized in order to create a hummingbird scale design [43].

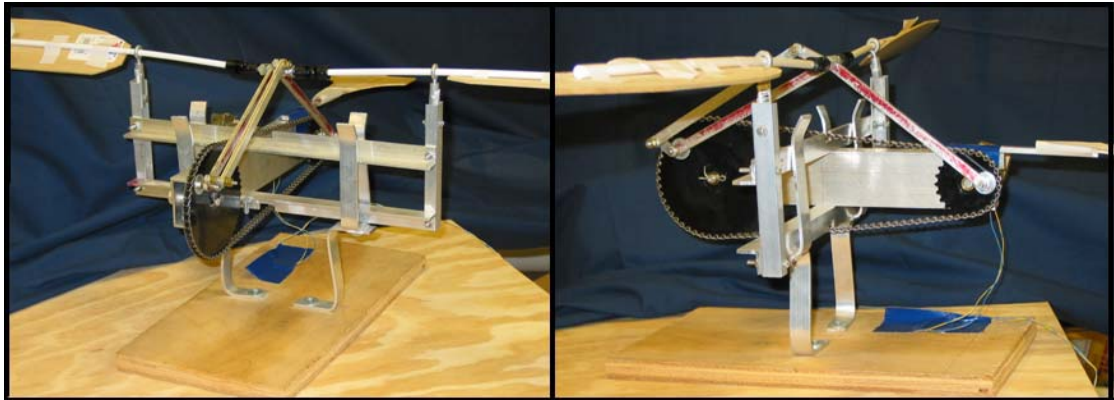


Figure 3.1: An early prototype developed at the University of Delaware that creates a multi-oscillatory wing motion using a single motor.

The MHP design has proceeded in a different direction evolving from our experience in building forward flying ornithopters, such as Sparrow II, as previously described in Fig. 1.4b. These ornithopters utilize a 4-bar mechanism, actuated by a single motor, to create a single axis flapping motion. The 4-bar mechanism is a successful design and has been reliably used by other ornithopters, including the Slow Hawk II and Microbat (previously described in Figs. 1.4 a and c). The 4-bar mechanisms used in these designs lack control over wing feathering. MHP improves on these designs by using a system of cams and springs along with the 4-bar mechanism to create both flapping and feathering. This mechanism lends itself quite well to creating a wing motion similar to birds and insects. Sec. 3.3 describes the details of how the mechanism works. Figure 3.2 shows a CAD illustration of the final

iteration of the mechanical hummingbird project, named MHP III. Fig. 3.3 shows the parameters of the wings.

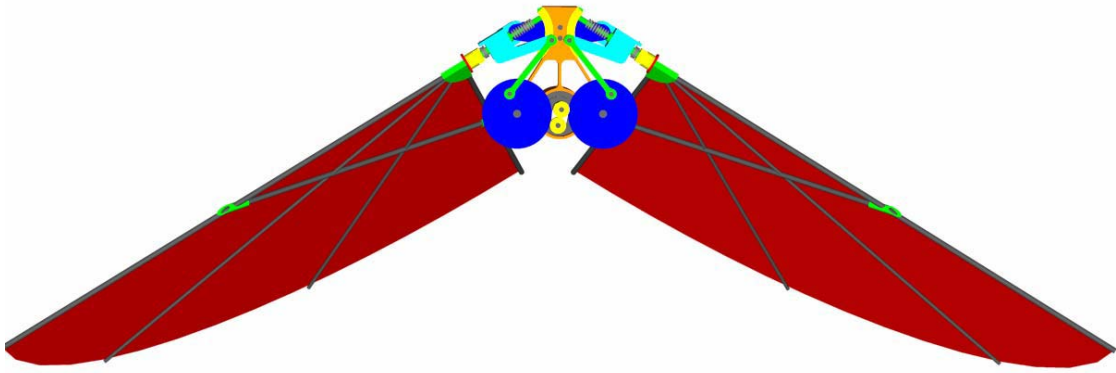


Figure 3.2: Illustration of MHP III, featuring a novel mechanism to drive the flapping and feathering motion of the vehicle's wings. The wings are driven by a single motor that operates two symmetric 4-bars which in turn operate two symmetric cam/follower mechanisms.

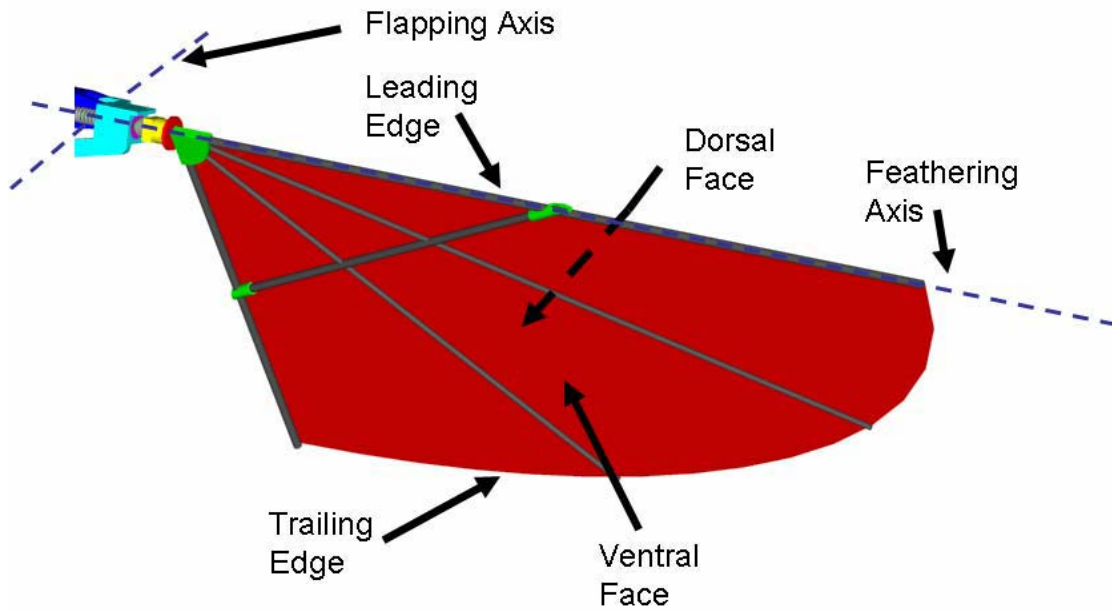


Figure 3.3: This shows some important features of the wing, namely the flapping and feathering axes.

3.4 Mechanism Operation

The flapping mechanism, of the MHP ornithopters, creates the same two major wing motions observed in insects and hummingbirds: flapping and feathering. The flapping and feathering motion are shown in Fig. 3.4. Since the physical mechanism uses a single actuator, the flapping and feathering motions are coupled. A novel combination of a 4-bar mechanism, similar to that used for the forward flying ornithopters, and a system of cams and springs allows for such a coupling. The entire vehicle consists of over fifty precisely manufactured parts. Some parts came from various outside vendors, but the majority of the parts were machined in-house at the University of Delaware Machine Shop. A complete listing of each part and assembly

procedures can be found in Appendix B. Fig. 3.5 A and B show labeled illustrations of the mechanism's various parts.

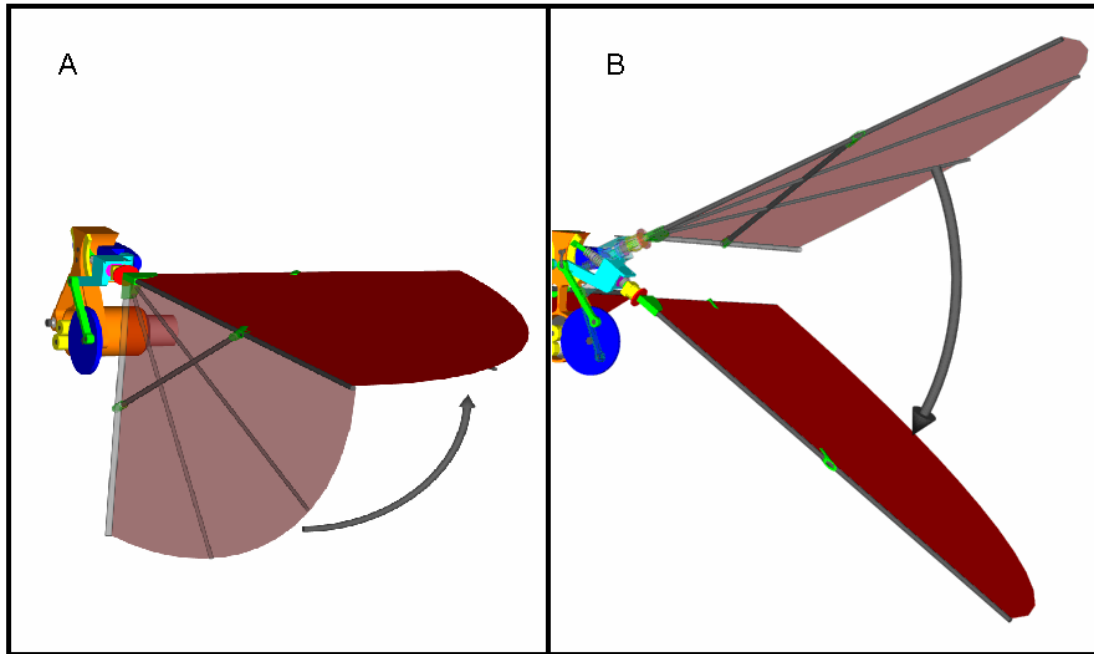


Figure 3.3 A shows the feathering motion of MHP III—the wing moves from the supinated position (semi-transparent) to the pronated position. B shows the flapping motion of MHP III. The wing is in a fully pronated position as it moves through the downstroke.

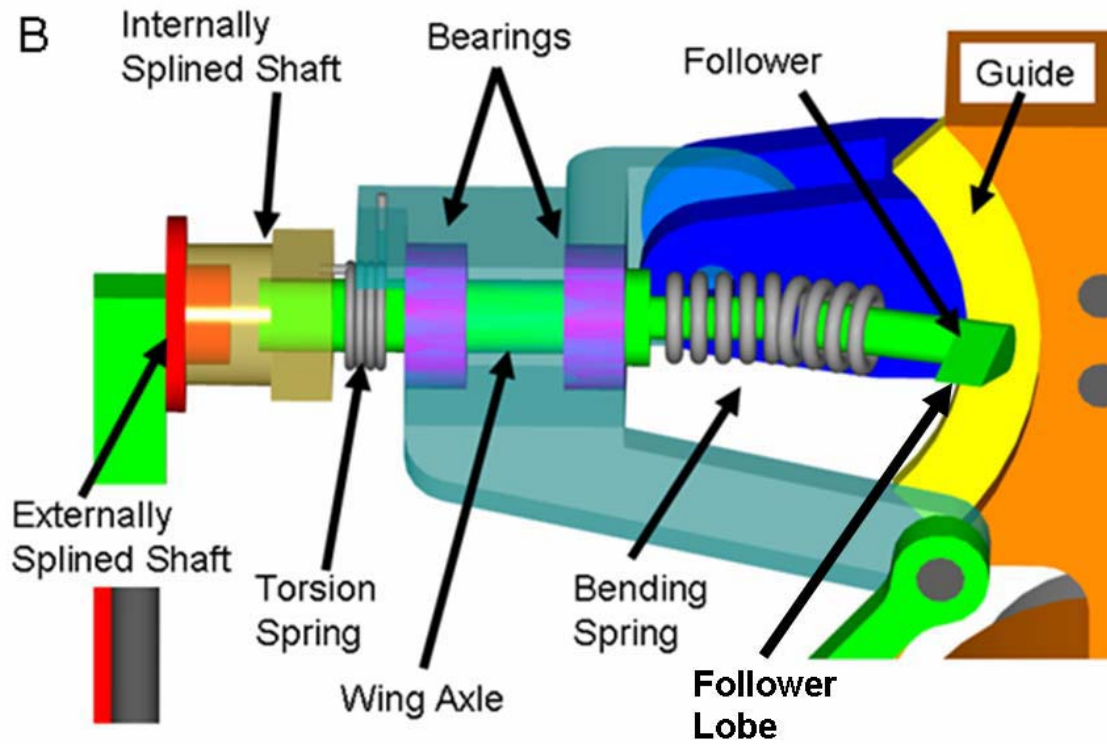
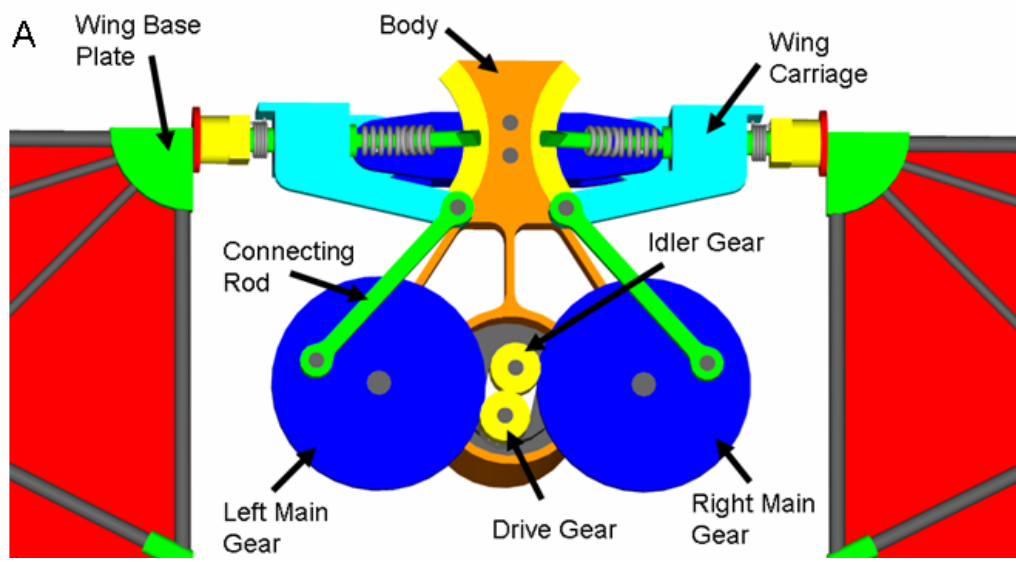


Figure 3.4: A shows a schematic of the parts in the flapping mechanism of MHP III. B shows a closer look at some of the parts in the flapping mechanism. A detailed list of these parts and assembly procedures appear in Appendix B.

The flapping mechanism operates as follows: Two four-bar mechanisms create the flapping motion of each wing. A main gear, a connecting rod, a wing carriage, and the body make up each four-bar. The drive gear rotates the left main gear, while the idler gear rotates the right main gear. The drive gear attaches to the end of the motor shaft and meshes with the idler gear; this arrangement ensures that the two main gears rotate in opposite directions and at equal speeds. The two main gears, supported by bearings pressed into the body, act as the cranks in the four bar mechanisms. A connecting rod is pinned to each main gear, with the other end of the connecting rod pinned to its respective wing carriage. The wing carriage rotates on a separate pin, again supported by bearings pressed into the mechanism body, thus completing the four-bar. As the main gears rotate the connecting rods move up and down rotating the wing carriages, supporting the wings, and consequently flapping the wings. Figure 3.5a and b shows a schematic of this four-bar arrangement and the resulting wing motion.

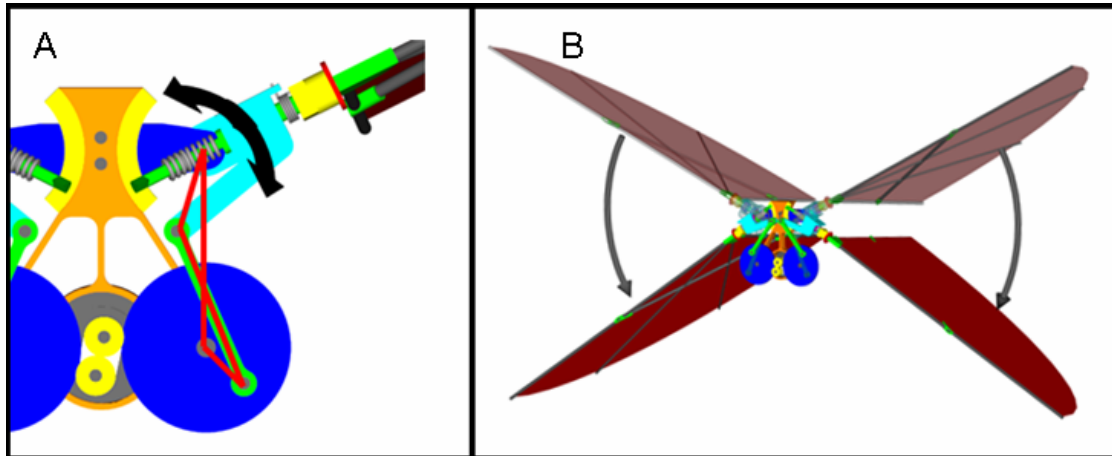


Figure 3.5: A shows the reciprocating motion created by the 4-bar mechanism, with the geometric link lengths shown in red. B shows the flapping motion of the wings generated by the 4-bar mechanism.

The feathering mechanism operates as follows: The wing carriage supports the wing axle. The wing axle, supported by two bearings, fits in a cylindrical shaft in the wing carriage. The wing axle is free to rotate within the shaft but stops prevent it from translating linearly. The wing connects to the outside end of the axle and the follower attaches to the inside end of the axle. The follower performs as its name suggests and follows along the surface of the guide, as shown in Fig. 3.6. At the very end of the follower is a lobe, the follower will contact the guide on either the lobe side or the non-lobed side depending on where it is in the stroke. The follower attaches to the wing axle via a bending spring, in reality the bending spring is a compression spring but it acts in bending so the more descriptive term is used. The bending springs allow for a slight misalignment of the follower axis with the wing axle axis. It also supplies a restoring moment to bring the follower axis back in alignment with the wing axle axis. A second spring, the torsion spring, wraps around the outside end of the wing axle. The inner wire of the torsion spring attaches to the

wing carriage and the outside wire attaches to the wing. When the wing supinates, the torsion spring applies an opposing moment that seeks to pronate the wing to its original position.

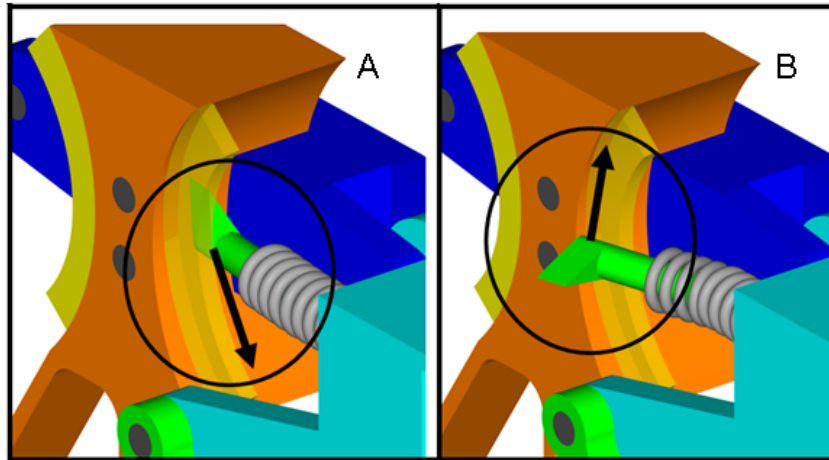


Figure 3.6: A shows the lobe end of the follower moving down the backside of the guide, putting the wing in a supinated position. Fig. B shows the non-lobed end of the follower moving up the front side of the guide, putting the wing in a pronated position.

The guide is a narrow ridge attached to the body of the ornithopter and positioned so that it lies in the path of the follower. A key feature of the guide is that its top edge lies slightly in front of the follower axis and its bottom edge lies slightly behind the follower axis. When the wing is at the bottom of the down stroke, the follower is slightly above the guide, with the follower lobe facing forward and horizontally. As the wing rotates upward, the follower rotates down and the follower lobe contacts the guide. Because of the guide's slant, the contact point is slightly in front of the follower axis. This contact force creates a moment supinating the wing.

As the follower slides down the guide, the bending spring deflects and forces the follower to stay in contact with the guide. Near the end of the upstroke, the follower moves below the guide. The torsion spring releases, pronating the wing to its original position, and the bending spring re-aligns the follower axis with the wing axle axis. The follower then begins to move upwards and contacts the guide a second time. Now on the down stroke, the non-lobed end of the guide contacts the follower, this time slightly behind the follower axis. The non-lobed side does not create a supinating moment, consequently the torsion spring remains un-stretched and the wing stays in its pronated position. The bending spring, however, does deflect keeping the follower in contact with the guide. Near the end of the down stroke, the follower moves above the guide, releasing the bending spring to its original position. Fig. 3.7 shows a schematic of this process.

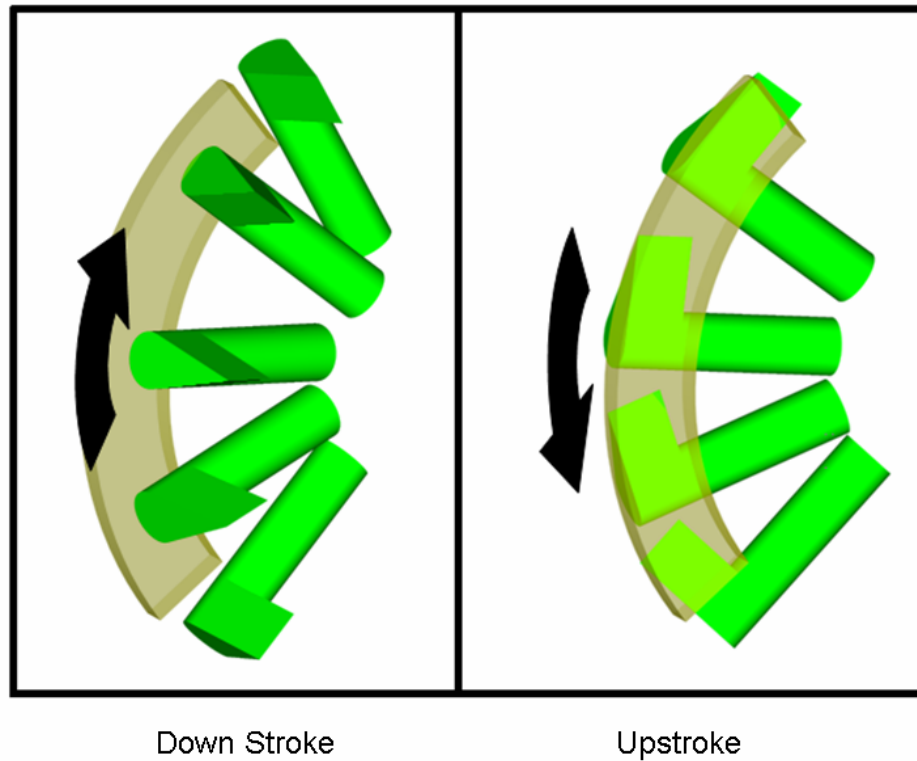


Figure 3.7: This shows the motion of the follower along the guide. During the down stroke the follower moves up along the front of the guide. During the upstroke the follower moves down along the backside of the guide. Note that the motion of the follower is always opposite to the motion of the wing, as it moves down the wing moves up and vice versa.

The wing orientation moves with the follower orientation. This relationship is fixed, however the initial orientation of the wing with respect to the follower is adjustable. This is possible because of an internally splined shaft that attaches to the outside end of the wing axle. The inside base of the wing has a mating externally splined shaft. These two shafts fit together to form the connection between the wing and the wing axle. Changing the initial orientation of the wing will change the overall wing kinematics. In the original design, the wing plane remained

perpendicular to the stroke plane during the down stroke, then supinated for the upstroke. This does not necessarily create the greatest lift. With the wing adjustability, the wing kinematics can be adjusted to measure the corresponding lift. The wing still feathers by the same amount for the upstroke and down stroke, but its angle with respect to the stroke plane will be different. Fig. 3.8 shows a photograph of these two mating features.

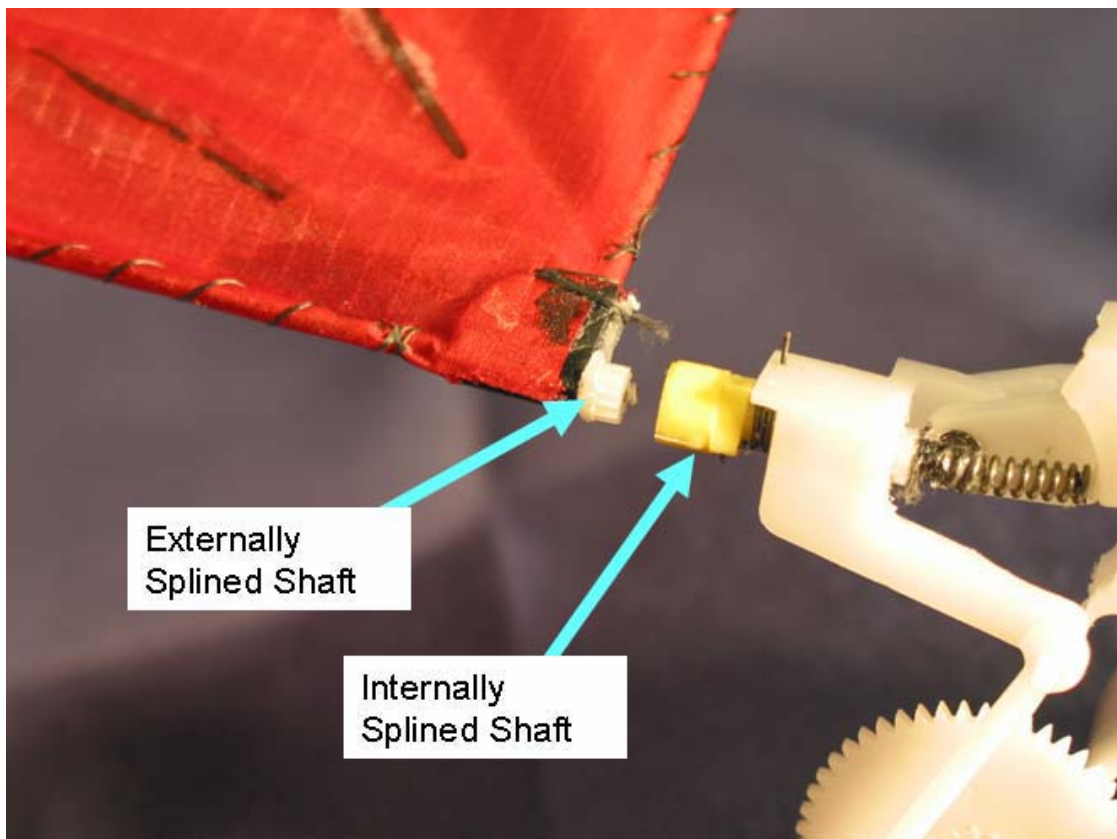


Figure 3.8: This shows the mating externally and internally splined shafts that allow for different initial orientations of the wing with the follower.

3.5 Wing Kinematics

The original wing motion envisioned for the MHP is as follows: During the down stroke the wing plane remains horizontal (fully pronated), at the end of the half stroke the wing is very quickly supinated as close to 90 degrees as possible. The wing remains in this position throughout the upstroke and then very quickly pronates to begin the downstroke. During the down stroke a positive lift force is generated and during the upstroke a negative lift force is generated. Because the wing is supinated during the upstroke its effective surface area is less than during the down stroke. Consequently the wings generate more positive lift during the down stroke than the negative lift generated during the upstroke, creating a net positive lift. Physical constraints of the mechanism lead to a supination angle of closer to 45 degree. Fig. 3.9 shows the motion generated by MHP III, with the blue lines showing the predicted lift forces.

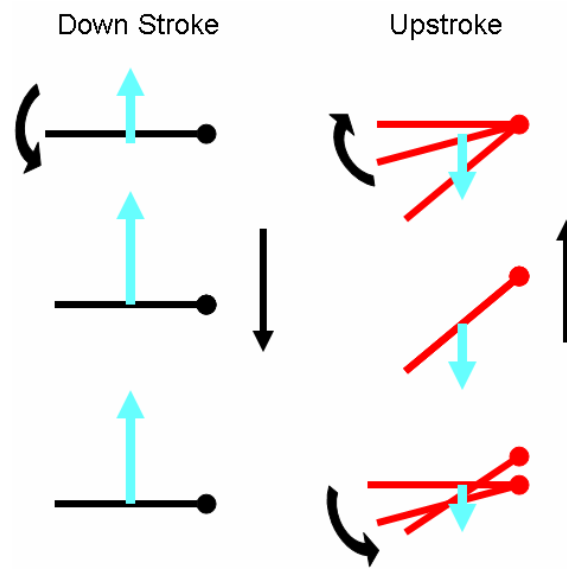


Figure 3.9: This is the desired wing motion of MHP III. A positive lift force shown in blue is generated during the down stroke when the wing is pronated. During the upstroke the wing produces a smaller negative force while in a supinated position. Consequently there is a net positive lift force.

As mentioned in the previous section, the flapping motion and the direction and magnitude of the feathering rotation are fixed. However, the initial feathering angle of the wing is adjustable. This allows for different wing kinematics. Fig. 3.10 shows different possible wing paths. However, experimental and theoretical data was only collected for the kinematics shown in Fig. 3.10 A.

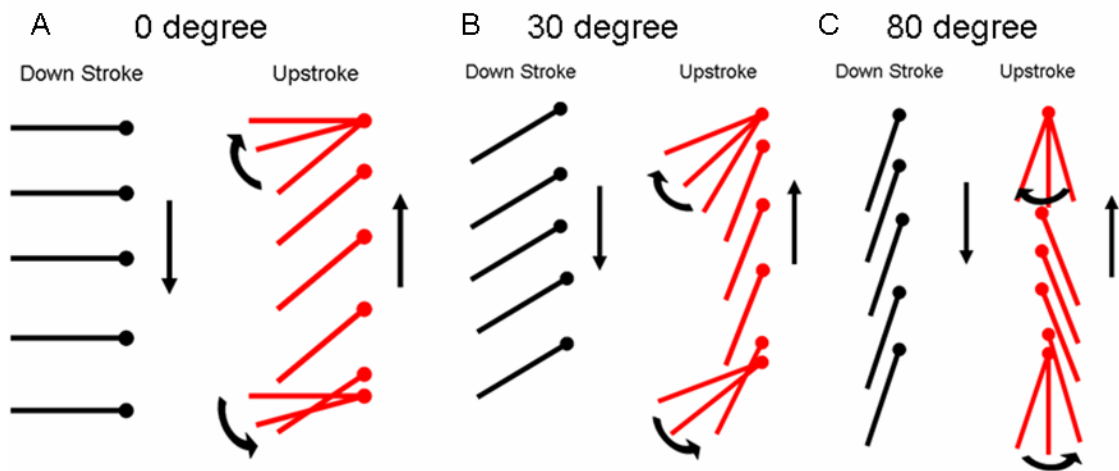


Figure 3.10: This shows the wing motion for different initial feather angles. **A** moves in an asymmetric motion and has an initial feather angle of 0 degrees and is the focus the experiments. **B** and **C** show initial feather angles of 30 and 80 degrees respectively. **C** is similar to the symmetric wing motion of flies.

The wing motion in Fig. 3.10 C is similar to the wing motion of flies, except the fly stroke plane is in a horizontal position. The advantage of this motion is that the wing can produce a positive lift in both the upstroke and down stroke. Fig. 3.10 shows experimental measurements of a model fly wing, the black line shows the motion of the wing and the red line is its resultant force vector. For the fly's wing motion the net force remains vertical throughout the up and down stroke [22]. This thesis does not study the effects of the symmetric wing motion of MHP III, but it is definitely a subject deserving future work.

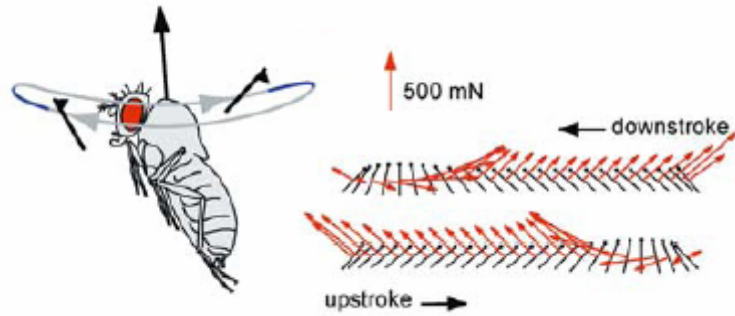


Figure 3.11: This shows the motion of a fly’s wing. The stroke plane is oriented horizontally and the net force of the wings in both the up and down stroke is vertical. Illustration adapted from [1]

3.6 Specifications of MHP III

MHP III has a wing span of 48 cm and it weighs approximately 50 grams. It can flap its wings up to 6 Hz with using an average power of 1.22 watts. Fig. 3.11 shows a dimensioned drawing of MHP III. For a detailed list of MHP parts, specification, and manufactures see Appendix C.

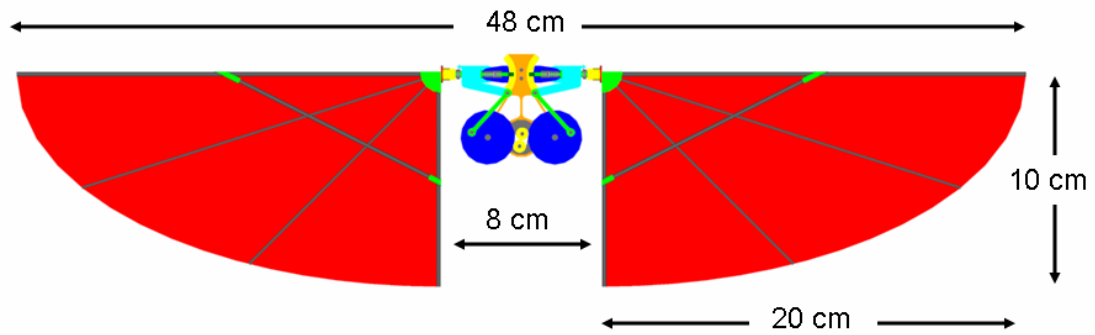


Figure 3.5: Dimensioned illustration of MHP III. It weighs 50 grams and has a maximum flapping rate of 6 Hz.

3.7 Summary

This chapter has described the operation of the MHP III prototype and detailed its characteristic parameters. Furthermore, it has discussed how the wing motion generated by MHP III, attempts to create positive lift. The subsequent chapters will analyze the mechanism theoretically and experimentally to quantify how well the MHP prototypes accomplish their desired goals.

CHAPTER 4

THEORETICAL ANALYSIS OF THE MHP

4.1 Introduction

In designing the flapping mechanism, it is important to predict the kinematics and dynamics of the system in order to improve the design. For this reason, a dynamic model of the flapping mechanism for the MHP ornithopters was created using MatlabTM. The theoretical model captures the major factors governing the system and allows for observation of critical forces and moments acting on the mechanism. The model is a tool to help improve the mechanisms design. Mechanism parameters can be varied to see the effects on its performance. The performance of the mechanism is judged mainly by the power usage and the aerodynamic lift generated. As one would expect, it is preferable to gain the most lift using the least power.

4.2 Model Simplifications and Assumptions

For ease of computation, a number of alterations and simplifications were made in developing the mathematical model. In the physical model, the joint attaching the follower to the body is made up of two revolute joints perpendicular to one another (the wing axle and the wing carriage axle), with a third joint created by the bending spring. This complex joint is replaced by a single spherical joint in the computer model. The location of this joint is approximately where the center line of

the wing carriage axle and the wing axle intersect. In addition, unlike the physical model, the follower and the wing are considered as one rigid body. Fig. 4.1 shows the physical joint and the theoretical joint used to replace it. To reconcile this discrepancy with the physical model the bending spring and the reaction moment generated by the wing carriage bearings are combined into a single reaction moment, M_{BS} . This moment acts to re-align the follower/wing into the stroke plane, as shown in Fig. 4.1. The final major assumption is neglecting friction.

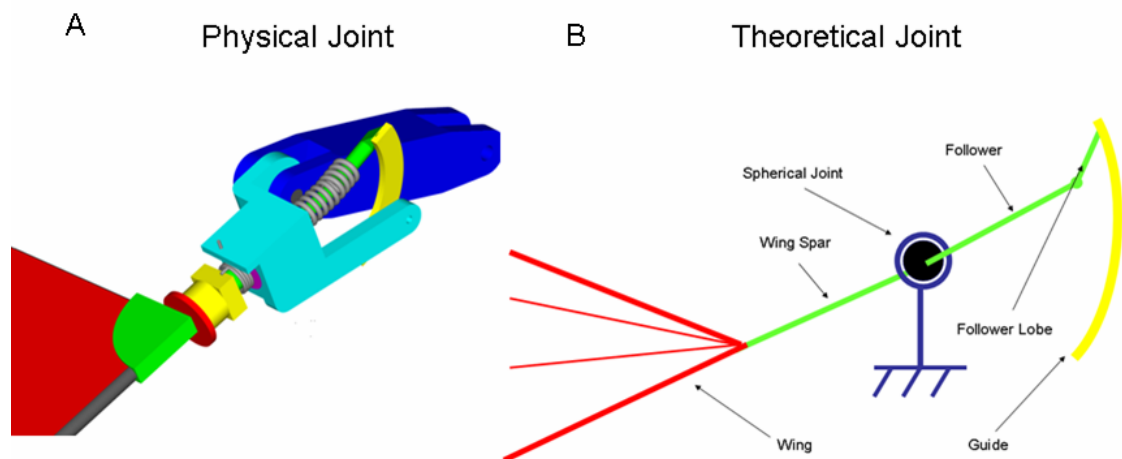


Figure 4.1: A shows an illustration of the physical joint contrasted with B an illustration of the theoretical joint.

4.3 Reference Frames

Two reference frames are identified in the theoretical model, an inertially fixed reference frame, reference frame \mathcal{E} , attached to the mechanism body with an origin, o , located at the wing pivot of the aircraft. And a second reference frame,

reference frame \mathcal{F} , which is attached to the follower/wing with the same origin, o . The axes \hat{x}_o, \hat{y}_o , and \hat{z}_o correspond to reference frame \mathcal{E} with the flapping plane coinciding with the $\hat{y}_o - \hat{z}_o$ plane. The \hat{x}_o axis is the flapping axis of rotation. The axes \hat{x}_w, \hat{y}_w , and \hat{z}_w correspond to reference frame \mathcal{F} . The \hat{y}_w axis corresponds with the leading edge wing spar and is the feathering axis of rotation. Furthermore, the $\hat{y}_w - \hat{z}_w$ plane is the plane of the wing surface.

In the physical model, the wing is free to rotate about two angles, ψ , the flapping angle, and ϕ , the feathering angle. Because of the modification made in Sec. 4.2 the wing now has three degrees-of-freedom, the flapping and feathering angle, and an out of flapping plane angle, θ . The out of plane angle will remain small throughout the wing's motion, approximating the motion of the physical model. Fig. 4.2 shows the reference frames of the theoretical model and the angles of rotation.

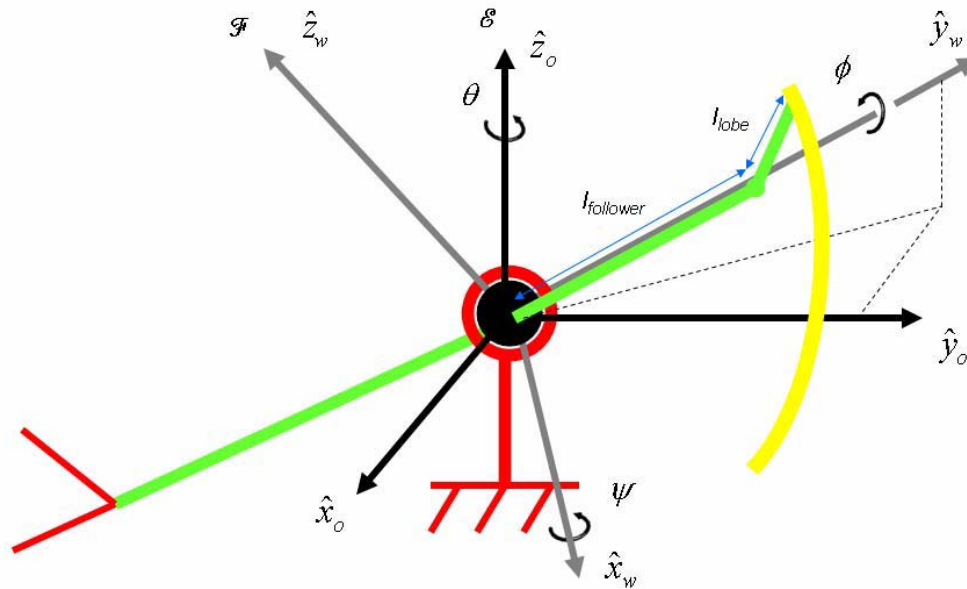


Figure 4.2: This shows the inertially fixed reference frame \mathcal{E} and the wing fixed reference frame \mathcal{F} . The flapping angle, ψ , the feathering angle, ϕ , and the out of plane angle, θ , are also shown.

4.4 Forces and Moments acting on the Mechanism

As mentioned in Sec 4.2, the theoretical model is a simplified version of the actual mechanism, but for the most part the forces and moments acting on the computer model replicate the forces and moments acting on the physical model. These force and moment vectors are as follows: \mathbf{F}_{AERO} —this is the summation of all aerodynamic forces acting on the wing, derivation of this force is further discussed in Sec. 4.5; it creates the aerodynamic moment \mathbf{M}_{AERO} . $\mathbf{F}_{\text{SUPPORT}}$ —this is the support force that holds the wing pivot fixed to the body. \mathbf{M}_{TS} —this is the moment generated by the torsion spring, it is simply a function of the feathering angle ϕ and the torsion

spring's stiffness constant k_{TS} . It acts along the \hat{y}_w axis. \mathbf{M}_{BS} —this is the moment generated by the bending spring and wing carriage support of the physical model. It is a function of the out of plane angle θ , and acts along the \hat{z}_w axis. Its apparent torsion stiffness constant k_{BS} . \mathbf{R} —is the reaction force of the guide contacting the follower and it creates the moment \mathbf{M}_{GUIDE} . The free body diagram of the follower/wing is shown in figure 4.3.

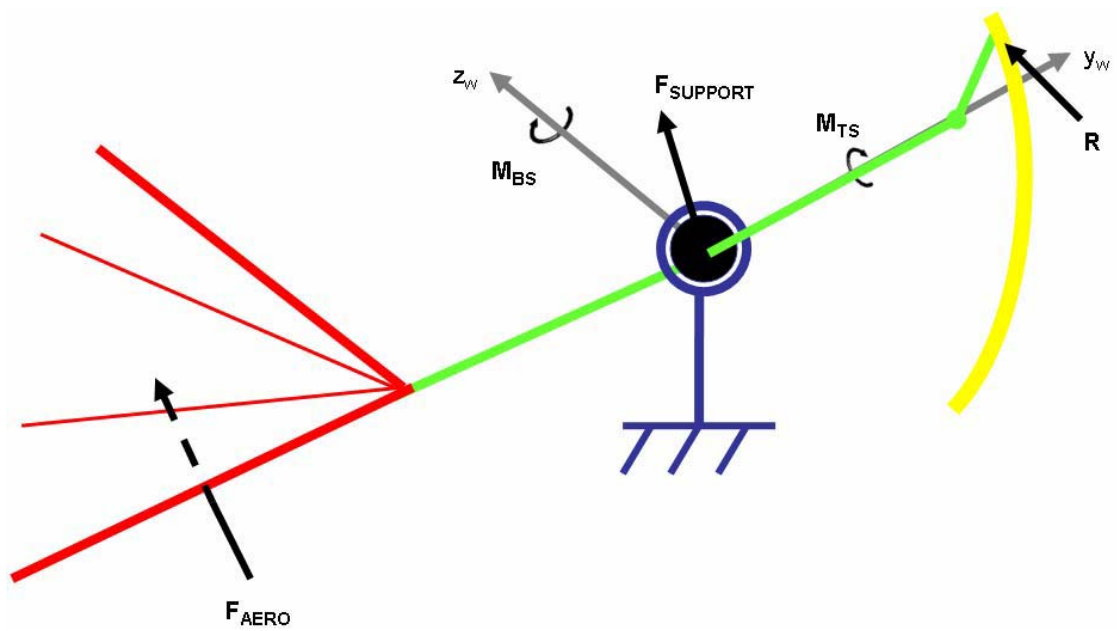


Figure 4.3: This is a free body diagram of the forces and moments that act on the flapping mechanism.

4.5 Aerodynamics of the Flapping Wing

The aerodynamic model presented in this text, as stated in Sec. 2.4.6, was developed at the University of Delaware. It is a quasi-steady state model and is a

function of the wing position and velocity. In the model, the wing is divided into n strips with the differential force of each strip computed separately. The formula for the differential force is as follows:

$$\Delta F = \frac{1}{2} C_1(\alpha_i) \rho \cdot c(r) \Delta r (V(d_i))^2 + C_3 \rho \frac{\pi}{4} (c(r))^2 \Delta r \cdot a, \quad (4.1)$$

where ΔF is the differential force acting normal to the chord of the wing at its cross section, ρ is the air density, r is distance from the wing base to the differential strip, $c(r)$ is the chord length at the corresponding length r , Δr is the thickness of the strip, $V(d_i)$ is the air velocity at a point on the wing strip 75% of the chord length, and α_i is the angle between the air velocity vector and the differential wing strip, and C_1 is an experimental coefficient. The first term in Eq. (4.1) calculates the translational force, including the leading edge vortex (LEV) force, and the rotational force. The second term is the virtual mass effect. Because of the relatively low flapping rate, the virtual mass effect is neglected. The total force is determined by summing each differential force of the wing. Fig. 4.4 shows a schematic of the parameters involved in the aerodynamic formula.

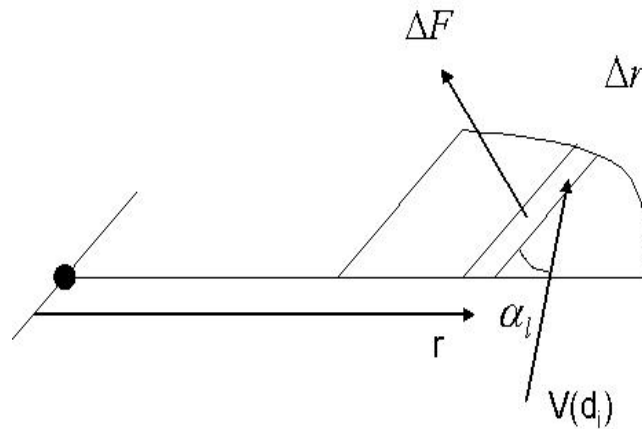


Figure 4.4: A differential aerodynamic force acting on a wing strip a distance r from the wing pivot. The differential force is created from the air velocity V contacting the wing at an angle α_i .

4.6 Solution Procedure

The solution was developed in the following way: The most critical forces are the aerodynamic lift and the input torque. Because the wing pivots about an inertially fixed location, it is only necessary to solve the moment equations about o in order to determine aerodynamic lift and input torque. This conveniently eliminates the $\mathbf{F}_{\text{SUPPORT}}$ term since it acts at the wing pivot. Also if we solve the problem in a coordinate system fixed to the follower/wing the inertia matrix of the follower/wing becomes constant, simplifying the calculations. The moment equation for the follower/wing is as follows:

$$\mathbf{I} \cdot \boldsymbol{\alpha} + \boldsymbol{\omega} \times (\mathbf{I} \cdot \boldsymbol{\omega}) = \mathbf{M}_{\text{BS}} + \mathbf{M}_{\text{INPUT}} + \mathbf{M}_{\text{GUIDE}} + \mathbf{M}_{\text{TS}} + \mathbf{M}_{\text{AERO}}, \quad (4.2)$$

where \mathbf{I} is the constant inertia matrix of the follower/wing about point o , $\boldsymbol{\alpha}$ is the angular acceleration vector, $\boldsymbol{\omega}$ is the angular velocity vector, and \mathbf{M}_{BS} , \mathbf{M}_{TS} , $\mathbf{M}_{\text{INPUT}}$,

\mathbf{M}_{AERO} , $\mathbf{M}_{\text{GUIDE}}$ are the external moment vectors described in Sec. 4.4. The reference frame \mathcal{F} is defined by a z-x-y rotation (also known as a 3-1-2 rotation) by the angles θ , ϕ , and ψ respective [42]. From the 3-1-2 rotation, the relationship between $\boldsymbol{\alpha}$ and $\boldsymbol{\omega}$ components and the reference angles θ , ϕ , and ψ can be written as follows:

$$\begin{aligned}\omega_{x_w} &= \dot{\theta} c_\psi s_\phi - \dot{\psi} c_\phi \\ \omega_{y_w} &= \dot{\theta} s_\psi + \dot{\phi} \\ \omega_{z_w} &= \dot{\theta} c_\psi c_\phi + \dot{\psi} s_\phi\end{aligned}\quad (4.3a, b, c)$$

$$\begin{aligned}\alpha_{x_w} &= -c_\psi s_\phi \ddot{\theta} + c_\phi \ddot{\psi} + (\psi s_\psi s_\phi - \dot{\phi} c_\psi c_\phi) \dot{\theta} - \dot{\phi} s_\phi \dot{\psi} \\ \alpha_{y_w} &= s_\psi \ddot{\theta} + \ddot{\phi} + \dot{\psi} c_\psi \dot{\theta} \\ \alpha_{z_w} &= c_\psi c_\phi \ddot{\theta} + s_\psi \ddot{\psi} + (-\psi s_\psi c_\phi - \dot{\phi} c_\psi s_\phi) \dot{\theta} + \dot{\phi} c_\phi \dot{\psi}\end{aligned}\quad (4.4a, b, c)$$

Substituting Eqs. (4.3 a, b, c) and (4.4 a, b, c) into Eq. (4.2), and then separating the first order and second order derivatives of θ , ϕ , and ψ , the moment equation can be rewritten as follows ,

$$\mathbf{A} \begin{Bmatrix} \ddot{\theta} \\ \ddot{\psi} \\ \ddot{\phi} \end{Bmatrix} + \mathbf{B} + \mathbf{C} = \mathbf{M} \quad (4.5)$$

Here, \mathbf{A} and \mathbf{B} are matrices containing only zeroth order θ , ϕ , and ψ terms, \mathbf{C} is the $\boldsymbol{\omega} \times (\mathbf{I} \cdot \boldsymbol{\omega})$ term, and \mathbf{M} is the summation of all external moments written in the fixed reference frame. \mathbf{A} is then written as the summation of the three column vectors of \mathbf{A} and multiplied by $\ddot{\theta}$, $\ddot{\phi}$, and $\ddot{\psi}$ respectively:

$$\text{LHS} = \begin{bmatrix} a_{1,1} \\ a_{2,1} \\ a_{3,1} \end{bmatrix} \ddot{\theta} + \begin{bmatrix} a_{1,2} \\ a_{2,2} \\ a_{3,2} \end{bmatrix} \ddot{\psi} + \begin{bmatrix} a_{1,3} \\ a_{2,3} \\ a_{3,3} \end{bmatrix} \ddot{\phi} + \mathbf{B} + \mathbf{C} \quad (4.6)$$

In solving the moment equation it is assumed that the motor rotation and thus the motion of the four bar mechanism is known. Because the out of plane angle θ is small, it is also assumed that the angle ψ corresponds approximately to the angle of the rocker of the four-bar. Furthermore, \mathbf{M}_{BS} , \mathbf{M}_{TS} , and \mathbf{M}_{AERO} are only functions of angles θ , ϕ , and ψ , therefore the only unknown terms are θ , ϕ , and the magnitudes of \mathbf{M}_{INPUT} , and \mathbf{M}_{GUIDE} . Bringing the unknown terms to the LHS and the known terms to the RHS Eq (4.5) can be rewritten as follows:

$$\mathbf{A}_1\ddot{\theta} + \mathbf{A}_3\ddot{\phi} - \mathbf{T}_1\mathbf{M}_{INPUT} - \mathbf{T}_2\mathbf{N} = \mathbf{D} \quad (4.7)$$

Where \mathbf{M}_{INPUT} and \mathbf{N} are the magnitudes of \mathbf{M}_{INPUT} , and \mathbf{M}_{GUIDE} and \mathbf{T}_1 and \mathbf{T}_2 are directions of the input moment and guide moments in the wing fixed reference frame. And \mathbf{D} is the vector containing the known external moments. Eq. (4.7) can be written as a 3x4 matrix \mathbf{E} , made from the vectors \mathbf{A}_1 , \mathbf{A}_2 , \mathbf{T}_1 , and \mathbf{T}_2 , multiplied by a 4x1 column vector containing the unknown variables as follows:

$$\mathbf{E} \begin{Bmatrix} \ddot{\theta} \\ \ddot{\phi} \\ \mathbf{M}_{INPUT} \\ \mathbf{N} \end{Bmatrix} = \mathbf{D} \quad (4.8)$$

As it stands, there are four unknowns for only three differential equations. The final equation depends on the follower/wing position. Similar to the actual motion of insect wings, there are four stages of the follower/wing motion, the down stroke, the upstroke, the supination, and the pronation. During the down stroke, the lobe end of the follower is in contact with the guide. In the model, the lobe is represented by a line such that only the end point of the line contacts the guide. For this stage, the fourth equation comes from the constraint that the tip of the follower lobe stays in contact with the guide. This constraint can be written mathematically by

finding the equation of the line defined by the intersection of the guide plane and the sphere with a radius from the wing pivot to the tip of the follower lobe. The equation of the guide plane is as follows:

$$m = \frac{z_2}{x_2} \quad (4.9)$$

where m is the slope of the guide. The parametric equation of the sphere defined by the tip of the follower lobe is as follows:

$$\begin{aligned} x_2 &= (c_\theta c_\phi - s_\theta s_\psi s_\phi) l_{lobe} - s_\theta c_\psi l_{follower} \\ z_2 &= -c_\psi s_\phi l_{lobe} + s_\psi l_{follower} \end{aligned} \quad (4.10)$$

where $l_{follower}$ is the length from the follower/wing pivot to the end of the follower, and l_{lobe} is the length from the end of the follower to the tip of the lobe as shown in Fig.

4.2. The variables x_2 and z_2 are the coordinate positions of the lobe end point in the body fixed frame \mathcal{C} . Substituting Eq (4.10) into Eq. (4.9) gives us the a constraint equation in terms of θ , ϕ , and ψ , taking the second derivative of this equation gives an Equation in the necessary form:

$$J_1 \ddot{\theta} + J_2 \ddot{\phi} + J_3 M_{INPUT} + J_4 N = J_5 \quad (4.11)$$

During the upstroke the solution is very similar, except the follower contacts the guide on the non lobe side. In the theoretical solution, we assume this is similar to the base of the follower contacting the guide. The only change that occurs is the parametric equation of the sphere is now as follows:

$$\begin{aligned} x_1 &= -s_\theta c_\psi l_{follower} \\ z_1 &= s_\psi l_{follower} \end{aligned}, \quad (4.12)$$

where x_1 and z_1 are the end point coordinates of the base of the follower. This yields another constraint equation, again taking the second derivative gives another equation in the form of Eq. (4.11).

During the pronation and supination stages, the follower no longer contacts the guide so the normal force N is zero, making the constraint equation.

$$N=0, \quad (4.13)$$

It is not necessary to take the derivatives of this Eq. (4.13) because it is already in the form of Eq. (4.11).

Using the constraint equation as the fourth differential equation, each stage's governing equations can be written in this form:

$$F \begin{Bmatrix} \ddot{\theta} \\ \ddot{\phi} \\ M_{\text{INPUT}} \\ N \end{Bmatrix} = \mathbf{G} \quad (4.14)$$

Pre-multiplying \mathbf{G} by the inverse of F gives four linear ODE's that can be solved using the ODE45 solver of MatlabTM. All four solutions are then pieced together to form a continuous solution for a single stroke.

4.7 Model Results

Before examining the model results, it is informative to analyze the aerodynamic force generation in an idealized wing motion. The desired motion of the mechanism is as follows: during the down stroke the wing should be fully pronated and at the bottom of the stroke it should quickly supinate by 90 degrees. The wing should remain supinated by 90 degrees throughout the upstroke and quickly pronate back to the original position at the top of the upstroke. Fig. 4.7 plots the aerodynamic

force predictions using the aerodynamic model, and the feathering, and flapping angles of this idealized wing motion at a flap rate of 5 Hz. In order to improve the accuracy of the plot, however, the wing supination angle is 85 degrees not 90. The reason for this is that the aerodynamic model considers an infinitesimally thin wing. If the wing is rotated such that it is parallel to the air flow it generates no lift. At a supination angle of 85 degrees the wing has approximately the same effective surface area as the surface area of the edge of the physical wing.

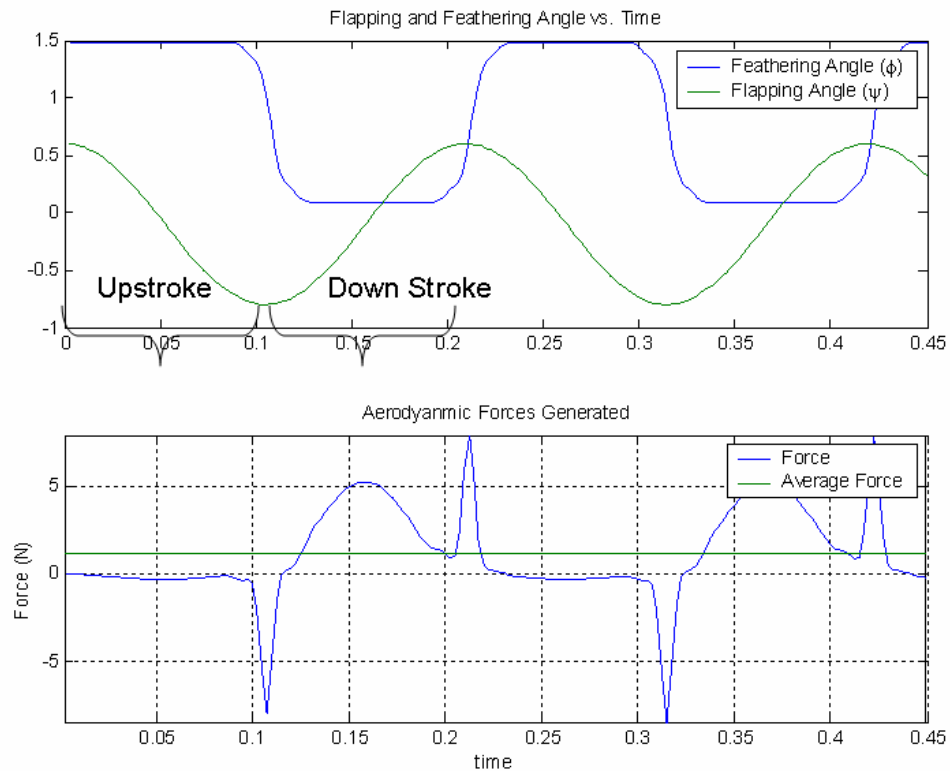


Figure 4.7: The two graphs show the feathering and, flapping angle, and aerodynamic force in the Z direction vs. time. The force data is generated by the aerodynamic model presented. The magnitude of the lift generated in the down stroke is much greater than the magnitude of the negative lift generated in the upstroke.

The aerodynamic model agrees with the original hypothesis. During the down stroke the wing generates positive lift and during the upstroke the wing generates negative lift. However, the magnitude of positive lift on the down stroke is greater than the negative lift on the upstroke thus there is a net positive lift. There is also a spike in lift during the feathering motion of the wing. Supination at the end of the down stroke will create a positive spike in force and pronation at the end of the

upstroke will add a negative spike in force as shown in the graph. These spikes in force last only for a brief period but can add substantial lift. The average lift predicted by this model is 1.14 N, well in excess of the predicted weight of the mechanism.

The results from the dynamic model presented in this chapter shared the same basic trends as that the desired wing motion. Fig. 4.8 shows these results. At the beginning of the upstroke the wing quickly supinates. The supination angle is slightly over shot, but is then damped by the aerodynamic forces. The wing remains in this supinated position until the top of the upstroke. At the top of the upstroke, the wing then pronates, slightly over shooting its original angle before being damped out by the aerodynamic forces. The same basic aerodynamic trends are also present. During the upstroke a negative lift force is generated, and during the down stroke a positive lift force is generated. Also, the magnitude of the positive lift is greater than that of the negative lift. Rotational peaks are also present during the pronation and supination of the wings. The average lift generated is 1.02 N, slightly less than the idealized wing motion. It should be noted these graphs show the angle of the follower and not the wing, consequently if the flap angle of the follower is increasing then the flap angle of the wing is decreasing.

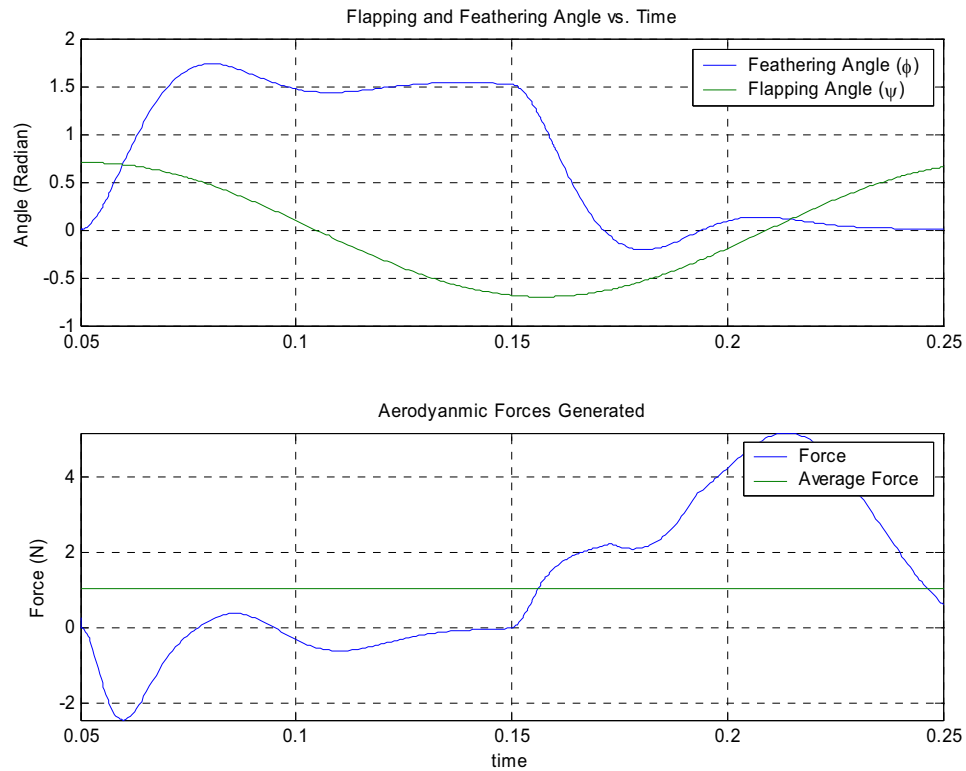


Figure. 4.8: A shows the flapping, and feathering angle vs. time and B shows the aerodynamic force in the z direction vs. time. The wing is flapping at 5 Hz.

4.8 Summary

This chapter has presented the derivation of a dynamic model for the MHP III flapping mechanism. The dynamic model developed in this chapter behaves similar to the observed motion of the prototype and predicts sufficient lift for hovering. The next chapter will present the experimental data and compare this to the theoretical data obtained in this chapter.

CHAPTER 5

EXPERIMENTAL ANALYSIS OF MHP

5.1 Introduction

Three successive iterations of the MHP design were studied in this thesis both qualitatively and quantitatively. The first major goal was to create a mechanism that would run smoothly and with repeatability. Once this was accomplished, a more quantitative look could begin measuring actual forces acting on the mechanism. The following chapter presents the MHP designs and the experimental set up, as well as the quantitative data collected.

5.2 Iterations of the MHP

Before arriving at the final design of MHP III, we built two previous models. The first design, built mainly to validate the ideas of the proposed mechanism, was named MHP I. MHP I captured the major principles of the mechanism, still there were a number of significant differences between it and its successive iterations. The major differences were the gear train and the spring materials. In MHP I, a single gear, attached to the motor, drove both main gears, as opposed to the drive and idler gears used in MHP III. Consequently, the two main gears rotated in the same direction creating asymmetric flapping. In addition, an extension of the carbon fiber leading edge wing spar served as the bending spring. The carbon fiber proved too stiff for smooth operation, leading to its replacement with the

coil over bending spring described in Sec. 3.4. Furthermore, the metal torsion spring in the current iteration replaced a small latex rubber band. The rubber band was unsuitable because it became inelastic and brittle after continual tension and relaxation. No quantitative experimentation was performed on MHP I. It performed well enough to give promise for successive iterations. Figure 5.1 shows a photograph of this first iteration.

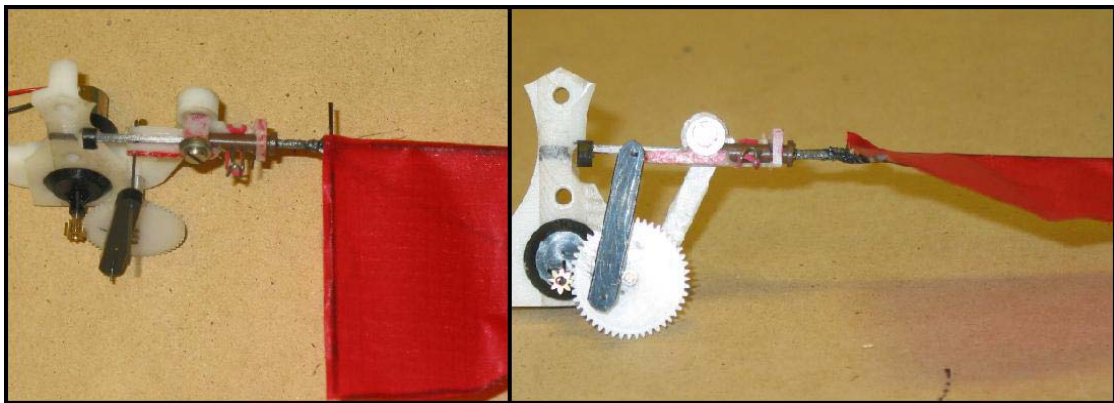


Figure 5.1: The photographs show the first iteration of the design, named MHP I. No quantitative experimentation was carried out on MHP I, but it did validate the basic premise of the mechanism.

The second iteration, MHP II, was much more effective, containing most of the refinements found in MHP III. There was an extensive use of ball bearings and metal coil over springs, as well as the symmetrical drive train used in MHP III. This second iteration allowed for some quantitative experimentation. Fig. 5.2 shows a photograph of MHP II.

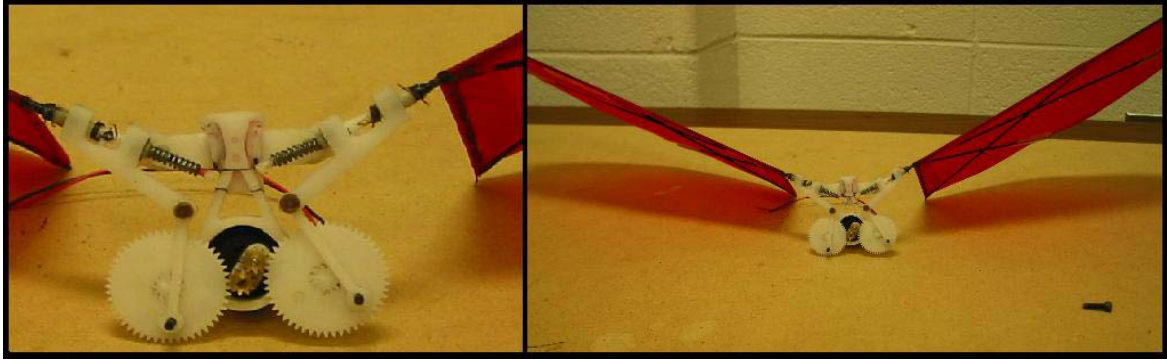


Figure 5.2: The photographs show the second iteration of the design, named MHP II. Initial lift experiments were performed on MHP II.

MHP III saw only subtle changes from MHP II. However, its wingspan was decreased substantially to come closer to the DARPA specifications for MAVs. Rigorous quantitative experiments were performed on MHP III. The experiments measured lift forces, motor power usage, and wing position in order to compare with the theoretical results. Fig. 5.3 shows a photograph of MHP III.

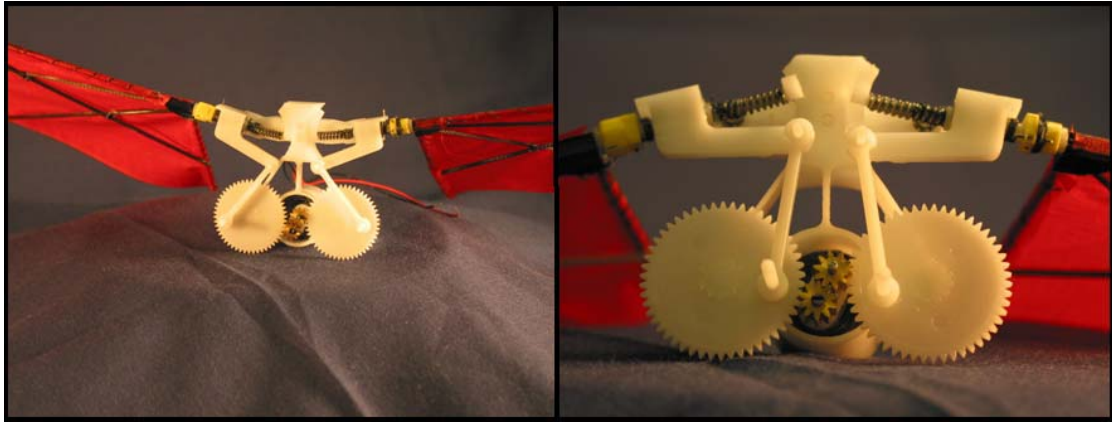


Figure 5.3: The photographs are of the most recent iteration of the design, named MHP III. Extensive measurements of lift production, wing position, and motor torques were performed on MHP III.

5.3 Setup of the MHP II Experiments

As stated earlier, the MHP II experiments measured aerodynamic lift generation at various flap rates. A three-axis force/torque sensor and constant voltage power source measured the experimental data. Visual inspection of dial gauges were used to record voltage and current, which led to rough estimations of current levels. The force data was collected accurately using a data acquisition board that was then processed through Matlab™'s Simulink™. From periodicity of the force data, the flap rate was determined but there was no explicit measurement of wing position.

The experiments for MHP II were set up in the following manner: MHP II was mounted onto a slender aluminum cylinder welded to a base plate and rigidly fixed to a workbench. A stainless steel collar attached to a shoulder on the top of the cylinder, a setscrew secured the collar to the cylinder. The collar was bolted to the force torque sensor, while another collar was bolted to the top of the force torque sensor. The force/torque sensor was model Nano 17 manufactured by ATI industrial

automation. It has a sensing range in the F_x and F_y direction of ± 12.0 N and in the F_z direction of ± 17 N. Only the force measurements were recorded. Fig. 5.4 shows a schematic of Nano 17 including its dimensions and orientation of its axes.

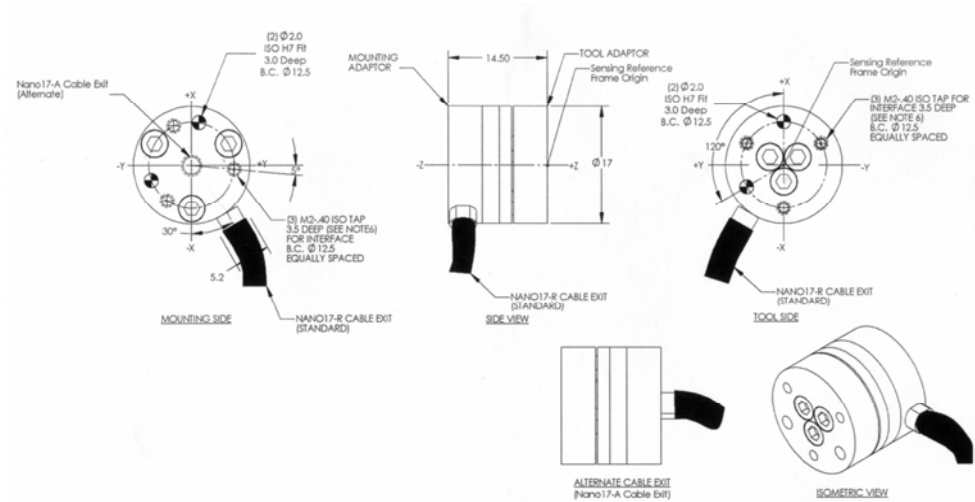


Figure 5.4: A schematic of the force torque sensor used in the experiments. The F_x and F_y axes are shown bisecting the circular cross-section of the sensor with the F_z axes directed out of the page.

A setscrew secured a delrin mounting fixture to the top collar. The delrin mounting fixture fit around the boss extruding from the MHP II's body. Held in place by two setscrews, the boss slid snugly into the mounting fixture. Finally, a large box shrouded the mechanism from outside drafts. Fig. 5.5 shows the experimental setup.

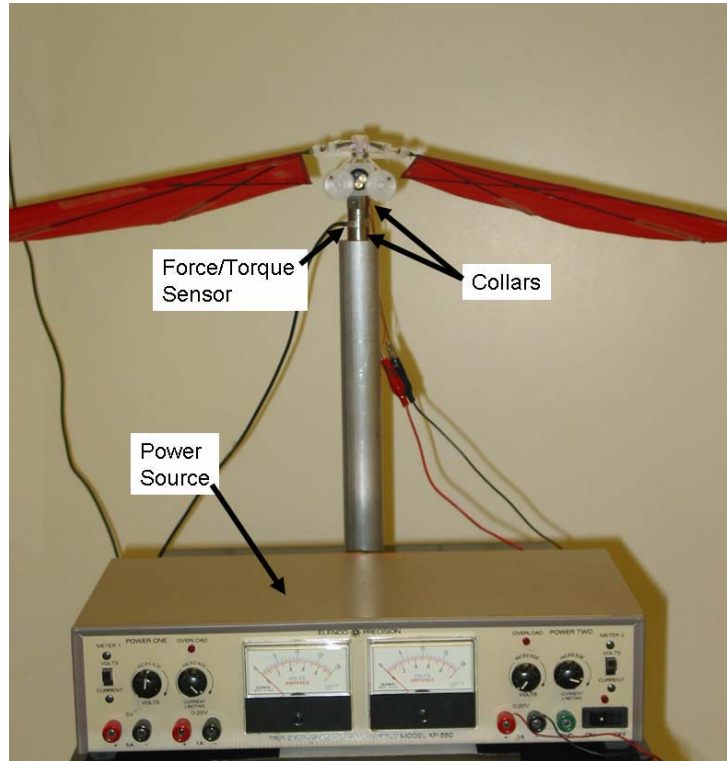


Figure 5.5: The photograph shows the experimental setup used for MHP II. MHP II rests on top of a slender aluminum rod. Between MHP II and the rod is a small force/torque sensor. Also seen in the picture is the constant voltage power source used to power the MHP II's motor.

The force data collected by the force/torque sensor was input directly to the data acquisition board. The data acquisition board was a dSPACE™ model 1103, which input data to Simulink™. A simple low-pass filter reduced noise of the experimental measurements. This filter proved better in following sudden peaks, presumed responsible for unsteady aerodynamic effects, than a butterworth filter or a convolution filter. The LP smoothing filter is given by the difference equation

$$y(n) = a y(n) + (1 - a) x(n), \quad (5.1)$$

where $x(n)$ represents the discrete-time signal with $n = 0, 1, 2, \dots, N$, and N is the number of samples. The parameter a is a weighting factor ($0 < a < 1$), $y(n)$ is the smoothed output with $y(-1) = 0$, $y(n)$ is the weighted average of the new input $x(n)$ and output $y(n-1)$ at the preceding time instant $n-1$. The closer a is to zero the closer the output is to the input; the closer a is to 1 the more weighted the output is and the smoother the function becomes. Values of a generally range between 0.7 and 0.8 depending on noise [41].

5.4 Experimental Results of MHP II

The experimental results for MHP II were very encouraging. Observation of the experiment showed that at low flap rates (< 0.5 HZ), friction at the follower/guide contact is the dominant force acting to slow down the flapper. At higher flap rates, the wing inertia actually helps to move the wing past these high friction areas. At these higher flap rates, the motor appears to work hardest at the beginning of each half stroke, where it must work against the inertia of the wings. The motor also strains during the down stroke where the motor works against the aerodynamic forces. Fig. 5.6 shows a graph of the motor torques. Power usage begins at 0.18 Watts, where frictional forces dominate, and then reduce slightly to 0.15 Watts as inertial forces over power the frictional forces. As the flap rate increases further, the power usage increases due to larger aerodynamic and inertial loads. The motor power usage was measured by recording the values of a dial gauge power source showing current and voltage output.

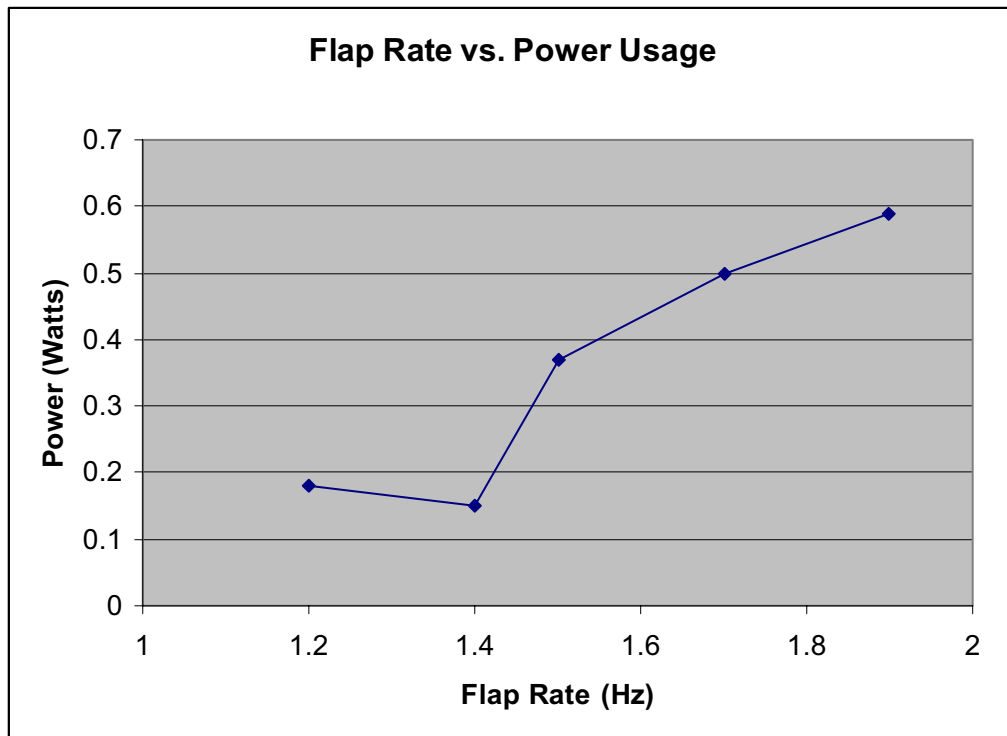


Figure 5.6: The graph shows the approximate motor power usage at various flap rates. Initially the power usage reduces as inertial forces overcome large frictional forces. The power usage then increases as inertial and aerodynamic forces increase.

More encouraging than the power usage is the lift generation. As expected, as the flap rate increased so did the aerodynamic lift, and at a flap rate of 1.9 Hz the average lift was 0.54 N in excess of the 0.45 N of gravitational force generated by the mass of the vehicle. This number, of course, does not include the weight of a battery or other accessories that would be necessary for free flight. A graph plotting the lift vs. time is shown in Fig. 5.7. The complete set of data is included in Appendix A—here we present only the F_z forces because the F_x and F_y forces were relatively small. As can be seen in the Fig. 5.7, there are two distinct peaks in lift for

every stroke. In these experiments, there is no measurement of wing position so the relationship between the force peaks and the flapping and feathering angle is unknown. Therefore, it is only surmised that the force peaks correspond to the translational forces of the wing generated during the down stroke and the rotational forces generated by the wing during supination at the bottom of the down stroke, as seen in the theoretical data. The inertial forces of the wings may also contribute significantly at the top and bottom of each stroke. With out more information it is difficult to draw any further conclusions.

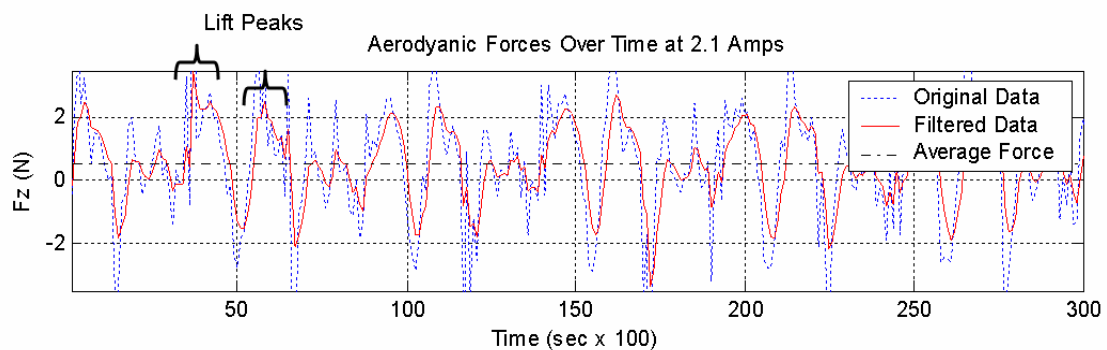


Figure 5.7: Lift vs. time Graph of MHP II at a flapping rate of 1.9 Hz. For each stroke there are two distinct lift peaks that are surmised to correspond to translational forces and rotational forces.

5.5 Experimental Setup of MHP III

The experiments for the MHP III were set up very similar to the experiments for MHP II. The major improvements made to the experiments were the ability to measure the wings' flapping angle and also accurately measure the motor power. All the information was processed through the same data acquisition board,

such that the wing position, aerodynamic loads, motor power were all recorded simultaneously.

The encoder used was a US digital E4 Miniature optical encoder measuring 300 counts per revolution. The encoder mounted to the main gear axle measures main gear position. A MatlabTM program computed the wing flap angle from the position of the main gear. The encoder only measured one wing, because both wings were assumed symmetric. The motor was still powered from a constant voltage power source, but a resistor was wired in series to the circuit. The voltage drop across the resistor was thus measured in the dSPACE. From information of the resistor and the voltage drop, the current was calculated. From the current and the voltage information, the power was computed. Figure 5.8 shows a photograph of the experimental setup for MHP III.

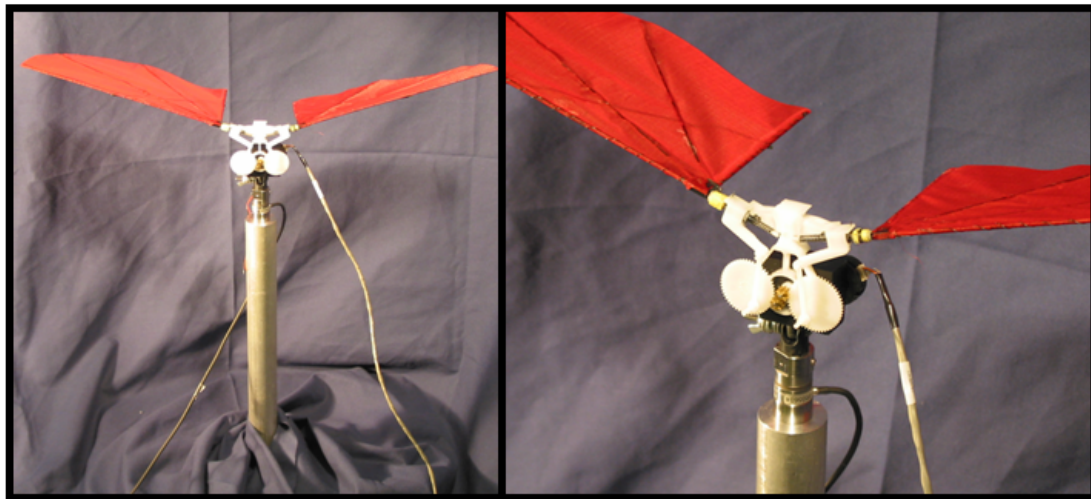


Figure 5.8: The photographs show the experimental setup of MHP III. The grey cable, hanging off to the right is the encoder cable, and the black cable hanging off to the left is the force/torque cable.

Data for MHP III was collected at three separate occasions labeled Trial 1, 2, and 3. Trial 1 and 2 used the wing measurements shown in Chapter 3. Trial 3 used larger wings of the same approximate size as MHP II. In each trial, measurements were made at a number of different flap rates. Graphs for each trial are included in Appendix B.

5.6 Experimental Results of MHP III

The experimental results of MHP III were not as encouraging and were somewhat perplexing, especially considering the performance of MHP II. Fig. 5.9 shows a typical set of data captured for MHP III. The graphs are for a flap rate of approximately 4.7 Hz (5v) during trial 2.

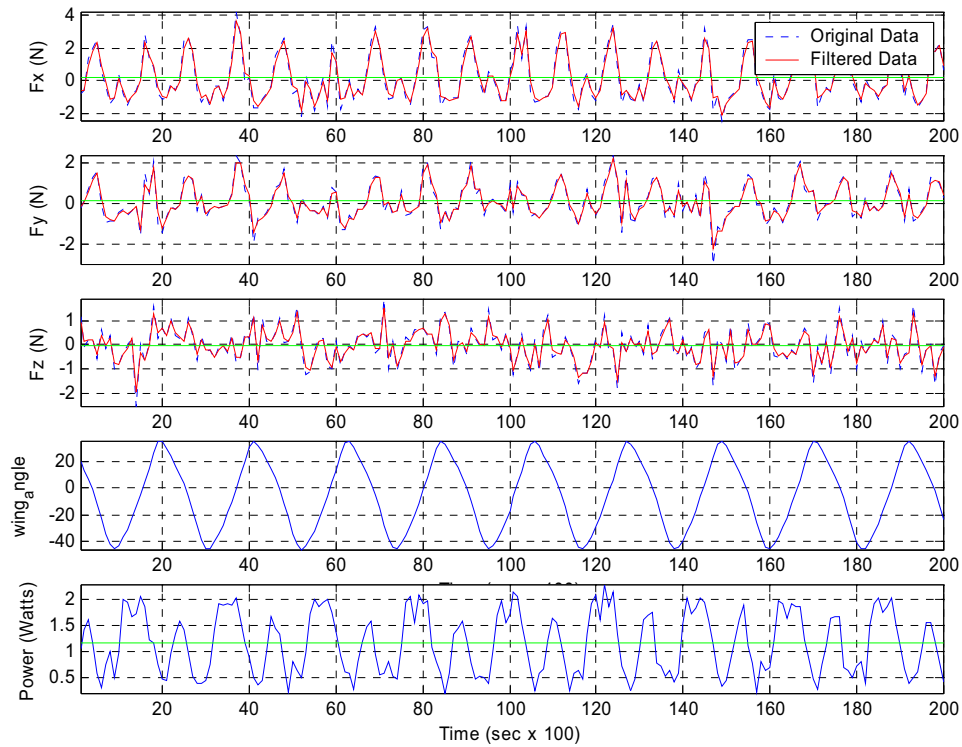


Figure 5.9: The above graph is the typical set of data captured in the MHP III experiments. The first three graphs show the F_x , F_y , and F_z forces respectively. The fourth graph is the flapping angle position and the fifth graph is the motor power. The Flap Rate is 5.2 Hz.

The data of each trial shows certain similarities. One similarity is that the motor power graphs have two reoccurring peaks per stroke. One large peak just after the down stroke as the wing changes direction and another smaller peak just after the upstroke again as the wing changes direction. This is consistent with where the inertial forces of the wing are the greatest. The motor power peak observed during the beginning of the upstroke is greater than the power peak during the down stroke. This most likely occurs because of the impulse force associated with lobe of the follower

colliding with the guide. During the down stroke, the non-lobed end of the follower contacts the guide but the collision is not as severe. Fig. 5.10 shows these two power peaks.

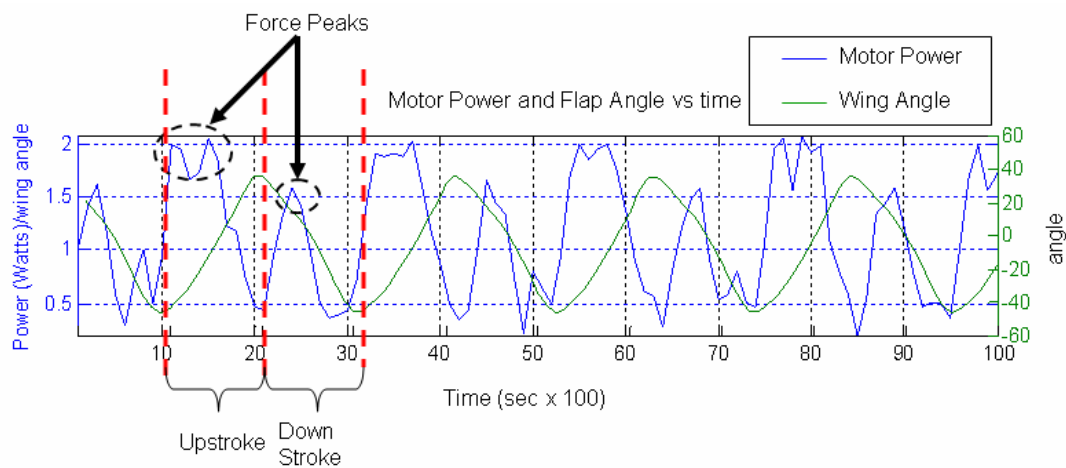


Figure 5.10: The graph shows where the motor power peaks occur relative to the flap angle. There is a large peak just after the wing begins its upstroke and a smaller peak just after the wing begins its down stroke. The large spikes are attributed to the inertial loads on the motor and the contact force of the follower with the guide.

In the MHP II experiments, there were large consistent force peaks in the z direction relative to the forces in the x and y directions. During the MHP III experiments, these force peaks were not as discernable and the total forces were considerably smaller than forces in the x and y directions. There were still some noticeable trends shown in Fig. 5.11. The average force in the z direction during the down stroke is positive and the average force during the upstroke is negative consistent with predictions.

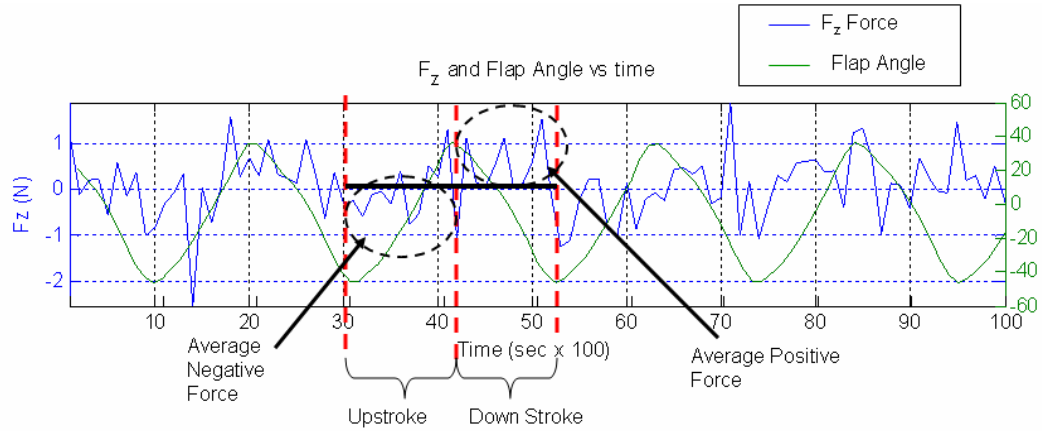


Figure 5.11: The graph shows the F_z forces vs. time. The force values were much smaller than in the MHP II experiments but the average force in the down stroke was positive and the average force in the upstroke was negative consistent with predictions.

The major force peaks occur in the y and the x direction. Forces in the y direction are side forces, which are not desirable for hovering flight. They are most likely due to asymmetries in the flapping mechanism. Generally, though, these forces were smaller than forces in the x direction. In the experimental orientation of MHP III the forces in the x direction would cause a forward motion. F_x forces did show some consistent trends. Experimental data showed two positive force peaks during the translational motion of the wings for both the up and the down stroke as shown in Fig. 5.12. There are also smaller lift peaks that may occur because of rotational forces.

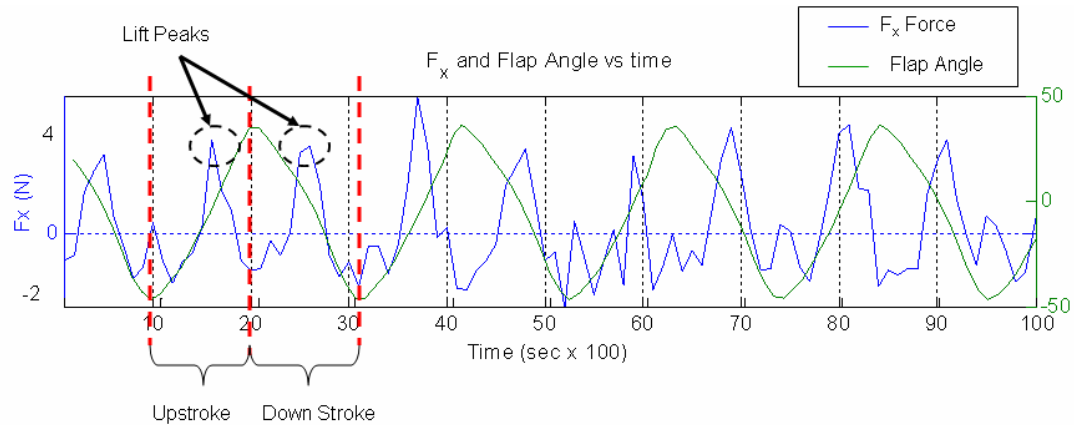


Figure 5.12: The graph shows the force data in the x direction and the flap angle vs. time. It shows two consistent spikes in lift during the translational motion of the wing.

5.7 Conclusions

The low forces in the z direction for the MHP III experiments were perplexing. Analysis of the video footage of the flapper motion the two mechanisms helped shed some light on the subject. In the MHP II design, a pin was used to secure the torsion spring to the wing axle. Due to the location of the pin, the wing was restricted from over-pronating at the top of the upstroke. The MHP III design was slightly different and this pin that restricted the over pronation of the wing was absent. Because of this reason, at the top of the upstroke the wing would continue to pronate further due to the momentum of the wing. This over-pronation is also observed in the theoretical model in Fig. 4.8, but the predicted aerodynamic forces damp out the over-pronation more than in the physical system. Because of this small difference in design, we believe the wing motion of MHP II and MHP III were significantly different. The motion of MHP III was more symmetric, as shown in Fig. 5.13. Therefore, the lift on

the down stroke would be of equal magnitude to the negative lift generated on the upstroke.

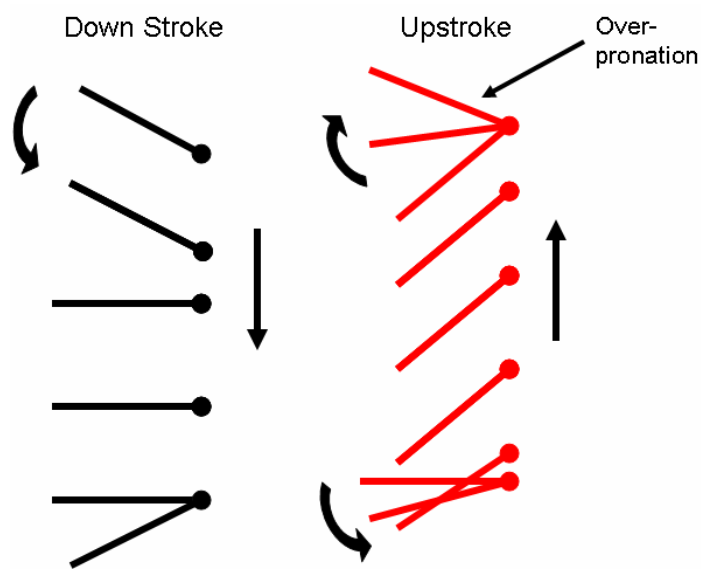


Figure 5.13: The observed motion of MHP III which differs from MHP II. At the top of the upstroke the wing over pronates reducing the effective wing surface area during the downstroke.

Experimental data of a wing motion similar to the motion observed in the MHP III experiments agree with this suspicion. Fig. 5.14 shows this lift data. As can be seen the over-pronation decreases the effective surface area on the down stroke reducing its lift. The upstroke and the down stroke therefore produce nearly equal lift causing a net lift of zero. Also the peak forces of the lift values are reduced.

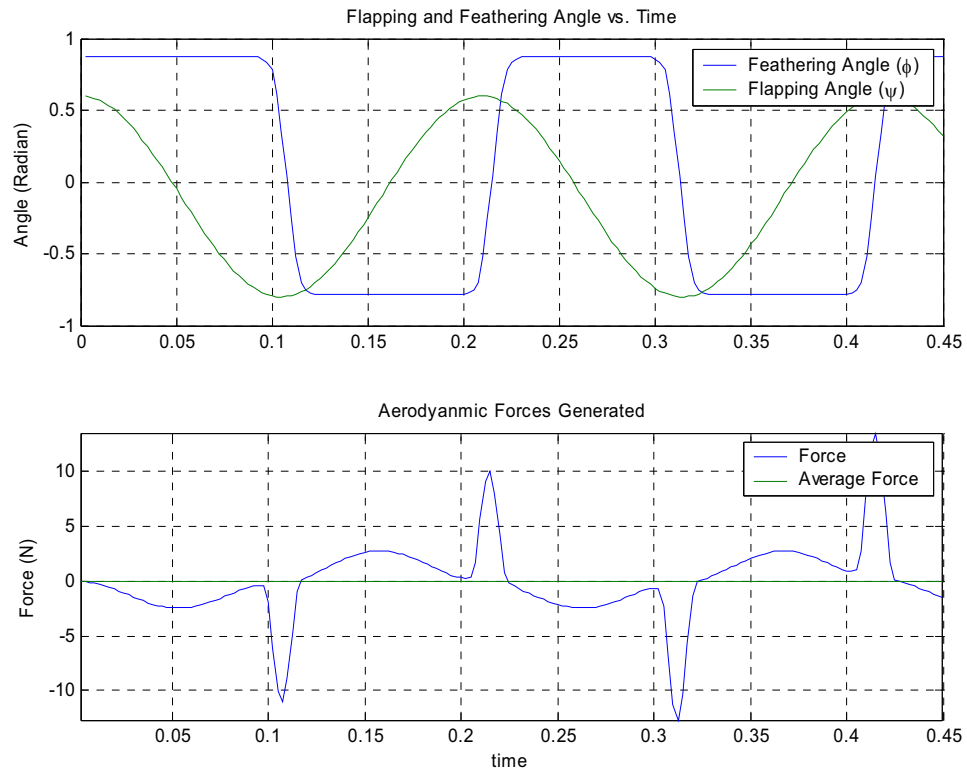


Figure 5.14: This shows the total force generation for the symmetric flapping observed by MHP III

5.8 Summary

The preceding chapter discussed the qualitative and quantitative experiments of the MHP prototypes. The lift generation of MHP II showed very encouraging figures, but because of subtle differences in the design of MHP III, these same lift values were not generated. The final chapter discusses the overall conclusions of the project and the future recommendations.

Chapter 6

CONCLUSIONS AND FUTURE RECOMMENDATIONS

6.1 Conclusion

The major contribution of this thesis is a novel mechanism for flapping wing flight. Furthermore the thesis has presented a method for theoretically predicting and the vehicles performance, and finally experimentally verifying the predictions. This final chapter discusses the overall conclusions that were made from the design and analysis of the MHP. It discusses the effectiveness of the theoretical model, experimental setup, and prototype design and how all of these can be improved. Finally, it discusses the long term goals of the MHP and ornithopters in general.

The theoretical model developed in this thesis adequately describes some of the basic features observed in the prototype. The model, however, makes a number of assumptions that may significantly affect the dynamics of the system. The model does show that during the down stroke the wings generate a greater magnitude of lift than the magnitude of negative lift generated during the upstroke. Experimental forces measured for MHP II agree with this conclusion. MHP III forces show equal lift magnitudes for both the down and upstroke. The wing motion of MHP III does not match the model results. Instead, the wing motion of MHP III over pronates at the end of the upstroke reducing its effective area during the down stroke and reducing its lift. The experimental measurements of the MHP III flapping motion is measured but

not the feathering motion so this hypothesis can not be rigorously modeled. Estimates of the MHP III model are made, and these agree with the hypothesis.

6.2 Future work

The MHP is very much a work in progress. The MHP flapping mechanism works but there is also much room for improvement. Furthermore, a great deal of information has been obtained about the MHP from the theoretical and experimental analysis, but there is still a need for a more robust computer model and thorough experiments. This final section discusses the necessary improvements for the theoretical model, experimental setup, and the prototype.

The model inaccuracies are most likely due to a number of governing assumptions. Frictional forces play an important role in the dynamics of the system as well as the impact force of the follower hitting the guide, both of which were not included in the model. Accuracy of the bending spring stiffness is also suspect, because it does not simply act about the \hat{z}_w axis, but about numerous axes in a rather complex manner. The largest assumption though is treating the follower and the wing as one rigid body. For a very accurate dynamic model the follower, wing, and wing carriage should all be treated as separate rigid bodies. This will be a much larger computational problem of course, but the wing motions should become more accurate.

The experimental setup also needs improvements. The most important improvement is the addition of an encoder to measure the feathering angle. With this information, the aerodynamic model could be accurately compared with experimental lift forces. Furthermore, measurements of purely inertial forces of the flapper could be made by removing the wing coverings. These inertial force measurements could then be subtracted from the total force generation to arrive at the pure aerodynamic

loads. In addition to the force measurements of the mechanism, PIV experiments could show the actual flow around the wings. This would give a much greater view of the actual aerodynamic mechanisms, the MHP uses to generate lift.

From these suggested experiments and the more complete dynamic model a very rigorous approach could be taken to improve the performance of the MHP prototypes. Even without these tools there are still many obvious areas of improvements. During the experiments, the contact with the follower and the guide appeared to be an area of great energy loss. Perhaps, roller bearings could be used on the follower, similar to those used in the followers of combustion engines to reduce friction. Also the impact of the follower with the guide is a source of high energy loss as well as a source of wear and tear for the mechanism. If the guide encompassed both sides of the follower it would not lose contact and there would not be sudden impacts. Another trouble area of MHP III is its tendency to over pronate at the end of the upstroke. Like MHP II, there needs to be a stop to prevent this over pronation. Also there needs to be a great deal of fine tuning of the torsion and bending springs to increase the supination angle during the upstroke while not overly increasing the contact force between the follower and the guide.

In all, the MHP shows a great deal of promise. MHP III however, still does not fly, which is the ultimate goal of the project. In the future, the mechanism will be optimized in order to reach this goal. Once flying has been accomplished, the next major goal will be to create an onboard system to control the MHP during flight. From this point, the size and weight of the MHP prototypes will be reduced to fit into the MAV size range. Hopefully, some day the mechanism designed for MHP will be a valuable technology in MAV flight.

APPENDIX A
EXPERIMENTAL RESULTS ON MHP II

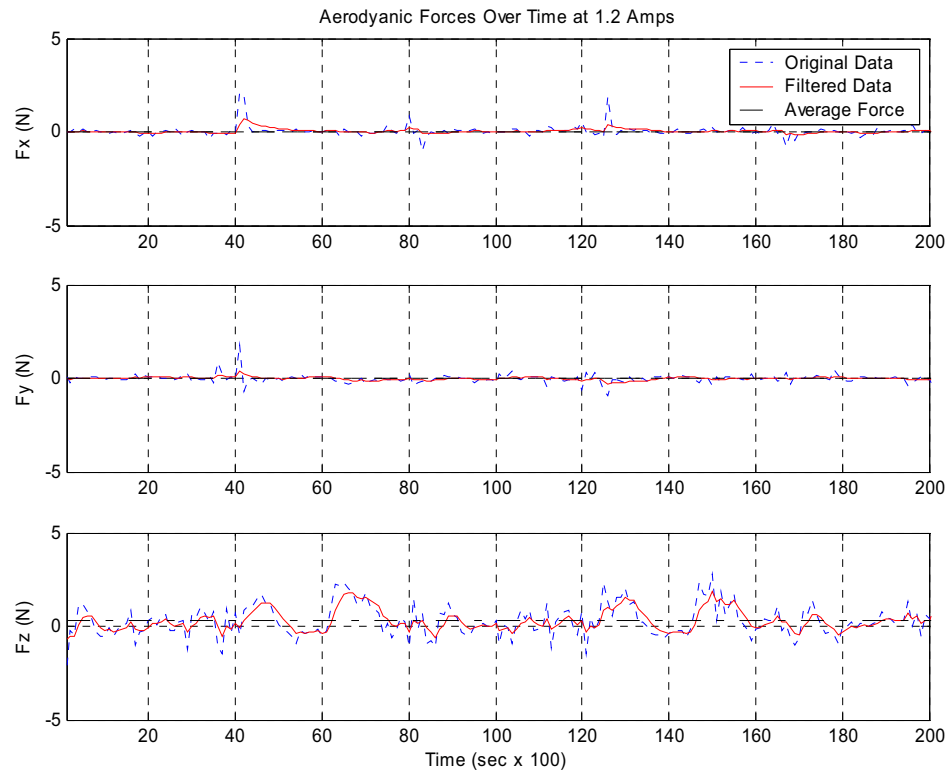


Figure A.1: Aerodynamic forces in the x, y, and z directions with a motor current of 1.2 amps. The average force in the x and y is 0.01 N and -0.03 N respectively. The average force in the z direction is 0.32 N with a maximum force of 1.78 N.

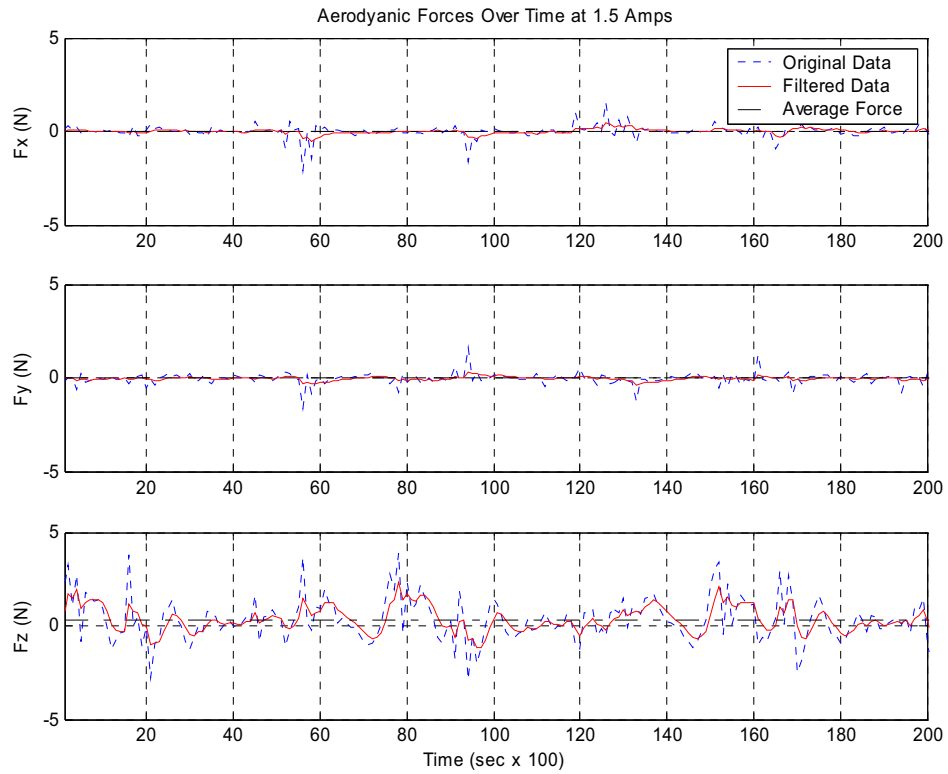


Figure A.2: Aerodynamic forces in the x, y, and z directions with a motor current of 1.5 amps. The average force in the x and y is 0.00 N and -0.03 N respectively. The average force in the z direction is 0.33 N with a maximum force of 2.12 N.

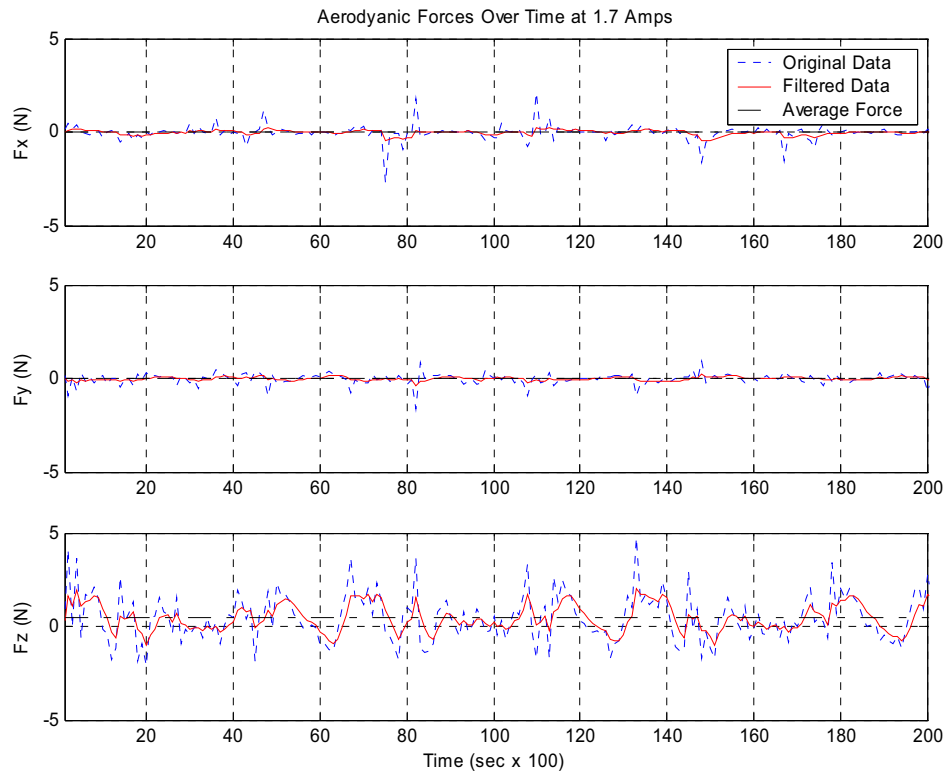


Figure A.3: Aerodynamic forces in the x, y, and z directions with a motor current of 1.7 amps. The average force in the x and y is -0.02 N and -0.02 N respectively. The average force in the z direction is 0.46 N with a maximum force of 1.67 N.

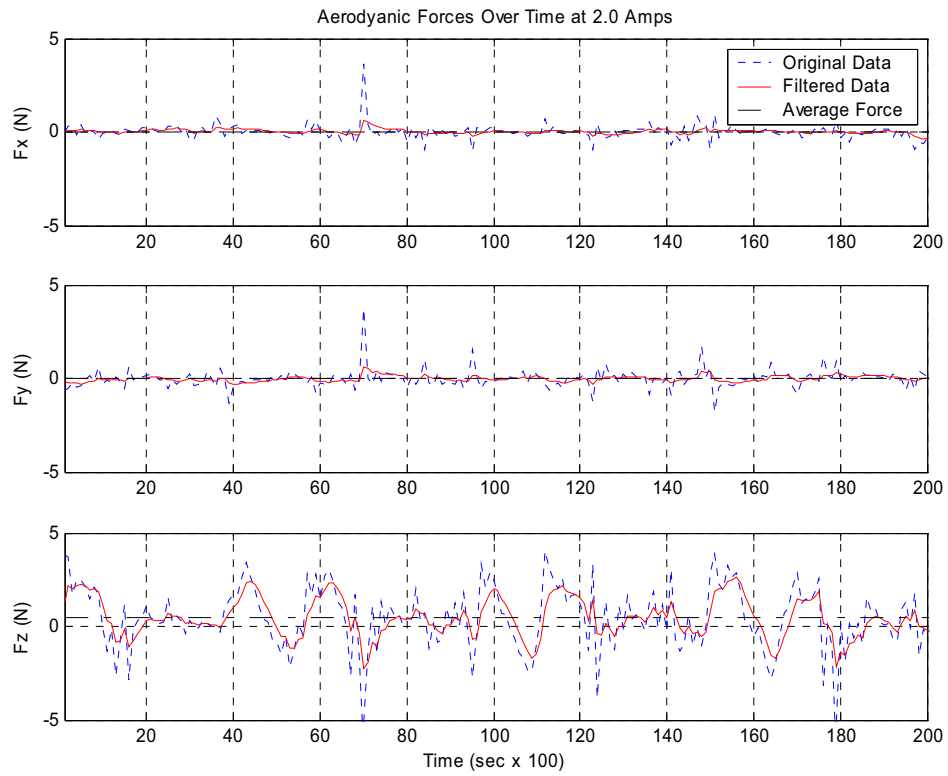


Figure A.4: Aerodynamic forces in the x, y, and z directions with a motor current of 2.0 amps. The average force in the x and y is 0.01 N and -0.04 N respectively. The average force in the z direction is 0.48 N with a maximum force of 2.61 N.

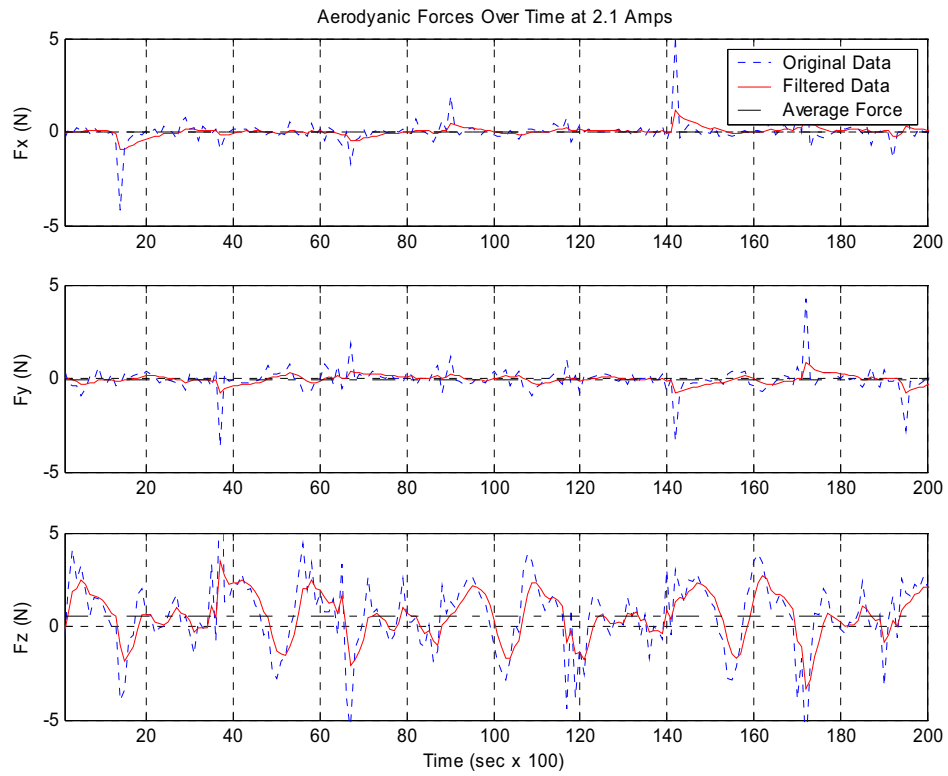
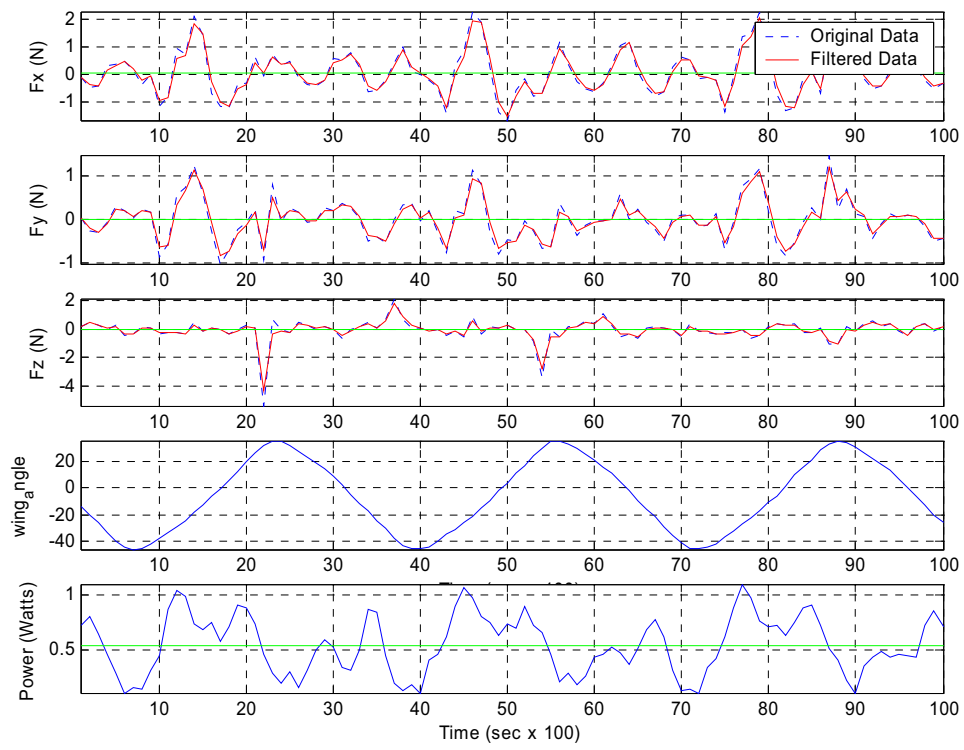


Figure A.5: Aerodynamic forces in the x, y, and z directions with a motor current of 2.1 amps. The average force in the x and y is 0.01 N and -0.05 N respectively. The average force in the z direction is 0.54 N with a maximum force of 3.47 N.

APPENDIX B

EXPERIMENTAL RESULTS OF MHP III



**Figure B.1: 3v Trial 1—Flap Rate = 2.9 Hz, $F_{x\text{mean}} = 0.0607$ $F_{y\text{mean}} = -0.0046$,
 $F_{z\text{mean}} = -0.0642$, $\text{Power}_{\text{mean}} = 0.5399$ W**

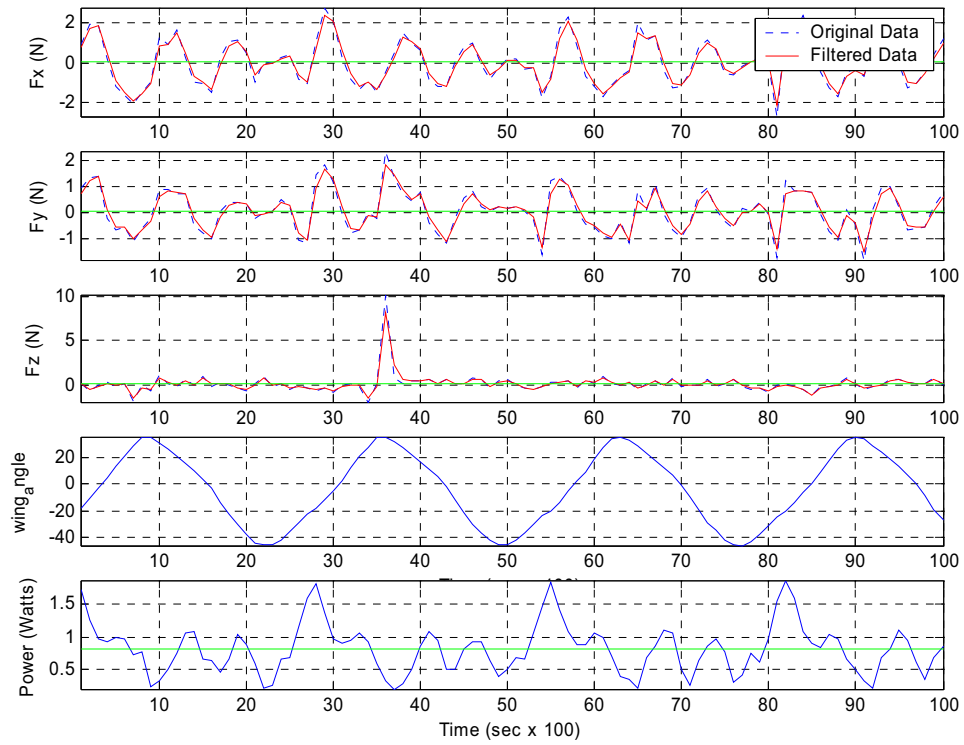


Figure B.2: Trial 1—Flap Rate = 4.0 Hz, $F_{x\text{mean}} = 0.0140$ N, $F_{y\text{mean}} = 0.0474$ N, $F_{z\text{mean}} = 0.1290$ N, $\text{Power}_{\text{mean}} = 0.8143$ W

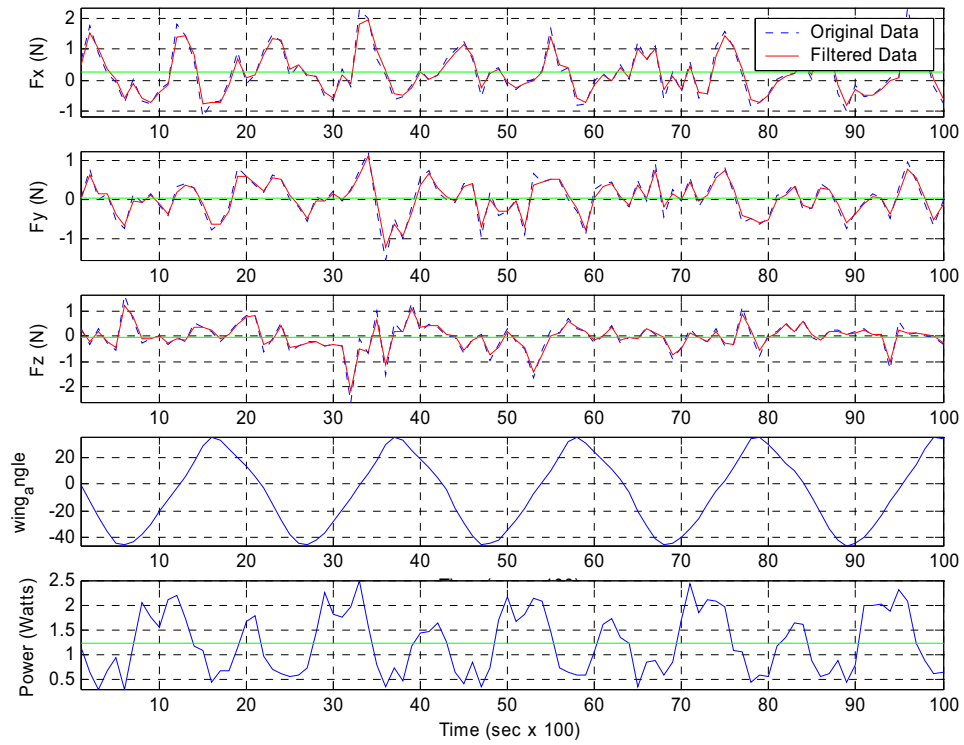


Figure B.3: Trial 1—Flap Rate = 5.5 Hz, $F_{x\text{mean}} = 0.2412$ N, $F_{y\text{mean}} = 0.0138$ N, $F_{z\text{mean}} = -0.0290$ N, $\text{Power}_{\text{mean}} = 1.2219$ W

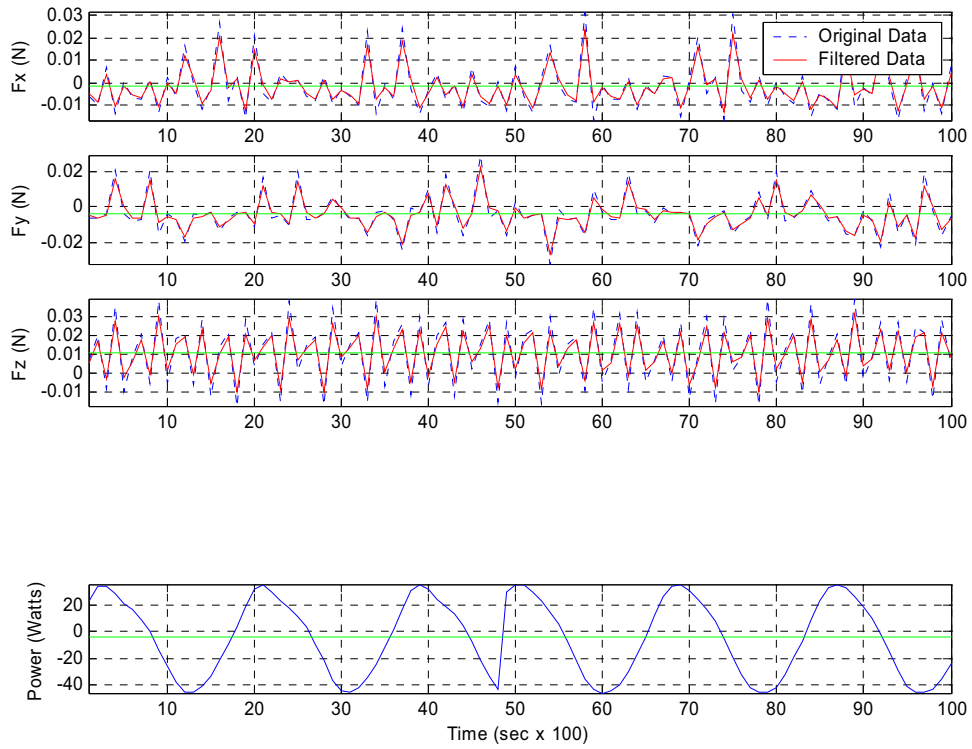


Figure B.4: Trial 1—Flap Rate = 6.7 Hz, $F_{x\text{mean}} = -0.0017$ N, $F_{y\text{mean}} = -0.0040$ N, $F_{z\text{mean}} = 0.0110$ N, $\text{Power}_{\text{mean}} = -4.3910$ W

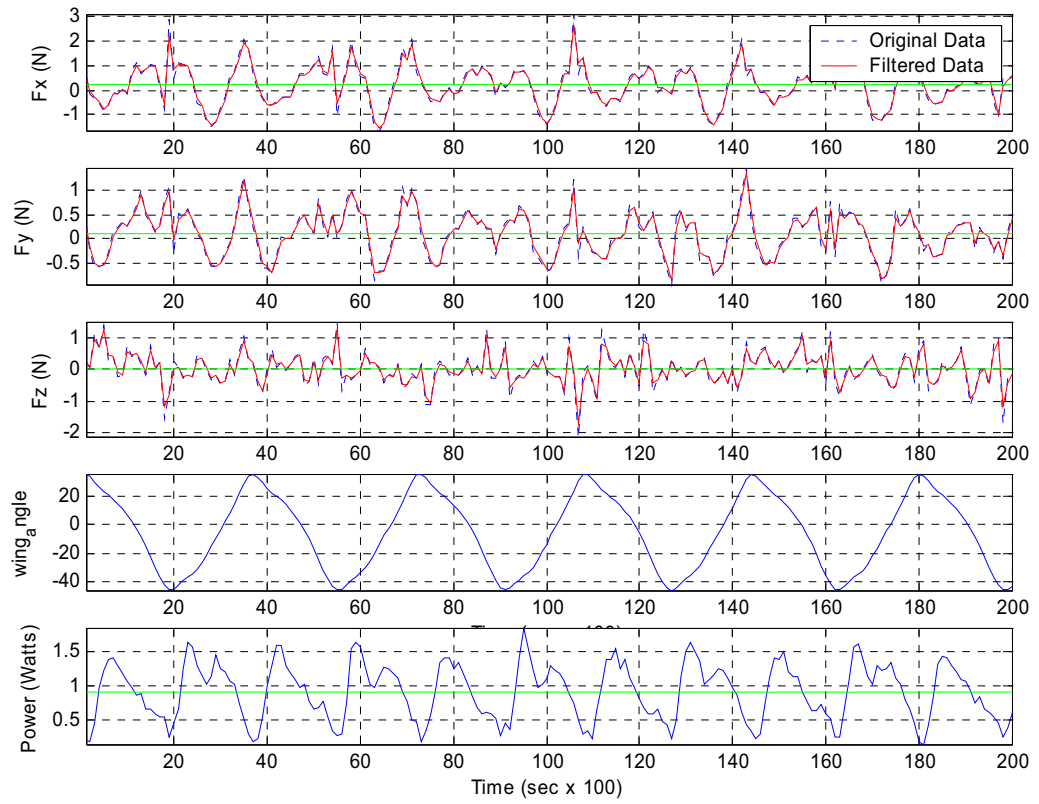


Figure B.5: Trial 2—Flap Rate = 3.2 Hz, $F_{x\text{mean}} = 0.2121$ N, $F_{y\text{mean}} = 0.1033$ N, $F_{z\text{mean}} = 0.0209$ N, $\text{Power}_{\text{mean}} = 0.9098$ W

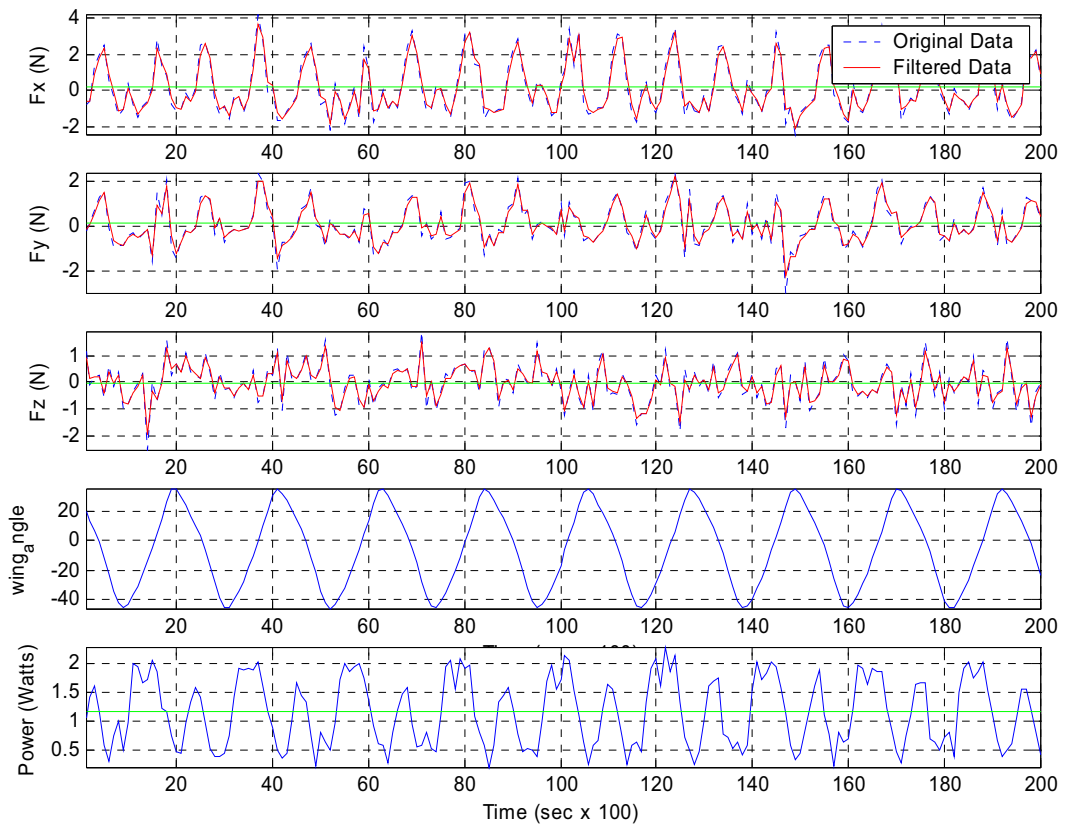


Figure B.6: Trial 2—Flap Rate = 5.2 Hz, $F_{x\text{mean}} = 0.2014$ N, $F_{y\text{mean}} = 0.1116$ N, $F_{z\text{mean}} = -0.0244$ N, $\text{Power}_{\text{mean}} = 1.1530$

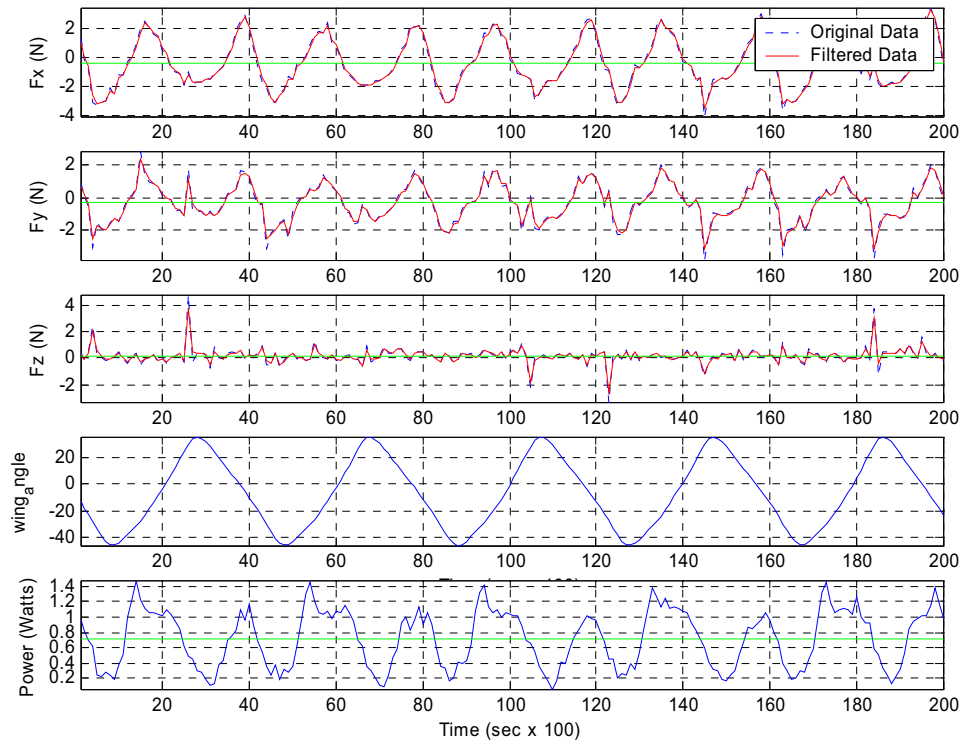


Figure B.7: Trial 3 Flap Rate = 3 Hz, $f_{x\text{mean}} = -0.4089$ N $f_{y\text{mean}} = -0.3176$ N $f_{z\text{mean}} = 0.1628$, $\text{Power}_{\text{mean}} = 0.7210$ W

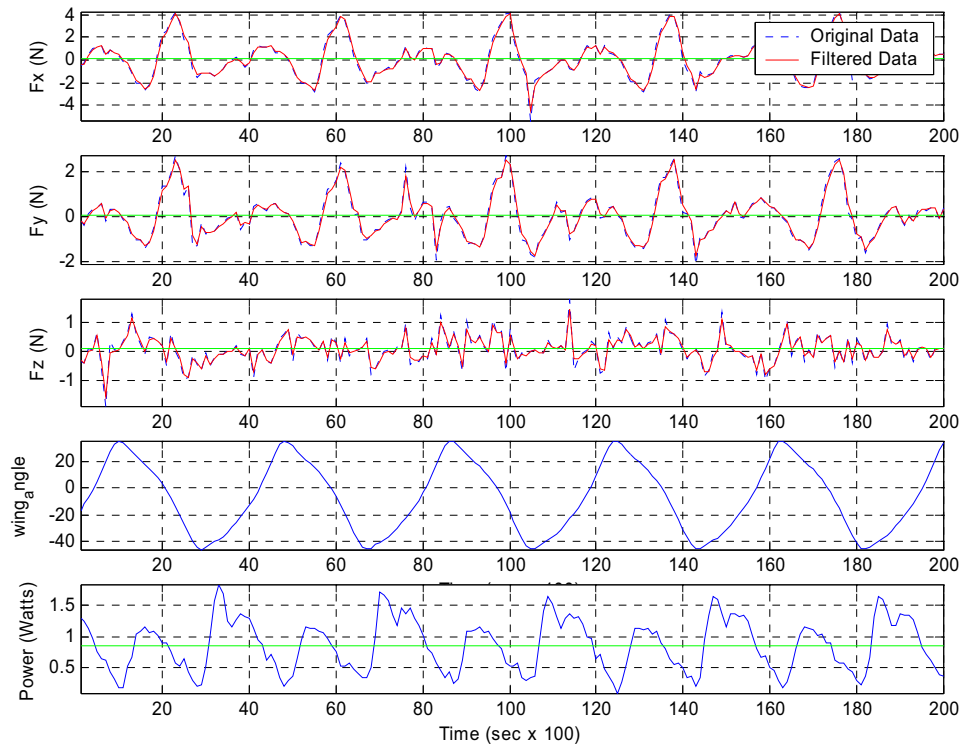


Figure B.8: Trial 3—Flap Rate = 3.3 Hz, $F_{x\text{mean}} = 0.0637$ N, $F_{y\text{mean}} = 0.0451$ N, $F_{z\text{mean}} = 0.0659$ N, $\text{Power}_{\text{mean}} = 0.8653$ W

APPENDIX C

FRABRICATION DETAIL OF MHP III

The following parts were machined out of delrin using a two axis CNC machine and/or a lathe in the Coleburn machine shop at the University of Delaware: the body, the wing carriages, the wing carriage supports, the followers, the wing base plate, the connecting rods, the wing axel, the wing carriage pins, the connecting rod pins, the wing carriage support pins, the wing spar juices, the idler gear mount, wing carriage spacers, and the main gear axels. The profiles of the guides were cut from the body using the CNC but the final shaping of the guides was done by hand using a Dremel.

The following parts were machined out of steel using a lathe in the Coleburn machine shop at the University of Delaware: wing pin connector, idler gear axel.

The following is a list of each purchased part and its supplier. 4 *Main gear axel bearings*—1.5mm bore 4 od x 1.2: Homefly; 4 *Wing carriage bearings*—1.5mm bore 4 od x 1.2: Homefly; 4 *Wing axel bearings*—*specifications*: MMB; 2 *bending springs* (compression springs)-- *specification*: McMaster; 2 *Torsion springs*—Music wire tosion spring 90 deg angle, .160” coil OD,.017” wire: McMaster; 2 *leading edge* and 2 *root wing spars*--1.7mm dia braided carbon fiber tubes: Homefly; 4 *medial* and 2 *cross wing spars*--1.3mm dia braided carbon fiber tubes-: Homefly; 2 *Internal splined shafts*--specification: didel; 2 *Externally splined shafts*--*specification: Didel; 1 *Motor* and 1 *gear box*--Propulsion 2 Micro DC 5-2.4

Motor with a 1:11.8 ratio gear box: Wes Tecniq; 1 *drive gear* and 1 *idler gear*—10 tooth 1mm bore 0.5 modulus brass gear: Homefly; 2 *Main gears*—50 tooth 3 mm bore 0.5 modulus nylon gear: Homefly.

The Wing Assembly. First the wings are assembled. The leading edge wing spar, the two medial wing spars and the root spar are glued and press fit into the wing plate. The two cross spar gussets are slipped onto the leading edge and root spar and glued into position. The cross wing spar is press fit and glued into the two gussets. Kevlar thread secures the cross wing spar to the two medial spars. The nylon rip stop material is cut slightly larger than the wing. The nylon is glued to the wing spars and the wrapped over the edge and glued again. The wing pin connector is pressed and glued into the wing plate and the externally splined shaft is press fit over the wing connector such that it butts up against the wing plate and is glued to both pieces.

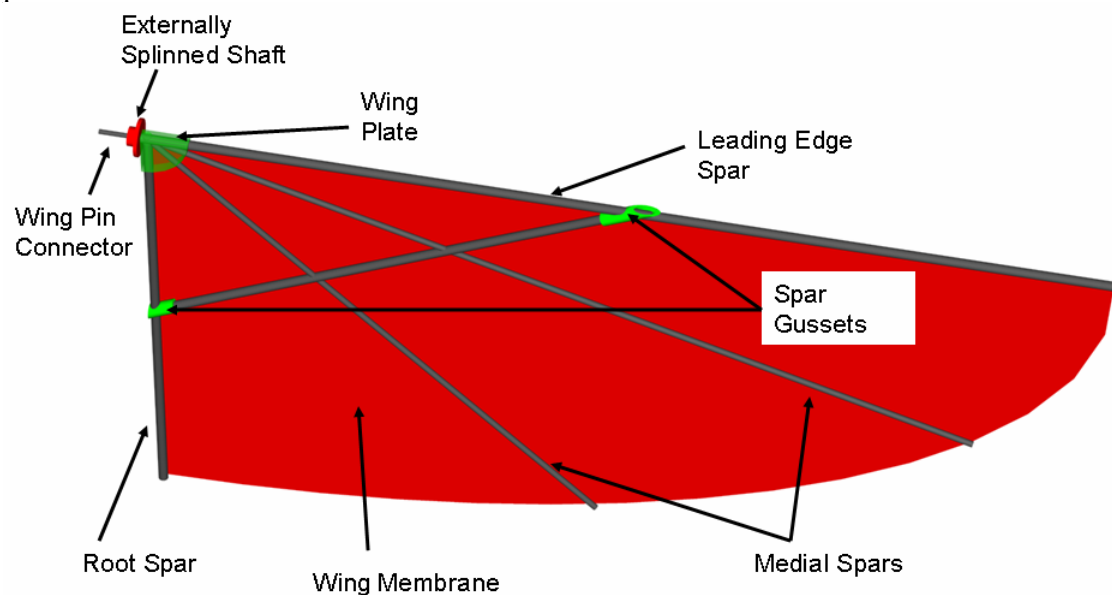


Figure C.1: labeled wing

The Body Assembly. The four main gear axle bearings are pressed into the body. The four wing carriage bearings are press fit into the win carriage support. The wing carriage support is fit into the slot on the back of the body, and then positioned with the two wing carriage support pins. Next, the main gear axles are pressed and glued into the main gears, and then the main gear axles are pressed into the main gear axle bearings. The idler gear mount is pressed over the motor shaft bearing support. The idler gear shaft is then pressed into the idler gear mount. Both the drive gear and the idler gear are press fit and glued onto their respective shafts. The motor is then press fit into the body such that the drive gear and the idler gear mesh with the main gears.

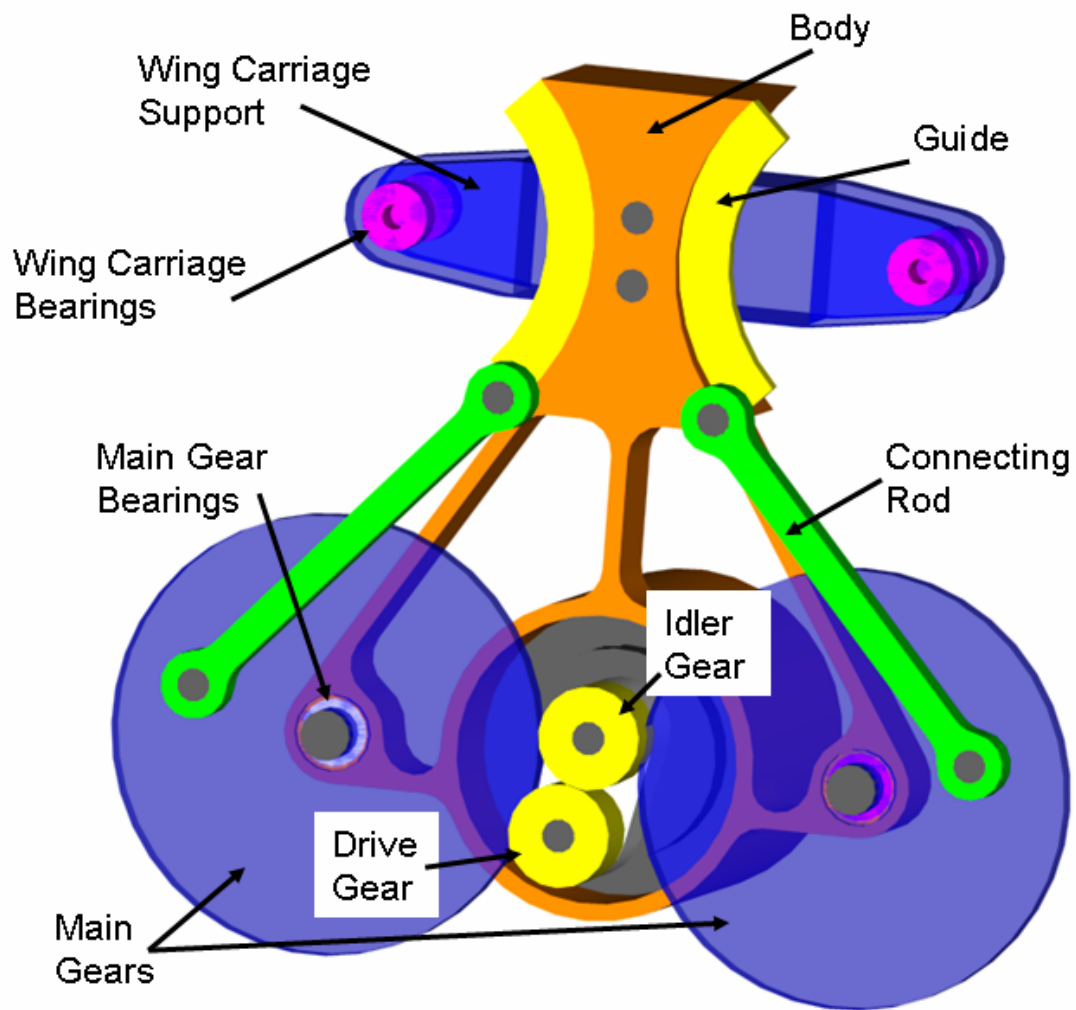


Figure C.2: Body Assembly

The Wing Carriage Assembly. The four wing axle bearings are pressed into the wing carriages. The follower is press fit into the bending spring and glued in place. The wing axle is press fit into the other end of the bending spring and glued in place. The wing axle is then pressed into the wing axle bearings. The torsion spring is slipped over the outside end of the wing axle. The inside end of the torsion spring

fits into a small hole in the wing carriage lip. The internally splined shaft is now press fit and glued to the wing axle such that the outside end of the torsion spring fits into the small spring hole on the shaft.

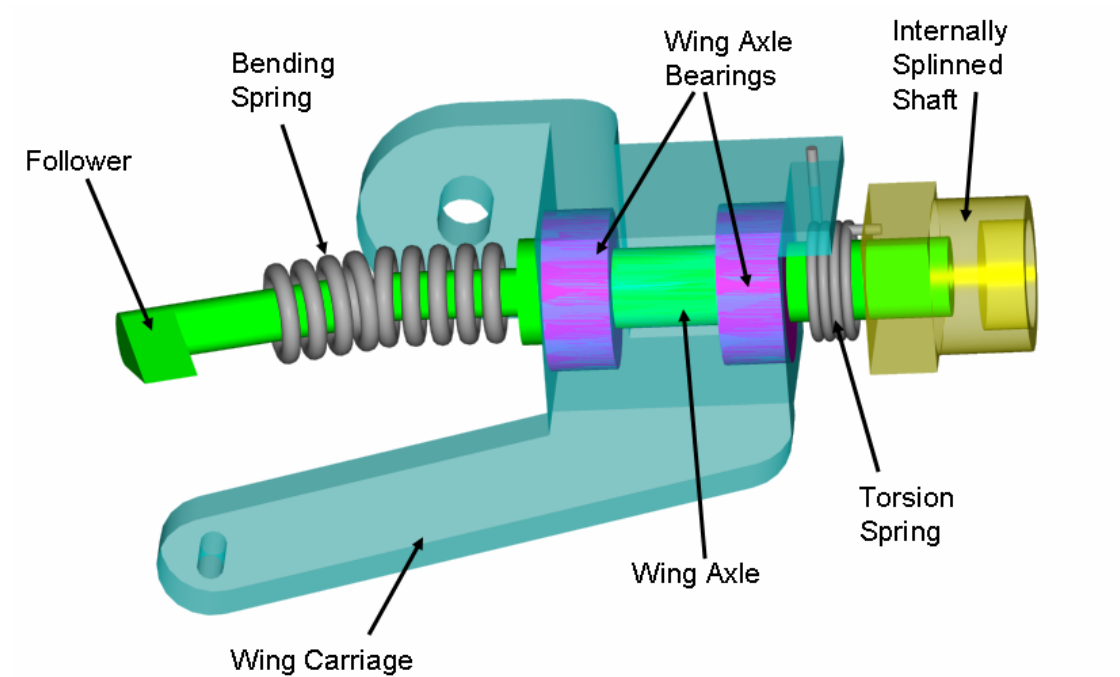


Figure C.3: Wing Carriage Assembly

The removable wings can now be fit into place with the mating internal and externally splined shafts fitting together.

REFERENCES

- [1] Michael H. Dickinson, Fritz-Olaf Lehmann, Sanjay P. Sane “Wing Rotation and the Aerodynamic Basis of Insect Flight”. *Science*, Vol. 284, June 18 1999, pp. 1954-1960
- [2] David L. Raney, Eric C. Slominski “Mechanization and Control Concepts for Biologically Inspired Micro Aerial Vehicles,” *AIAA Guidance, Navigation & Control Conference*, 11-14 August 2003
- [4] Aerovironment, URL: <http://www.aerovironment.com/news/news-archive/wasp62.html>
- [5] Dr. Stephen J. Morris, Dr. Michael Holden, “Design of Micro Air Vehicles and Flight Test Validation”
- [6] Yongsheng Lian, Wei Shyy, Raphael T. Haftka, “Shape Optimization of a Membrane Wing for Micro Air Vehicles”. *SAMPE Journal*, vol. 42, n 2, February, 2004, p 424-426 Florida Tech
- [7] William E. Green and Paul Y. Oh, “Towards Autonomous Fixed-Wing MAVs with Hovering Capabilities,” submitted to the *IMECE conf.* 2005
- [8] Peter Muren, URL: <http://www.proxflyer.com>
- [9] Alexander Van de Rostyne, URL: <http://pixelito.reference.be/>
- [10] Profs. Ilan Kroo and Fritz Prinz “Mesicopter: A Meso-Scale Flight Vehicle NIAC Phase II Technical Proposal” Stanford University mesicopter
- [11] URL: <http://www.angelfire.com/electronic/awakening101/leonardo.html>
- [12] Science Museum London, URL: <http://www.sciencemuseum.org.uk/online/flight/flight/frost.asp>
- [13] Wikipedia, URL: http://en.wikipedia.org/wiki/Alexander_Lippisch

- [14] J.D. DeLaurier, "The Development and Testing of a Full-Scale Piloted Ornithopter". *Canadian Aeronautics and Space Journal* Vol. 45, No. 2, June 1999.
- [15] smaller scales can flap wings faster
- [16] URL:<http://www.ornithopter.org/store/slowhawk.info.html>
- [17] Mathew McDonald, "Design of flapping-wing micro-aerial vehicles motivated by Hawk Moths and Hummingbirds," Undergraduate Thesis submitted to the University of Delaware
- [18] T. Nick Pornsin-Sirirak, S. W. Lee, H. Nassif, J. Grasmeyer, Y.C. Tai, C. M. Ho, M. Keennon, "MEMS Wing Technology for a Battery-Powered Ornithopter," The 13th IEEE International Conference of Micro Electro Mechanical Systems (MEMS '00), Miyazaki, Japan, Jan 23-27, 2000, pp. 799-804
- [19] Dean Eberhardt URL: <http://www.andrew.cmu.edu/user/deberhar/Mentor.html>
- [20] R.J. Wood, S. Avadhanula, and R.S. Fearing, "Microrobotics using Composite Materials: the Micromechanical Flying Insect Thorax," *IEEE Int. Conf. on Robotics and Automation* 2003, pp. 1842-1849, Taipei, Taiwan.
- [21] Frampton K.D., Goldfarb M.: Passive Aeroelastic Tailoring for Optimal Flapping Wings. Conference on Fixed, Flapping and Rotaary Winged Vehicles for Very Low Reynolds Numbers," Notre Dame, IN, June 2000.
- [22] Fritz-Olaf Lehman, "The mechanisms of lift enhancement in insect flight", *Naturwissenschaften* 2004, 91:101-122
- [23] Sanjay P. Sane "The aerodynamics of insect flight", *The Journal of Experimental Biology* 206, 4191-4208.
- [24] Pijush K. Kundu and Ira M. Cohen. *Fluid Mechanics* (Second Edition). Academic Press, 2002.
- [25] Ellington CP (1984e) The aerodynamics of hovering insect flight. I. The quasi-steady analysis. *Philos Trans R Soc Lond B* 305:1-15
- [26] Ellington, C.P. (1984a). The aerodynamics of hovering insect flight. I. The quasi-steady analysis. *Phil. Trans. R. Soc. Lond. B* 305, 1-15.
- [27] Liu, H. and Kawachi, K. (1988). "A numerical study of insect flight." *J. Comput. Physics* 146, 124-156.

- [28] Dickinson, M. H., Lehmann, F.-O. and Gotz, K. G. (1993) "The active control of wing rotation by *Drosophila*." *J. Exp. Biol.* 182, 173-189.
- [29] Katz J. Plotkin A (2002) "Low-speed aerodynamics". Cambridge University Press, Cambridge.
- [30] R.B. Srygley and A. L. R. Thomas (2002) "Unconventional lift-generating mechanism in free-flying butterflies", *Nature Publishing Group*, Vol 420, 12 December 2002, pp. 660-662.
- [31] Willmott AP (1995) The mechanics of Hawkmoth flight. Thesis, Cambridge University, Cambridge.
- [32] Dickinson MH (1994) "The effects of wing rotation on unsteady aerodynamic performance at low Reynolds numbers." *J Exp Biol* 192: 179-206.
- [33] Dickinson MH, Lehmann F-O, Sane S (1999) "Wing rotation and the aerodynamic basis of insect flight." *Science* 284:1954-1960.
- [34] Srygley RB, Thomas ALR (2002) Unconventional lift-generating mechanism in free-flying butterflies." *Nature* 420:6600-6604
- [35] Sun M, Tang J (2002) Lift and power requirements of hovering flight in *Drosophia virilis*." *J. Exp Biol* 205: 2413-2427.
- [36] Weis-Fogh T (1975) "Unusual mechanisms for the generation of lift in flying animals." *Sci Am* 233:80-87
- [37] Sanjay P. Sane and Michael H. Dickinson (2001). "The aerodynamic effects of wing rotation and a revised quasi-steady model of flapping flight" *Journal of experimental Biology*, 205, 1087-1096.
- [38] Usherwood, J.R. and Ellington C.P. (2002) "The aerodynamics of revolving wings. I." *J. Exp. Biol.* 205, 1457-1564.
- [39] Usherwood, J.R. and Ellington C.P. (2002) "The aerodynamics of revolving wings. II." *J. Exp. Biol.* 205, 1457-1564.
- [40] Jeffrey A. Walker (2002). "Rotational lift: something different or more of the same?" *Journal of Experimental Biology*, 205, 3783-3792 (2002).
- [41] Zaeems Ashraf Khan "Experimental Investigation and Modeling of Flapping Wing Aerodynamics" Master's Thesis submitted to the University of Delaware.

- [42] *Spacecraft Dynamics*, by Kane, Likins, and Levinson, McGraw-Hill Book Company, New York, 1983
- [43] S. Banala, Z. Khan, S. McIntosh, Y. Karakaya, S. K. Agrawal, “Design and Optimization of a Mechanism for Out of Plane Insect Wing Like Motion With Twist”, *ASME Mechanisms and Robotics Conference*, 2004.
- [44] Z. A. Khan and S. K. Agrawal, “Wing Force and Moment Characterization of Flapping Wings for Micro Air Vehicle Application”, *American Control Conference*, 2005.
- [45] R. Madangopal, Z. A. Khan, and S. K. Agrawal, “Energetics Based Design of Small Flapping Wing Air Vehicles”, *IEEE International Conference on Robotics and Automation*, 2004.
- [46] R. Madangopal, Z. Khan, and S. K. Agrawal, “Biologically Inspired Design of Small Flapping Wing Air Vehicles Using Four Bar Mechanisms and Quasi-Steady Aerodynamics”, *ASME Mechanisms and Robotics Conference*, 2004.